CHARACTERIZATION OF BORON DOPED ZINC OXIDE THIN FILMS PREPARED BY SPRAY PYROLYSIS DEPOSITION TECHNIQUE

MEHNAZ SHARMIN

MASTER OF PHILOSOPHY IN PHYSICS

DEPARTMENT OF PHYSICS

BANGLADESH UNIVERSITY OF ENGINEERING AND TECHNOLOGY

DHAKA-1000, BANGLADESH

JULY, 2015

CHARACTERIZATION OF BORON DOPED ZINC OXIDE THIN FILMS PREPARED BY SPRAY PYROLYSIS DEPOSITION TECHNIQUE

by

MEHNAZ SHARMIN

ROLL NO. 0412143011P

SESSION: APRIL-2012

MASTER OF PHILOSOPHY IN PHYSICS

DEPARTMENT OF PHYSICS

BANGLADESH UNIVERSITY OF ENGINEERING AND TECHNOLOGY

DHAKA-1000, BANGLADESH

JULY, 2015

CANDIDATE'S DECLARATION

It is hereby declared that this thesis or any part of it has not been submitted elsewhere for the award of any degree or diploma.

MEHNAZ SHARMIN

ROLL NO.: 12143011P

SESSION: APRIL, 2012

DEDICATED TO

MY

FAMILY

CONTENTS

Page No.

CANDIDATE'S DECLARATION **i**

DEDICATION **ii**

ACKNOWLEDGEMENTS **vii**

ABSTRACT **x**

LIST OF FIGURES **xiii**

LIST OF TABLES **xv**

LIST OF ABBREVIATIONS **xvi**

CHAPTER 1

INTRODUCTION 1-10

1.1 Introduction 1

1.2 A Brief Review of Research on Zinc Oxide Thin Films 3

1.3 Objectives of The Present Work 6

References 8

CHAPTER 2

MATERIALS AND DEPOSITION TECHNIQUES 11-35

2.1 Properties of Zinc Oxide 11

2.1.1 Structure of zinc oxide 12

2.1.2 Optical properties 14

2.1.3 Electrical properties 16

2.2 Properties of Boron 16

2.3 Applications of Zinc Oxide 17

2.4 Thin Film Deposition Techniques 18
2.4.1 Physical techniques 19
2.4.1.1 Vacuum evaporation method 19
2.4.1.2 Sputtering 21
2.4.1.3 Epitaxial growth 22
2.4.1.4 Physical vapor deposition 23
2.4.2 Chemical techniques 24
2.4.2.1 Chemical vapor deposition 24
2.4.2.2 Spin coating 26
2.4.2.3 Sol-gel technique 27
2.4.2.4 Chemical bath deposition 29
2.4.2.5 Electroplating 30
2.4.2.6 Spray pyrolysis technique 30
2.4.2.7 Electrodeposition 32
References 33

CHAPTER 3

THEORIES RELATED TO CHARACTERIZATION TECHNIQUES 36-67
3.1 Structural Characterization 36
3.1.1 X-ray diffraction 37
3.1.1.1 Lattice constant 38
3.1.1.2 Crystallite Size 39
3.1.1.3 Microstrain 39
3.1.1.4 Dislocation density 39
3.2 Surface Morphology 40
3.2.1 Working principle of an electron microscope 40

3.2.2 Scanning electron microscopy 41

3.3 Elemental Analysis 43

3.3.1 Energy dispersive x-ray spectroscopy 43

3.4 Optical Characterization 44

3.4.1 Beer-Lambert law 44

3.4.2 Electronic transitions 46

3.4.3 Direct and indirect optical transitions 49

3.4.4 Refractive index and extinction coefficient 52

3.4.5 Instrumentations 54

3.4.6 Experimental procedure 56

3.5 Electrical Characterization 57

3.5.1 Direct method 57

3.5.2 Two point probe method 58

3.5.3 Linear four point probe method 58

3.5.4 Van der Pauw technique 60

3.5.5 Factors affecting resistivity measurement 62

3.5.6 Activation energy 62

3.6 Thickness Measurement 63

References 66

CHAPTER 4

SAMPLE PREPARATION 68-75

4.1 Preparation of Thin Films 68

4.1.1 Experimental details 69

4.1.1.1 Preparation of masks 69

4.1.1.2 Heater 69

4.1.1.3 The design of the reactor 69

4.1.1.4 The fume chamber 70

4.1.1.5 Air compressor 70

4.1.1.6 Spray head/ nozzle 70

4.2 Substrate and Substrate Cleaning 71

4.3 Working Solution 72

4.4 Deposition Parameters 72

4.5 Rate of Deposition 73

4.6 Thickness Control 73

4.7 Sample Deposition 73

Reference 75

CHAPTER 5

RESULTS AND DISCUSSION 76-108

5.1 Introduction 76

5.2 Surface Morphology 76

5.3 Elemental Analysis 81

5.4 X-ray Diffraction 84

5.5 Optical Properties 87

5.5.1 Transmittance 87

5.5.2 Absorption co-efficient 89

5.5.3 Optical band gap 91

5.5.4 Refractive index 93

5.5.5 Extinction co-efficient 95

5.5.6 Optical conductivity 97

5.5.7 Dielectric constants and dielectric loss 99

5.6 Electrical Properties 103

5.6.1 I-V characteristics 103

5.7 Temperature dependence of electrical conductivity and activation energy 105
References 107

CHAPTER 6

CONCLUSIONS AND SUGGESTIONS FOR FURTHER WORK 109-111

6.1 Conclusions 109

6.2 Suggestions for Further Work 111

ACKNOWLEDGEMENTS

Firstly, I express very much gratefulness to the Almighty Allah, who gives me the strength and energy to fulfill this research work.

I would like to express my sincere gratitude to my supervisor Prof. Dr. Md. Abu Hashan Bhuiyan for his wonderful guidance, valuable instructions and tremendous support throughout my M. Phil. research. He is a wonderful advisor who helped me to overcome all the difficulties that I encountered during my study and research. It has been a great honor to be the student of such a great materials scientist. What I have learnt from him will help me throughout my entire life.

I am thankful to Dr. Afia Begum, Professor and Head, Department of Physics, BUET, Dhaka, for providing necessary facilities, precious suggestions and supports to carry out this work.

I wish to express my gratefulness to Prof. Dr. Jiban Podder for allowing me to use the experimental set up of SPT and also for his valuable suggestions and encouragement. I also would like to thank all my colleagues: Prof. Dr. Md. Feroz Alam Khan, Prof. Dr. A. K. M. Akther Hossain, Prof. Dr. Md. Mostak Hossain, Prof. Fahima Khanam, Prof. Dr. Md. Forhad Mina, Dr. Md. Rafi Uddin, Dr. Nasreen Akter, Dr. Mohammed Abdul Basith, Mr. Muhammad Samir Ullah, Mr. Mohammad Abu Sayem Karal, Mr. Mohammad Khurshed Alam, Mr. Md. Azizar Rahman, Dr. Mohammad Jellur Rahman, Dr. Muhammad Rakibul Islam, Mr. Md. Afjal Khan Pathan, Mr. K.A.M. Hasan Siddiquee, Mr. A.T.M. Shafiul Azam, Dr. Parvin Sultana and Mr. Md. Mehdi Masud for their supports and helpful suggestions.

I would like to give my sincere thanks to Dr. D. K. Saha, Director, BAEC, Dhaka, for providing the help in XRD measurements.

I am grateful to Dr. Md. Abdul Gafur, Senior scientific officer, PP & PDC, BCSIR, Dhaka, for UV-VIS spectroscopy measurements.

I would like to give my thanks to Prof. Dr. Md. Fakhrul Islam, Head, Department of Glass and Ceramic Engineering, BUET, Dhaka, for allowing to perform the SEM and EDX measurements.

I wish to thank all of my fellow graduate students. Working with them during these past years has truly been a joyful experience. The list is too big, but I would try to highlight a few. Thanks to Mr. Sonjit Sen Roy, Dr. Rummana Matin, Dr. Tamanna Afroze, Dalia Parven, Mr. Md. Ahaduzzaman Deeraz and Kishwar-E Hasin for their sincere help to this work.

Finally, I like to thank my family members. I express my most sincere gratitude to all of them for their continuous support and encouragement during this research work.

I acknowledge with thanks for the financial support to this thesis work provided by the authority of Bangladesh University of Engineering & Technology.

ABSTRACT

Undoped and boron (B) doped zinc oxide (ZnO) thin films are synthesized onto glass substrate by spray pyrolysis technique (SPT) at various substrate temperatures (300 - 450 °C). Concentration of B are varied between 0.50 and 1.50 at% at the step of 0.25 at% during preparation of B doped ZnO (ZnO: B) thin films. The effect of change of substrate temperature and doping concentration of B on the structural, optical and electrical properties of the ZnO thin films is studied. Scanning electron microscopy (SEM) is used to study the surface morphology of ZnO and ZnO: B thin films. The SEM images show that the glass substrates are nicely covered by fibrous and non-fibrous film. Nanofibers of various thicknesses (200- 550 nm) are observed around the nucleation center of the thin films in the SEM images. Energy dispersive X-ray (EDX) analysis illustrates that the ZnO and ZnO: B films are very close to nominal composition. Quantitative analysis shows that at% of B increases with the increase of B concentration in ZnO: B thin films. X-ray diffraction (XRD) patterns of ZnO and ZnO: B thin films show polycrystalline hexagonal wurtzite type of crystal structure. The reflections for (100), (002), (101) and (110) planes are found, among which (002) is the dominant peak. Lattice constants (a and c) are calculated for the prominent peaks. The values of a are found between 3.2365 and 3.2624 Å and those of c are found between 5.1877 and 5.3089 Å. The c/a ratio is very close to that for an ideal hexagonal structure. Crystallite size of the thin films varies from 27 to 88 nm. Crystallite size decreases, whereas microstrain and dislocation density increase with the increase of B concentration in ZnO: B thin films. Transmittance and absorbance of ZnO and ZnO: B thin films are measured by UV-visible spectroscopy and optical band gap, refractive index, extinction coefficient, dielectric constants and optical conductivity are calculated from those data. Transmittance and optical band gap (3.11 - 3.33 eV) increase and refractive index, extinction coefficient, dielectric constants and optical conductivity decrease with increasing B concentration. Electrical resistivity of ZnO: B thin films are measured at room temperature and in the range of temperature 298 – 423 K by linear four point probe method. Resistivity of ZnO: B thin films decrease both with the increase of B concentration and temperature. Activation energy of ZnO: B thin films are obtained between 0.27 and 0.52 eV.

LIST OF FIGURES

Pages

Figure 2.1: The hexagonal wurtzite structure of ZnO 13
Figure 2.2: Photoluminescence spectrum of *n*-type bulk ZnO (HeCd excitation) showing excitonic, donor acceptor pair and green-band emission [8] 15
Figure 2.3: Refractive-index dispersion of ZnO for (a) E $\perp$ c and (b) E $\parallel$ c below the fundamental absorption edge [9] 15
Figure 2.4: Types of deposition techniques 19
Figure 2.5: Schematic diagram of thermal or vacuum evaporation coating system 20
Figure 2.6: A diagram of sputtering system 21
Figure 2.7: Schematic diagram of MBE system 22
Figure 2.8: A diagram of physical vapor deposition technique 23
Figure 2.9: Schematic diagram of CVD process 24
Figure 2.10: The Plasma –Enhanced Chemical Vapor Deposition Process 25
Figure 2.11: A schematic diagram of LECVD system 26
Figure 2.12: The spin coating process 27
Figure 2.13: Generalized scheme of sol-gel synthesis 28
Figure 2.14: Chemical Bath Deposition Process 29
Figure 2.15: Schematic diagram of SPD equipment 31
Figure 3.1: Bragg‟s law of X-ray diffraction 37
Figure 3.2: Schematic diagram of an electron microscope 40
Figure 3.3: A scanning electron microscope with EDS set up 42
Figure 3.4: Absorption of light by a sample 45
Figure 3.5: Vibrational and rotational energy levels 47
Figure 3.6: Possible electronic transitions 47
Figure 3.7: Direct and indirect transitions between valance and conduction bands with extrema at different values of momentum (k) 49
Figure 3.8: Refraction of light at the interface between two media 52
Figure 3.9: Schematic diagram of the components of a spectrometer 55
Figure 3.10: A UV-vis spectrophotometer 56
Figure 3.11: Circuit arrangement of resistivity measurement by two point probe method 58
Figure 3.12: Circuit of linear four point probe for measuring resistivity 59

Figure 3.13: Experimental set up for electrical measurement 60
Figure 3.14: Experimental arrangements for measuring resistivity by using Van der Pauw method 60
Figure 3.15: Interferometer arrangement for producing reflection Fizeau fringes of equal thickness 65
Figure 3.16: Interference patterns during measurement of film thickness 65
Figure 4.1: Steps of thin film processes 68
Figure 4.2: Mask for the sample 69
Figure 4.3: Schematic diagram of the experimental setup of spray pyrolysis technique 71
Figure 4.4: Experimental set up of Spray Pyrolysis Deposition Technique at Department of Physics, BUET 74
Figure 5.1: SEM image (x 1 k) of ZnO thin film deposited at the T_s of 300 °C 77
Figure 5.2: SEM images (x 5 k) of ZnO thin films deposited at the T_s of (a) 350, (b) 400 and (c) 450 °C 77
Figure 5.3: SEM images (x 5 k) of 0.50 at% ZnO: B thin films deposited at the T_s of (a) 350, (b) 400 and (c) 450 °C 78
Figure 5.4: SEM images (x 5 k) of 0.75 at% ZnO: B thin films deposited at the T_s of (a) 350, (b) 400 and (c) 450 °C 78
Figure 5.5: SEM images (x 5 k) of 1.00 at% ZnO: B thin films deposited at the T_s of (a) 350, (b) 400 and (c) 450 °C 79
Figure 5.6: SEM images (x 5 k) of 1.50 at% ZnO: B thin films deposited at the T_s of (a) 350, (b) 400 and (c) 450 °C 79
Figure 5.7: SEM images (x 30 k) of (a) 0.50, (b) 1.00 and (c) 1.50 at% ZnO: B thin films deposited at the T_s of 450 °C 80
Figure 5.8: SEM image (x 30 k) shows nanofiber thickness 80
Figure 5.9: Droplet size is shown in an SEM image (x 2.5 k) 81

Figure 5.10: EDX spectra of (a) ZnO, (b) 0.50, (c) 0.75, (d) 1.00 and (e) 1.50 at% ZnO: B thin films 83

Figure 5.11: XRD patterns of ZnO and ZnO: B thin films deposited at the T_s of (a) 300, (b) 350, (c) 400 and (d) 450 °C 85

Figure 5.12: Variation of (a) crystallite size, (b) microstrain and (c) dislocation density with B concentration for ZnO: B thin films deposited at different T_s 87

Figure 5.13: Variation of transmittance (%) with wavelength for (a) ZnO, (b) 0.50, (c) 0.75, (d) 1.00 and (e) 1.50 at% ZnO: B thin films deposited at various T_s 88

Figure 5.14: Variation of transmittance with wavelength for ZnO and ZnO: B thin films deposited at T_s=450°C 89

Figure 5.15: Variation of absorption co-efficient with photon energy for (a) ZnO, (b) 0.50, (c) 0.75, (d) 1.00 and (e) 1.50 at% ZnO: B thin films deposited at various T_s 90

Figure 5.16: Tauc plots of (a) ZnO, (b) 0.50, (c) 0.75, (d) 1.00 and (e) 1.50 at% ZnO: B thin films deposited at various T_s 92

Figure 5.17: Variation of optical band gaps with B concentrations in ZnO thin films deposited at various T_s 93

Figure 5.18: Variation of refractive index with wavelength for (a) ZnO, (b) 0.50, (c) 0.75, (d) 1.00 and (e) 1.5 at% ZnO: B thin films deposited at various T_s 95

Figure 5.19: Variation of extinction coefficient (k) with wavelength for (a) ZnO, (b) 0.50, (c) 0.75, (d) 1.00 and (e) 1.50 at% ZnO: B thin films deposited at various T_s 96

Figure 5.20: Variation of optical conductivity with photon energy for (a) ZnO, (b) 0.50, (c) 0.75, (d) 1.00 and (e) 1.50 at% ZnO: B thin films deposited at various T_s 98

Figure 5.21: Variation of real part of dielectric constant with wavelength for (a) ZnO, (b) 0.50, (c) 0.75, (d) 1.00 and (e) 1.50 at% ZnO: B thin films deposited at various T_s 100

Figure 5.22: Variation of imaginary part of dielectric constant with wavelength for (a) ZnO, (b) 0.50, (c) 0.75, (d) 1.00 and (e) 1.50 at% ZnO: B thin films deposited at various T_s 101

Figure 5.23: Variation of dielectric loss tangent with wavelength for (a) ZnO, (b) 0.50, (c) 0.75, (d) 1.00 and (e) 1.50 at% ZnO: B thin films deposited at various T_s 102

Figure 5.24: I-V characteristic graphs of (a) ZnO, (b) 0.50, (c) 0.75, (d) 1.00 and (e) 1.50 at% ZnO: B thin films deposited at various T_s 104

Figure 5.25: Variation of resistivity of ZnO thin films with (a) B concentration and (b) substrate temperature 105
Figure 5.26: Electrical conductivity versus 1000/T graphs of ZnO and ZnO: B thin films deposited at (a) 300, (b) 350, (c) 400 and (d) 450 ^{o}C 106
Figure 5.27: Variation of activation energy with B concentration for ZnO: B thin films 106

LIST OF TABLES **Pages**

Table: 1. Basic properties of ZnO 11

Table: 2. Static (ε_o) and high frequency dielectric constant (ε_∞) data for ZnO [10, 11]. 16

Table: 3. Properties of boron 17

Table: 4. The EDX analysis of ZnO and ZnO: B thin films 83

Table: 5. Lattice constants of ZnO and ZnO: B thin films deposited at various T_s 86

Table: 6. c/a ratio for ZnO and ZnO: B thin films deposited at various T_s 86

Table: 7. Refractive index for ZnO and ZnO: B thin films deposited at various T_s 94

LIST OF ABBREVIATIONS

Symbol	Description
θ	Bragg angle
λ	Photon wavelength
d_{hkl}	Interplanar spacing
a	Lattice constant
D	Crystallite size
β	Full width half maximum of the highest peak in XRD pattern
ε	Microstrain
δ	Dislocation density
A	Absorbance
T	Transmittance
α	Absorption co-efficient
ν	Frequency of photon
h	Planck‟s constants
B	Tauc parameter
n	Refractive index
k	Extinction co-efficient
ε_r	Real part of refractive index
ε_i	Imaginary part of refractive index
R	Reflectance
ζ_{opt}	Optical conductivity
c	Speed of light
ρ	Electrical resistivity
ζ	Electrical conductivity
K_B	Boltzman constant
ΔE	Activation energy
K	Kelvin
d	Thickness

CHAPTER 1

INTRODUCTION

CHAPTER 1

INTRODUCTION

1.1 Introduction

Transparent conducting oxide (TCO) thin films have been an interesting topic in the field of materials research in past years. Among the other TCO‟s, Zinc oxide (ZnO) is a popular one due to its interesting structural, chemical, optical, electrical, etc. properties. Research work based on synthesis and characterization of ZnO and ZnO-based alloys (such as AlZnO, BZnO, CuZnO, MgZnO, CdZnO, CoZnO, MnZnO, etc.) are being encouraged more and more in recent years. ZnO has many practical applications such as light-emitting diodes (LEDs), ultraviolet (UV) photodetectors, UV-blue semiconductor laser, window layers, heat reflectors in solar cells, flat panel displays, electro-chromic devices, various gas sensors, surface acoustic wave devices, etc. [1-6]. Growth and characterization of ZnO crystal were being investigated extensively in the early years from 1950-1960 [7]. In early 1990‟s the research wave for this material was accelerated by the demand of new opto-electronic devices. Because of the unique characteristics, ZnO is considered to be a very promising alternative of III-V compound semiconductors (such as GaN, GaAs, InAs, etc) for fabrication of opto-electronic devices in the blue to UV range. Most of the recent interests on ZnO materials have been focused on the future potentials of UV-blue LEDs and UV-blue lasers.

ZnO is a II-VI compound semiconductor with some important properties. The crystalline structure of ZnO is hexagonal wurtzite type with lattice constants of a=3.253 Å and c=5.215 Å [8]. It has large exciton binding energy of 60 meV and direct band gap energy of 3.3 eV at room temperature [8, 9]. It has high transparency, high electron mobility, n-type electrical conductivity and low resistivity [9, 10]. Such attractive properties make it useful in fabrication of UV laser diode and other exciton related LEDs to be operated at room temperature. ZnO is one of the “hardest” materials in II-VI compound semiconductors due to

the higher melting point and larger cohesive energy. The constituent elements of ZnO are abundant and relatively of low cost. It is nontoxic, thus causes no harmful effect to the environment. Interfacial energy between ZnO and sapphire or other oxide substrates is such that two-dimensional growth is favored, which results in high quality films at lower temperature.

Various deposition techniques, such as chemical vapor deposition (CVD) [10], pulsed laser deposition (PLD) [11], rf-magnetron sputtering [12], Sol-gel [13], molecular beam epitaxy (MBE) [14], spray pyrolysis [15], atomic layer deposition [16], etc. have been used to synthesize ZnO thin films. Each of the techniques has its advantages and limitations. Spray pyrolysis technique (SPT) is one of the simplest and low cost techniques among the different methods. Besides, this technique might be used for large-area thin film deposition without any high vacuum system.

ZnO and doped ZnO thin films are being synthesized and characterized elaborately in last few years. ZnO can form alloy with many transition metals (Cr, Mn, Fe, Co, Ni, Cu, etc.), poor metals (Al, Ga, Cd, In, etc.) and non-metals (B, N, F, etc.). Doping causes changes in structural, optical and electrical properties of ZnO. The main purposes for the preparation of ZnO alloys are band gap tuning and construction of the super-lattice hetero-structures with less lattice mismatches. The fabrication and characterization of these hetero-structures are key to realization of ZnO-based devices as the alternatives for III-V semiconductors (such as GaN, GaAs). For example Mg doping in ZnO causes increase in band gap value. Band gap shifts in ZnO due to doping may be attributed to Berstain-Moss (BM) effect [17, 18]. When Mg ions substitute Zn ions in their regular lattice sites and the number of conducting carriers increase in the structure, the band structure of ZnO is strongly affected. As a consequence the band gap value is increased due to Mg doping. Although the common stable phases of ZnO has hexagonal and MgO has cubic crystal structures, these two materials can still be alloyed

with each other to form MgO-ZnO compounds. The crystal structures of such alloys can be either hexagonal wurtzite type or fcc depending on the relative concentrations of Mg and Zn. Research on ZnO- based alloys may reveal some unique features of ZnO and extend its field of application.

1.2 A Brief Review of Research on Zinc Oxide Thin Films

Pure ZnO thin films [19] were prepared on silicon (1 0 0) and fused silica substrates by chemical SPT at various substrate temperatures. It was found that at low temperature the growth rate was controlled by activated process. Maximum growth rate of 15.01 nm/min was obtained at the substrate temperature 543 K and the ZnO thin films were very smooth with preferred c-axis orientation, high electrical resistivity (~ 400 Ω-cm) and an optical transmittance of 90 %. At higher substrate temperature the film surfaces were rough. All the ZnO thin films prepared at 473 K showed polycrystalline hexagonal wurtzite structure. Optical band gap of ZnO thin films was found between 3.33 and 3.31 eV with the increase of substrate temperature from 473 to 573 K. Godbole *et. al.* [20] prepared ZnO thin films on glass substrates by SPT at the substrate temperature of 400 °C. They characterized ZnO thin films of different thicknesses by X-ray diffraction (XRD) and atomic force microscopy (AFM). They found polycrystalline nature of the thin films in XRD analysis. The grain size decreased and roughness of the film increased with the increase the film thickness. From the resistivity-temperature measurements they found that the activation energy decreased with the increase in thickness of the film. ZnO thin films were prepared [4] from methanolic solution of zinc acetyl-acetonate as a precursor and sapphire (0 0 1) as a substrate by SPT. XRD analysis revealed polycrystalline character of prepared films with preferential growth orientation along c-axis. The roughness of prepared films was assessed by AFM and represented by roughness root mean square (RMS) value in the range of 1.8 - 433 nm. The

surface morphology was mapped by SEM showing periodical structure with several local defects. ZnO films were transparent in the UV region and the band gap of was found to be 3.35 eV. Raman spectroscopy confirmed wurtzite structure and the presence of compressive stress within its structure as well as the occurrence of oxygen vacancies. The resistivity of ZnO films was measured by Van der Pauw method. Resistivity was found to be 8×10^{-2} Ω-cm with carrier density of 1.3×10^{18} cm^{-3} and electron mobility of 40 $cm^{2}V^{-1}$ s^{-1}. Kumar *et al.* [21] prepared polycrystalline ZnO thin films on glass substrate at the substrate temperature of 250 °C using aqueous solution of zinc acetate by SPT. The result of XRD clearly revealed polycrystalline nature of ZnO films with hexagonal wurtzite structure with the (0 0 2) preferential orientation and the grain size was computed to be 0.43 nm. The films exhibited excellent optical properties with transmittance of about 80 %, low absorbance and reflectance in the visible region. Refractive index, extinction co-efficient and energy band gap were calculated and the developed films had a direct band gap value of 3.2 eV. Islam *et al.* [22] prepared ZnO thin films of different thicknesses SPT onto glass substrate at 200 °C from an aqueous zinc acetate solution. SEM micrograph shows that films are uniform and nanofiber structures appear around the nucleation center. The films show direct band gap between 3.3 and 3.4 eV. The films exhibit low absorbance in the vis-NIR region from 450 to 1000 nm. Salaken *et al.* [23] studied the structural and optical properties of Fe-doped ZnO thin films prepared by SPT. Results of the XRD analysis suggested that the doped Fe ions exist mainly in the form of Fe^{3+} as $FeCl_3$ was used as dopant and the preferred orientation was along (1 0 1) direction. SEM and UV-vis spectroscopy revealed that ZnO the film was more homogeneous and more transparent for 3 at% Fe-incorporation. Taskin *et al.* [24] investigated the structural and optical properties of Co-doped ZnO thin films synthesized by SPT with different dopant concentrations. Co-doped ZnO films showed good crystalline structure suggesting the substitution of Zn ion by Co ion as evident from XRD and UV-vis

spectrum. Nanofibers were observed in both pure and Co doped ZnO thin films by SEM. The optical transmissions of the films were found to decrease from 80 to 70 % with the increase of Co doping. The films showed a decrease in direct band gap with increasing doping concentration in the range 3.2 – 2.7 eV. The conductivity increased with the increase of Co concentration.

Textured and low-resistivity ZnO thin films [10] were prepared onto glass substrate by metalorganic chemical vapor deposition (MOCVD) at the substrate temperatures between 100 and 300 °C. The B_2H_6 gas was used for an n-type doping. It was found that the electrical properties of films were strongly dependent on growth conditions and film thickness. The film with the thickness 2 μm deposited at the substrate temperature of 150 °C had the sheet resistivity of 10 Ω-cm. The crystal orientation and grain structure changed with the increase of B_2H_6 flow rate. Kumar *et al.* [25] reported the structural, transport and optical properties of ZnO: B thin films grown on glass substrate by sol-gel spin coating process. It is observed from the XRD analysis results that the crystalline quality of the film is improved with increasing B concentration. A crystallite size of ~17 nm is obtained for B doped films. A minimum resistivity of 7.9×10^{-4} Ω-cm is formed at 0.6 at% of B concentration in the ZnO: B films. Optical interference pattern in transmittance spectra shows good homogeneity with a transparency of ~ 88% in the visible region and the band gap of the films is increased from 3.24 to 3.35 eV with increasing B concentration. Avis *et al.* [26] studied the effect of B doping on the structural and electrical properties of ZnO thin films deposited on glass substrate by DC magnetron sputtering method. XRD and Raman intensities were analyzed to see the change in the structure and Hall Effect was measured to have an insight into the carrier concentration and the Hall mobility for the B doped ZnO films. B doped ZnO film exhibited a sheet resistance of 0.9 kΩ/square, Hall mobility of 22 cm^2/Vs and carrier concentration of 4.8×10^{19} cm^{-3}.

Undoped and boron (B) doped ZnO (ZnO: B) thin films [27] were prepared by SPT. The films obtained with 0.8 wt% doping of B exhibited low resistivity and average transmittance was found to be 90 %. XRD analysis showed that the ZnO: B thin films were crystalline and well oriented along the (0 0 2) plane. Highly transparent and conducting ZnO: B thin films were deposited by Yadav *et al.* [28] using spray CVD technique. The structural analysis showed that the films were polycrystalline with preferential orientation along [0 0 2] direction. For 0.8 at% B doping concentration the films exhibited higher carrier concentration $\approx 10^{20}$ cm^{-3} with lower resistivity of 0.39×10^{-3} Ω-cm and optical transmittance ≈ 90%. Pawar *et al.* [29] prepared highly transparent and conducting ZnO: B thin films on glass substrate using chemical SPT. Low angle XRD analysis showed that the films were polycrystalline with a hexagonal wurtzite structure and had preferred orientation in [0 0 2] direction. The films with resistivity 2.54×10^{-3} Ω-cm and optical transmittance ~ 90% were obtained at 1 at% B doping concentration. The optical band gap of ZnO: B films were found to be 3.27 eV. On the basis of the literature survey it is seen that a lot of research work has been carried on the preparation and characterization of pure and doped ZnO thin films. A range of deposition techniques have been used for the synthesis of B doped ZnO thin films under various deposition conditions. The effect of variation of substrate temperature and film thickness on the structural, optical and electrical properties of B doped ZnO thin films deposited by SPT have not been explored extensively. So, the aim of the present work is to study those above mentioned properties elaborately.

1.3 Objectives of The Present Work

The objectives of the present study are to synthesize ZnO and ZnO: B thin films by locally fabricated SP system and to characterize those thin films by using various experimental techniques. The effect of substrate temperature and dopant concentration on the

structural, optical and electrical properties of the thin films is to be studied elaborately. Because the quality of thin films can be controlled by controlling these parameters, the thin films from aqueous solutions might have great advantages on economy and capacity of large area deposition. It is expected that optically transparent and homogeneous thin films can be synthesized by using this low cost technique. These thin films may have expected electrical and optical properties to find applications in sensors, electronic and optoelectronic devices, etc.

In the present work ZnO and ZnO: B thin films would be synthesized on to glass substrate by a SPT. Based on these research challenges discussed above, the objectives of this work are as follows:

1. ZnO and ZnO: B thin films would be synthesized at various substrate temperatures with different B concentrations.
2. Surface morphology of the ZnO and ZnO: B thin films would be studied by scanning electron microscopy (SEM).
3. Chemical composition of the ZnO and ZnO: B thin films will be studied by energy dispersive X-ray (EDX) analysis.
4. Crystal structure of the ZnO and ZnO: B thin films would be studied by XRD.
5. Direct current (DC) electrical conductivity of the thin films would be determined by linear four point probe method.
6. Transmittance, absorbance, optical absorption coefficient, optical band gap (E_g), refractive index, dielectric constants, etc. would be determined from UV-visible spectra.

Finally, the structure-property behavior in relation to B concentration and substrate temperature would be discussed. This may indicate a better scope to find applications of the material in different devices.

References

[1] Nakamura, S., Fasol, G., “The Blue Laser Diode”, Springer: Berlin, (1997).

[2] Bagnall, D. M., Chen, Y. F., Zhu, Z., Yao, T., Koyama, S., Shen, M. Y., Goto, T., “Optically pumped lasing of ZnO at room temperature”, Appl. Phys. Lett., 70, 2230-2232, (1997).

[3] Tripathi, B., Patel, M., Ray, A., Kumar, M., “Influence of optical properties of ZnO thin films deposited by spray pyrolysis and rf magnetron sputtering on the output performance of silicon solar cell”, IOP Conf. Series: Mater. Sci. Eng.43, 012002, 1-5, (2013).

[4] Nádherný, L., Sofer, Z., Sedmidubský, D., Jankovský, O. Mikulics, M., “ZnO thin films prepared by spray-pyrolysis technique from organo-metallic precursor”, Ceramics – Silikáty, 56 (2), 117- 121, (2012).

[5] Shakti, N., Gupta, P.S., “Structural and Optical Properties of Sol-gel Prepared ZnO Thin Film”, Appl. Phys. Res. 2 (1), 21, (2010).

[6] Gorla, C. R., Emanetoglu, N.W., Liang, S., Mayo, W.E., Lu, Y., Wraback, M., Shen, H., “Structural, optical, and surface acoustic wave properties of epitaxial ZnO films grown on (01$\bar{1}$2) sapphire by metalorganic chemical vapor deposition”, J. Appl. Phys. 85, 2595, (1999).

[7] White, E. A. D., “Current Topics in Materials Science”, Vol.3 (edited by E. Kaldis), North-Holland Publishing Company: Amsterdam, (1981).

[8] Khan, Z. R., Khan, M. S., Zulfequar, M., Khan, M. S., “Optical and Structural Properties of ZnO Thin Films Fabricated by Sol-Gel Method”, Mater. Sci. Appl. 2, 340-345, (2011).

[9] Janotti, A., Van de Walle, C.G., “Fundamentals of zinc oxide as a semiconductor”, Rep. Prog. Phys., 72, 126501,1-29, (2009)

[10] Wenas, W.W., Yamada, A., Takahashi, K., Yoshino, M., Konagai, M., “Electrical and optical properties of boron-doped ZnO thin films for solar cells grown by metalorganic chemical vapor deposition”, J. Appl. Phys., 70(11), 7119- 7123, (1991).

[11] Zhao, L., Lian, J., Liu, Y., Jiang, Q., "Structural and optical properties of ZnO thin films deposited on quartz glass by pulsed laser deposition", Appl. Surf. Sci., 252, 8451-8455, (2006).

[12] Kim, K. K., Song, J. H., Jung, H. J., Park, S. J., "The grain size effects on the photoluminescence of ZnO/α-Al_2O_3 grown by radio-frequency magnetron sputtering", J. Appl. Phys., 87, 3573- 3575, (2000).

[13] Nagase, T., Ooie, T., Nakatsuka, Y., Shinozaki, K., Mizutani, N., "A Novel Method for the Preparation of Green Photoluminescent Undoped Zinc Oxide Film Involving Excimer Laser Irradiation of a Sol-Gel-Derived Precursor", Jpn. J. Appl. Phys., 39, L713-L715 (2000).

[14] Chen, Y. F., Bagnall, D., Yao, T. F., "ZnO as a novel photonic material for the UV region", Mater. Sci. Eng. B. 75, 190- 198, (2000).

[15] Studenikin, S. A., Golego, N., Cocivera, M., "Optical and electrical properties of undoped ZnO films grown by spray pyrolysis of zinc nitrate solution", J. Appl. Phys. 83, 2104-2111, (1998).

[16] Yamada, A., Konagai, M., "Atomic Layer Deposition of ZnO Films and Their Application to Solar Cells", Sol. Stat. Phenomena. 67(8), 237-248, (1999).

[17] Burstein, E., "Anoma1ous Optical Absorption Limit in InSb", Phys.Rev., 93, 632-633, (1954).

[18] Ziabari, A. A., Rozati, S.M., "Carrier transport and band gap shift in n-type degenerate ZnO thin films: The effect of band edge Nonparabolicity", Physica B., 407, 4512–4517, (2012).

[19] Ayouchi, R., Martin, F., Leinen, D., Barrado, J. R. R., "Growth of pure ZnO thin films prepared by chemical spray pyrolysis on silicon", J. Cryst. Growth, 247, 497-504, (2003).

[20] Godbole, B., Badera, N., Shrivastava, S., Jain, D., Ganesan, V., "Growth Mechanism of ZnO Films Deposited by Spray Pyrolysis Technique", Mater. Sci. Appl., 2, 643- 648, (2011).

[21] Kumar, R. A., Manivannan, V., Krishnaraj, S., "Growth and Characterization of ZnO Nano thin films using Spray Pyrolysis", Int. J. Res. Pure Appl. Phys., 3(4), 39-42, (2013).

[22] Islam, M. R., Podder, J., "Optical properties of ZnO nano fiber thin films grown by spray pyrolysis of zinc acetate precursor", Cryst. Res. Technol., 44(3), 286-292, (2009).

[23] Salaken, S. M., Farzana, E., Podder, J., "Effect of Fe-doping on the structural and optical properties of ZnO thin films prepared by spray pyrolysis", J. Semicon., 34(7), 073003,1-6, (2013).

[24] Taskin, M., Podder, J., "Structural, Optical and Electrical Properties of Pure and Co-Doped ZnO Nano Fiber Thin Films Prepared by Spray Pyrolysis", App. Sci. Report. 2 (3), 107-113, (2014).

[25] Kumar, V., Singh, R.G., Purohit, L.P., Mehra, R.M., "Structural, Transport and Optical Properties of Boron-doped Zinc Oxide Nanocrystalline", J. Mater. Sci. Technol., 27(6), 481-488, (2011).

[26] Avis, C., Kim, S. H., Kim, K. H., Jang, J., Hong, S. J., Nam, Y. D., Hur, J. H., "B-Ion Doping Effect in ZnO Thin-Films", J. Korean Phys. Soc. 54(1), 535-538, (2009).

[27] Lokhande, B. J., Patil, P.S., Uplane, M.D. "Studies on structural, optical and electrical properties of boron doped zinc oxide films prepared by spray pyrolysis technique", Physica B., 302–303, 59-63, (2001).

[28] Yadav, S. C., Uplane, M. D., "Synthesis and properties of Boron doped ZnO thin films by spray CVD technique at low substrate temperature", Int. J. Eng. Sci. Technol., 4(12), 4893-4898, (2012).

[29] Pawar, B. N., Jadkar, S.R., Takwale, M.G., "Deposition and characterization of transparent and conductive sprayed ZnO: B thin films", J. Phys. Chem. Sol., 66, 1779-1782, (2005).

CHAPTER 2

MATERIALS AND DEPOSITION TECHNIQUES

CHAPTER 2

MATERIALS AND DEPOSITION TECHNIQUES

In this chapter, basic properties and applications of ZnO are discussed in brief. The structural, optical and electrical properties of ZnO are discussed in details. In this work, B has been used as the dopant material. So, it is very important to know the basic properties of B and its oxide compound (B_2O_3). There is a short discussion on B in this chapter. Basic principles of various this film deposition techniques are also been discussed later.

2.1 Properties of Zinc Oxide

ZnO has attracted much attention of the scientists as a promising material. ZnO has been widely studied since the year 1935 [1]. ZnO based electronic and optoelectronic devices are very popular. It is a very nice coating material and also used in pressure sensors. There are many more uses of ZnO which make it an important material for research. Table: 1 shows some basic properties of ZnO.

Table: 1. Basic properties of ZnO

Name of the Property	Value/Type
Molecular formula	ZnO
Material type	II-VI compound semiconductor
Molar mass	81.408 g/mol
Appearance	White solid
Odor	Odorless
Density	5.606 g/cm^3
Melting point	1975 °C (decomposes)
Boiling point	1975 °C (decomposes)
Solubility in water	Insoluble
Band gap (room temperature)	3.3 eV (direct)
Exciton binding energy (room temperature)	60 meV
Dielectric constant	8.5
Refractive index(n_D)	2.0041

From Table 1 it is seen that ZnO has a wide band gap of 3.3 eV and a large exciton binding energy of 60 meV at room temperature. These two properties make ZnO an important material for blue and ultra-violet optical devices. ZnO has several advantages over gallium nitride (GaN) in this application range. ZnO has the ability to grow on single crystal substrates. ZnO is non-toxic and thermally stable; hence it is widely used as coating material. There are some other good aspects of ZnO such as its broad chemistry leading to many opportunities for wet chemical etching, low power threshold for optical pumping, radiation hardness and biocompatibility. Collectively, these properties of ZnO make it one of the ideal candidates for a variety of devices. Its applications range from sensors and ultra-violet laser diodes to display systems. Extensive research on ZnO and the alloys based on ZnO may discover more new type of applications of the material.

2.1.1 Structure of zinc oxide

ZnO shows crystallization in two major forms, hexagonal wurtzite [2] and cubic zincblende. The wurtzite structure is most stable at ambient conditions and thus most commonly found in ZnO. The zincblende form can be stabilized by growing ZnO on substrates with cubic lattice structure. For both the cases, the Zn and O form tetrahedrons, the most characteristic geometry for Zn (II). ZnO converts to the rocksalt motif at relatively high pressures about 10 GPa [3]. Hexagonal and zincblende polymorphs have no inversion symmetry. Lattice symmetry properties result in piezoelectricity of the hexagonal and zincblende ZnO, and pyroelectricity of hexagonal ZnO. The lattice constants are a = 3.25 Å and c = 5.2 Å; their ratio c/a ~ 1.60 is close to the ideal value for hexagonal cell c/a = 1.633 [4]. As in most group II-VI materials, the bonding in ZnO is largely ionic (Zn^{2+}–O^{2-}). The radii of Zn^{2+} and O^{2-} are 0.074 nm and 0.140 nm, respectively. This property accounts for the preferential formation of

wurtzite rather than zincblende structure [5] as well as the strong piezoelectricity of ZnO. Because of the polar Zn-O bonds, Zn and O planes are electrically charged.

Figure 2.1 shows a hexagonal wurtzite unit cell of ZnO. The number of the nearest neighbors in wurtzite is four. Each O (or Zn) ion is tetrahedrally surrounded by four Zn (or O) ions. Furthermore each ion also has twelve next-nearest neighbors of the same type of ions. The O-Zn distance of the nearest neighbors is 1.992 Å in the direction parallel to the c-axis of the hexagonal unit cell and 1.973 Å in the other three directions of the tetrahedral arrangement [6]. The tetrahedral arrangement of the nearest neighbors indicates the covalent bond between the Zn and O atoms. The covalent radii of Zn and O were reported to be 1.31 Å and 0.66 Å, respectively [7] ZnO is an- isotropic crystal with the symmetry of point group of C6v (or 6mm). Group C6v is the point group of the hexagonal wurtzite structure, which includes rotations by ±60°, ±120°, and ±180° around the hexagonal axis and two sets of three equivalent mirror planes that are parallel to the hexagonal axis.

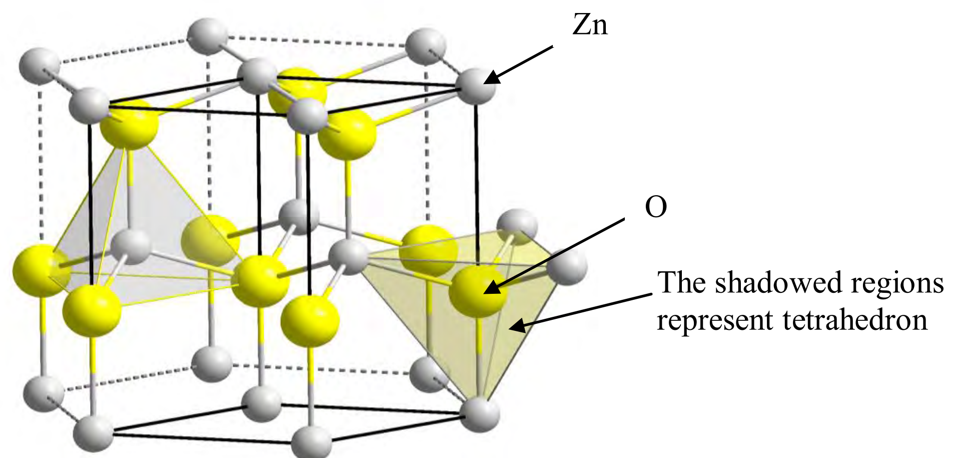

Figure 2.1: The hexagonal wurtzite structure of ZnO

There are 12 phonon modes corresponding to 4 atoms per unit cell in a single crystal wurtzite ZnO. Phonon modes are important for understanding the thermal, electrical and optical properties of the crystal. There are one longitudinal acoustic (LA), two transverse-acoustic

(TA), three longitudinal-optical (LO) and six transverse-optical (TO) branches. The $A1$ and $E1$ branches are Raman and infrared active, while the two $E2$ branches (non-polar) are only Raman active. The E_2^{low} mode is associated with the vibrations of the Zn sub-lattice, whilst the E_2^{high} mode is associated with the oxygen atoms only. The B_1 branches are always inactive. The phonon modes of ZnO have been extensively studied and modeled.

2.1.2 Optical properties

Energy Band structure and lattice dynamics influence the optical properties of ZnO very strongly. To understand optical properties of ZnO it is necessary to know the excitonic behavior of the material. Excitonic recombinations in bulk *n*-type ZnO is explained nicely by the work of Meyer et al. [8]. This work gives a comprehensive treatment and analysis of the excitonic spectra obtained from ZnO, and assigns many defect related spectral features and donor–acceptor pair (DAP) emission. A broad defect related peak extending from about 1.9 to 2.8 eV is also a common optical feature of ZnO. Known as the green band, the origin of its luminescence is still not well understood and has in the past been attributed to a variety of different impurities and defects. Figure 2.2 shows a typical photoluminescence spectra of *n*-type ZnO measured at 4.2 K. The excitonic, DAP and extended green band emission can all be clearly seen, as can the phonon replicas produced from the LO phonons. Due to the lack of available data on *p*-type ZnO, a corresponding spectrum is not shown here.

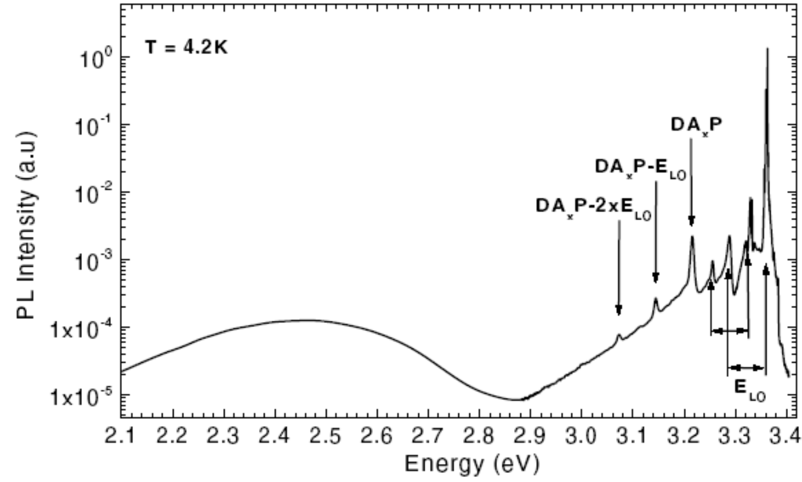

Figure 2.2: Photoluminescence spectrum of *n*-type bulk ZnO (HeCd excitation) showing excitonic, donor acceptor pair and green-band emission [8]

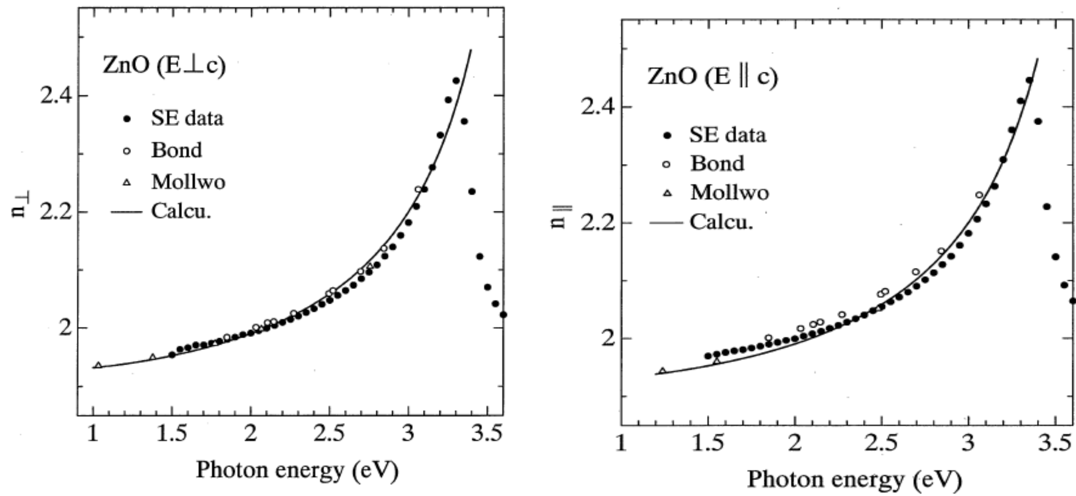

Figure 2.3: Refractive-index dispersion of ZnO for (a) E ⊥c and (b) E $_{\|}$ c below the fundamental absorption edge [9]

Numbers of works have been reported on the determination of fundamental optical properties of ZnO, such as refractive index and dielectric constants of this material [9-11]. The measurements are all carried out using spectroscopic ellipsometry. The values have been determined for the dielectric constants of ZnO are shown in Table: 2.

Table: 2. Static (ε_o) and high frequency dielectric constant (ε_∞) data for ZnO [10, 11].

		Film [10]	Bulk [10]	Bulk [9]
ε_o	E ⊥ C	7.46	7.77	
	E ∥ C	8.59	8.91	
ε_∞	E ⊥ C	3.7	3.6	3.68
	E ∥ C	3.78	3.66	3.72

2.1.3 Electrical properties

ZnO is an n-type semiconductor. The electrical properties of ZnO vary a lot due to carrier concentration. The background carrier concentration depends a lot upon the quality of the layers, but is usually~10^{16} cm^{-3}. The largest reported n-type doping is ~10^{20} electrons cm^{-3} and largest reported p-type doping is ~10^{19} holes cm^{-3}. But such a heavy doping cause high level of p-type conductivity and has not been verified experimentally [12]. ZnO has the value of exciton binding energy (60 meV) at room temperature (300 K). Such a large value of exciton binding makes ZnO very suitable in fabrication of optoelectronic devices. ZnO has a large and direct band gap of 3.3 eV at 300 K which makes useful for high power and high temperature operations. The ZnO-devices make less noise; have high breakdown voltage and ability to sustain large electric field. The electron effective mass is $0.24m_0$, and the hole effective mass is $0.59m_0$. The corresponding electron Hall mobility at 300K for low *n*-type conductivity is μ=200 cm^2 V^{-1} s^{-1}, and for low *p*-type conductivity is 5–50 cm^2 V^{-1} s^{-} [13].

2.2 Properties of Boron

Boron (B) is a metalloid with the atomic number 5. It is the only non-metal in group 13 of the periodic table. General properties of B are showed in the Table: 3. B is similar to carbon (C) in its capability to form stable covalently bonded molecular networks. Even nominally disordered (amorphous) B contains regular B icosahedra which are, however, bonded randomly to each other without long-range order. Crystalline B is a very hard, black material with a high melting point of above 2000 °C. It exists in four major polymorphs: á-

rhombohedral and â-rhombohedral (á-R and â-R), ã and â-tetragonal (â-T); á-tetragonal phase also exists (á-T), but is very difficult to produce without significant contamination. â-rhombohedral B is the most thermodynamically stable allotrope of B [14].

Table: 3. Properties of boron

Name of the property	**Value/ Type**
Atomic mass	10.81
Crystal structure	Rhombohedral
Allotropes	α-, β-Rhombohedral, β-Tetragonal, γ-Orthorhombic
Appearance	Black-brown
Phase	Solid
Density (when liquid at melting point)	$2.08\ g{\cdot}cm^{-3}$
Melting point	2076 °C
Boiling point	3927 °C
Atomic radius	0.09 nm (empirical)
Ionic radius	0.041 nm
Electrical resistivity	$\sim 10^{6}\ \Omega{\cdot}m$ (at 20 °C)

Chemically, B behaves more similarly to silicon than to aluminum. Crystalline B is chemically inert and resistant to attack by boiling hydrofluoric or hydrochloric acid. The rate of oxidation of B depends upon the crystallinity, particle size, purity and temperature. B does not react with air at room temperature, but at higher temperatures it burns to form B trioxide (B_2O_3) [15]. B is a very suitable candidate for p-type doping in semiconductors. Because it has three valance electron and can easily contribute holes to the material and help to increase p-type conductivity. But, in the case of ZnO it acts as n type doping since it replaces Zn in its lattice sites.

2.3 Applications of Zinc Oxide

ZnO is an attractive material for applications in electronics, photonics, sensing and acoustics. It is a key element in various industrialized processes such as paints, cosmetics, pharmaceuticals, plastics, batteries, electrical equipment, rubber, soap, textiles, floor

coverings, etc. Growth technologies of ZnO single crystals, epitaxial layers, nanostructures, and nanoparticles are improving day by day. In future, ZnO devices will become increasingly functional and exotic. ZnO-based nanostructures including nanowire arrays hold a host of opportunities for flat screen displays, field emission sources, gas, chemical [16] and biological sensors, and as UV light emitters and switches [16–19]. Epitaxial layers and single crystals will be important for the development of optoelectronic (blue and ultraviolet light emitters and detectors) [20], piezoelectric [21] and spintronic [22] devices, and together with GaN may form the light source of the 21st century [23]. Epitaxial layers of ZnO are promising forms of semi-conducting transparent thin film [24], which again can be significant for solar cells, gas sensors, displays and wavelength selective applications. ZnO nanoparticles have caused revolution in the development of improved sunscreens, paints and coatings to name just a few. Additionally, the radiation hardness of ZnO to high energy proton irradiation makes it an ideal candidate for space applications [25].

ZnO already possesses a wide range of applications, due to its unique properties which are being explored and applied, recently. It can be predicted that in future ZnO devices will become necessary part of our everyday lives.

2.4 Thin Film Deposition Techniques

Thin films can be synthesized by several physical and chemical techniques. In this section, there will be a brief description of some commonly used deposition techniques for thin films on a variety of commercially available substrates. The following chart (Figure 2.4) represents the classifications of thin film deposition techniques precisely.

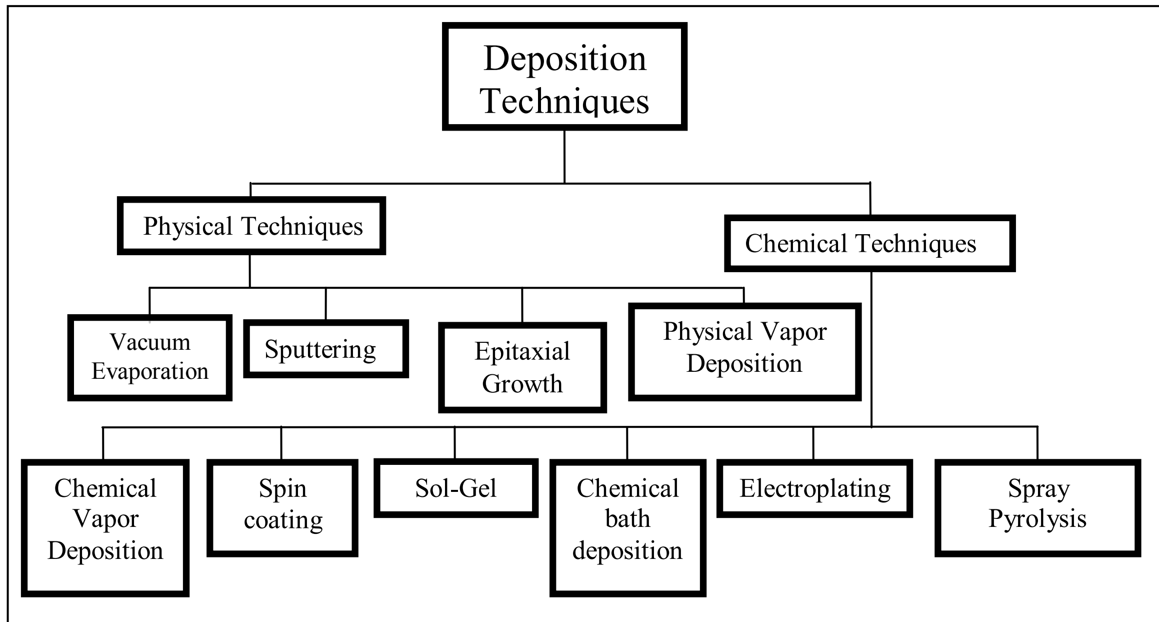

Figure 2.4: Types of deposition techniques

2.4.1 Physical techniques

Physical deposition uses mechanical or thermodynamic means to produce a thin film of solid. An everyday example is the formation of frost. Since most engineering materials are held together by relatively high energies, and chemical reactions are not used to store these energies, commercial physical deposition systems tend to require a low-pressure vapor environment to function properly.

2.4.1.1 Vacuum evaporation method

Vacuum evaporation is a well known and widely used technique of thin film preparation. In this technique, material is first thermally vaporized and then condensed on a substrate. Among the numerous deposition parameters substrate temperature, evaporation rate and the vacuum quality affect the microstructure and surface morphology of the coating. Thermal evaporation technique allows precise control over thickness multiplayer interface stacks of any complexity can be prepared with great precision. The evaporation of a material required to be heated at a sufficiently high temperature to produce the desired

vapor pressure. The rate of free evaporation of a vapor atom from a clean surface of unit area in vacuum is given by the Langmuir-Dushman Kinetic theory equation [26].

$$N_e = 3.513\times10^{21}\ p_e/(MT)^{1/2}\quad [\text{ molecules cm}^{-2}\text{s}^{-1}]$$

where p_e is the equilibrium vapor pressure (in Torr) if the evaporation under saturated vapor conditions at a temperature T and M is the molecular weight of the vapor species. Vacuum evaporation requires a system with a known vacuum and its residual gas analysis. A diffusion pump backed by a rotary pump system continues to be the 10^{-6}- 10^{-8} Torr workhorse in thin film technology largely because of its modest price, simplicity, and high speed. By using special diffusion pump oil (e,g., polyphenyl ether), a cryogenic baffle, and an all-metal system, ultrahigh vacuum (UHV) in the range 10^{-8} -10^{-10} Torr are easily obtained. Vapor species may be created by kinetic ejection from the surface of a material (called target of cathode) by bombardment with energetic and nonreactive ions.

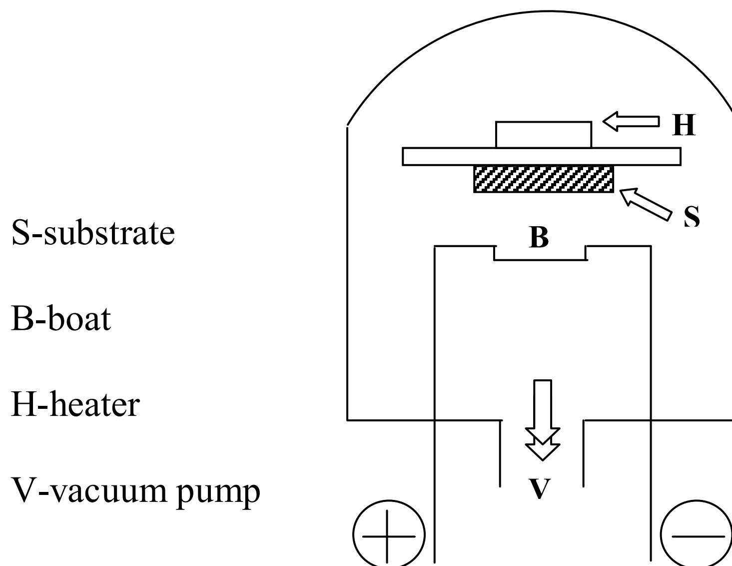

Figure 2.5: Schematic diagram of thermal or vacuum evaporation coating system

A simple arrangement of vacuum evaporation chamber is shown in Figure 2.5. The material to be evaporated lies in a high melting point metallic boat B through which a high current is

passed and the evaporated material is deposited on the substrate S attached to a heater H. This arrangement chamber is pumped to high vacuum, through V.

2.4.1.2 Sputtering

Sputtering [27] means the ejection of atoms from the surface of a material by bombardment with energetic particles. Figure 2.6 shows schematic diagram of sputtering system. During sputtering an atom or molecule is knocked out of a target material by accelerated ions which are produced from excited plasma. The atom or molecule is then condensed on a substrate either in its original or in a modified form. In sputtering the material is released from the source at much lower temperature than evaporation. The substrate is placed in a vacuum chamber with the source material, named a target, and an inert gas (such as argon) is introduced at low pressure.

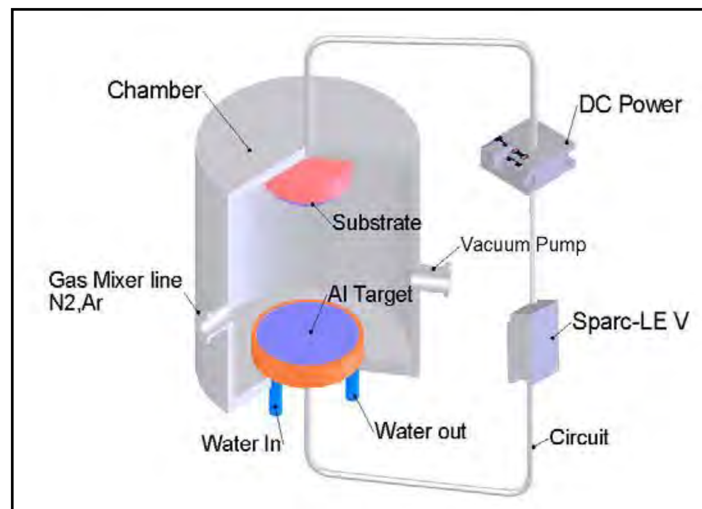

Figure 2.6: A diagram of sputtering system

The chemically inert atoms are ionized in a glow discharge which is called plasma. The gas ions are accelerated towards the surface of the target, causing atoms of the source material to break off from the target in vapor form and condense on all surfaces including the substrate. If the plasma ions are accelerated by a DC field then the sputtering technique is called DC and if an RF field is used then the technique is called RF sputtering. If magnets with alternating polarity are arranged behind or sometimes at the sides of the target to enable

lower pressures to be used and thus a cleaner film to be created, it is called magnetron sputtering. As for evaporation, the basic principle of sputtering is the same for all sputtering technologies.

2.4.1.3 Epitaxial growth

„Epitaxy" is a Greek word. „Epi" means on and „Taxi" means arrangement. Basically Epitaxy means growth of film with a crystallographic relationship between film and substrate. Among the various Epitaxial Growth methods, Molecular Beam Epitaxy (MBE) [28] is frequently used for its advantages over other methods. MBE is a technique for epitaxial growth via the interaction of one or several molecular or atomic beams that occur on a surface of a heated crystalline substrate .In Figure 2.7 a schematic diagram of a typical MBE system is shown. The solid sources materials are placed in evaporation cells to provide an angular distribution of atoms or molecules in a beam. The substrate is heated to the necessary temperature and, when needed, continuously rotated to improve the growth homogeneity. Ultra high vacuum (UHV) > 10^{-8} Pa is the essential environment for MBE. Therefore, the rate of gas evolution from the materials in the chamber has to be as low as possible. MBE can achieve precise control over both chemical composition and doping profile. Single crystal multi-layer structure with dimension in the order of atomic layers can be grown using MBE.

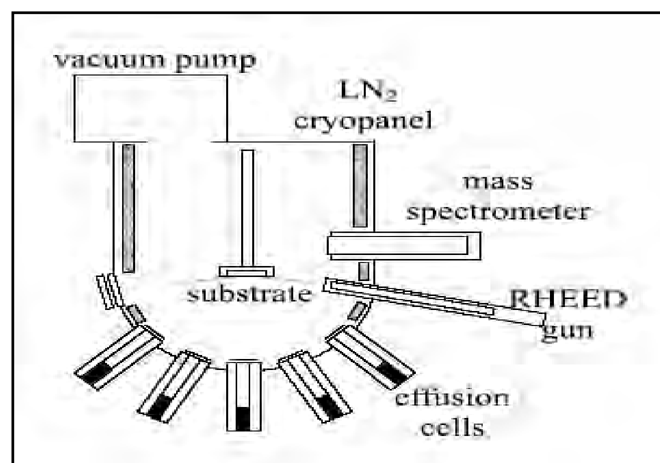

Figure 2.7: Schematic diagram of MBE system

2.4.1.4 Physical vapor deposition

Physical Vapor Deposition (PVD) [29] is a method to deposit thin films by the condensation of a vaporized material onto various surfaces (e.g., onto semiconductor wafers). The coating method involves purely physical processes such as high temperature vacuum evaporation rather than involving a chemical reaction at the surface to be coated as in chemical vapor deposition. One of the main industrial fields where PVD is extensively used is the fabrication of semiconductor devices. PVD covers a number of deposition technologies in which material is released from a source and transferred to the substrate. PVD comprises the standard technologies for deposition of metals. A typical PVD set up is shown in Figure 2.8.

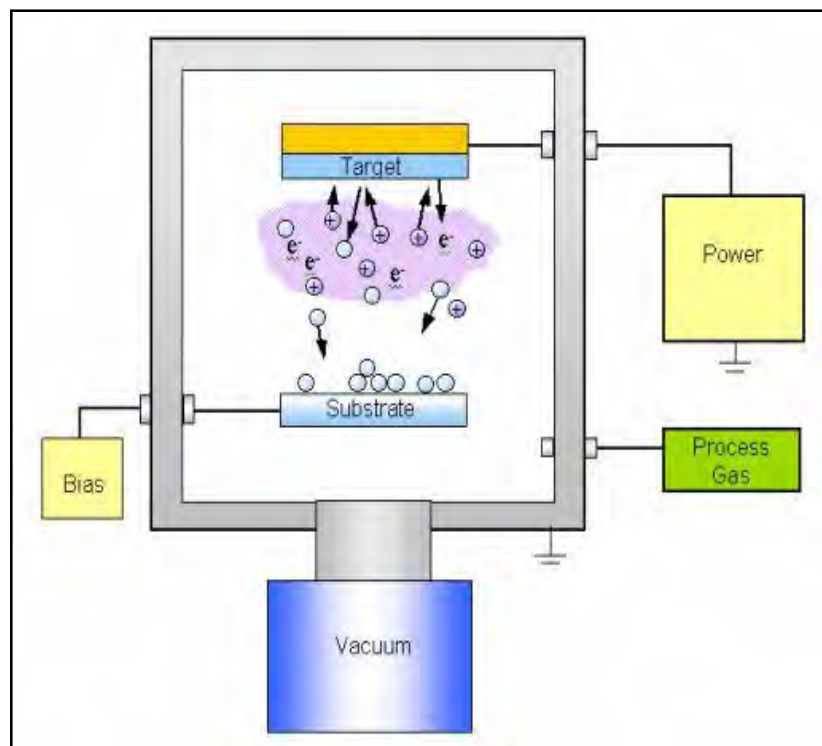

Figure 2.8: A diagram of physical vapor deposition technique

It is far more common than CVD for metals since it can be performed at lower process risk and cheaper in regards to materials cost. The quality of the films is inferior to CVD, which for metals means higher resistivity and for insulators more defects and traps. The step coverage is also not as good as CVD.

2.4.2 Chemical techniques

Here, a fluid precursor undergoes a chemical change at a solid surface, leaving a solid layer. An everyday example is the formation of soot on a cool object when it is placed inside a flame. Since the fluid surrounds the solid object, deposition happens on every surface, with little regard to direction; thin films from chemical deposition techniques tend to be conformal, rather than directional.

2.4.2.1 Chemical vapor deposition

Chemical Vapor Deposition (CVD) [30] is an extremely versatile process that can be used to process almost any metallic or ceramic compound. During CVD thin films are developed on a substrate by using chemical reactions. Reactive gases are supplied into a vacuum chamber at approximately ambient temperatures and these gases react on a substrate and form a thin film or a powder. The reactions though which form a solid material do not always occur on or close to the heated substrate, heterogeneous reactions, but in the gas phase as well, homogeneous reactions. Gaseous by-products are removed from the chamber. CVD coatings are usually only a few microns thick and are generally deposited at fairly slow rates, usually of the order of a few hundred microns per hour. A schematic diagram of CVD process is shown in Figure 2.9.

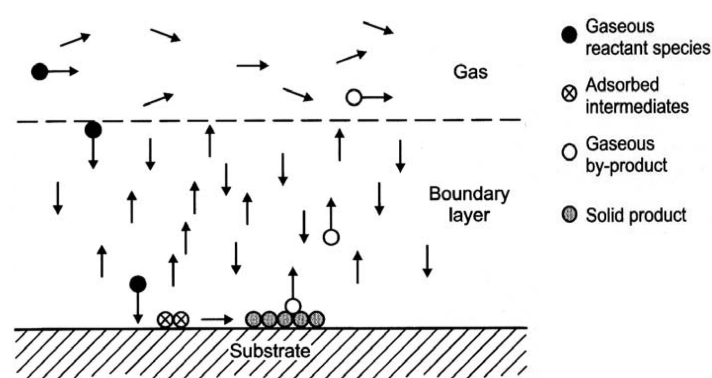

Figure 2.9: Schematic diagram of a CVD process

The most important CVD techniques are:

- Metal Organic Chemical Vapor Deposition (MOCVD)
- Plasma Enhanced Chemical Vapor Deposition (PECVD)
- Atmospheric Pressure Chemical Vapor Deposition (APCVD)
- Low Pressure Chemical Vapor Deposition (LPCVD)
- Electron-Cyclotron Resonance CVD (ECRCVD)

Some of them are discussed bellow.

In plasma enhanced CVD (PECVD), deposition rates can be enhanced if the deposition occurs in glow-discharge plasma. During PECVD thin films are deposited from a vapor (gas state) onto a substrate. Plasma of the reacting gases is created and then several chemical reactions are taking place. In general the plasma is created by an RF frequency or by a DC discharge between two electrodes. Figure 2.10 describes a PECVD process schematically.

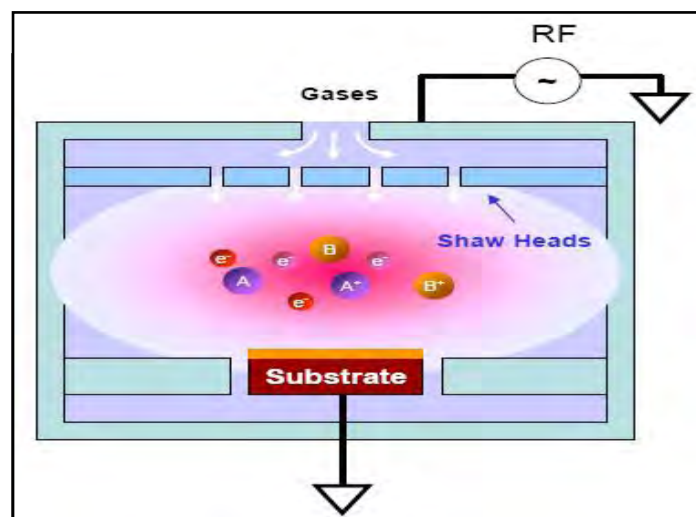

Figure 2.10: The Plasma –Enhanced Chemical Vapor Deposition Process

It enables the deposition of dielectric films such as oxides and nitrides on wafers with small feature sizes and line widths at low temperature and on devices which are not able to withstand the high temperatures of a thermally activated reaction. PECVD is additionally used in amorphous silicon thin film deposition e.g. for photovoltaic panels.

In low pressure CVD (LPCVD), the deposited films are either amorphous, in the case of the inorganic dielectrics, or polycrystalline, in the case of polysilicon or metals. The material properties can depend on the exact process, including the conditions such as temperature, pressure, etc. The LPCVD process produces layers with excellent uniformity of thickness and material characteristics. A schematic diagram of LECVD system is shown in Figure 2.11.

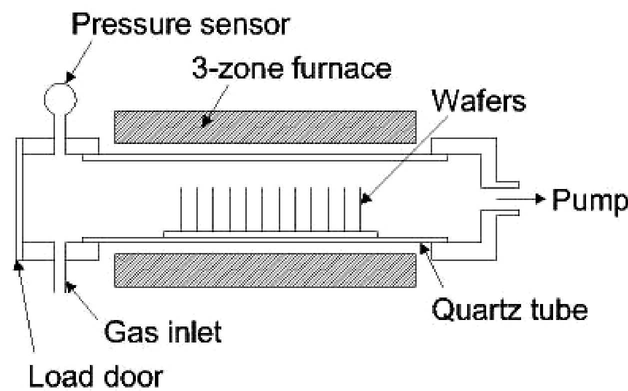

Figure 2.11: A schematic diagram of an LECVD system

2.4.2.2 Spin coating

In this process the material to be deposited is dissolved in liquid form in a solvent. The material can be deposited to the substrate by spraying or spinning. A typical Spin coating process involves depositing a small puddle of a liquid drop onto the center of a substrate and then spinning the substrate at high speed (typically around 3000 rpm). Centripetal acceleration will cause the drop to spread to, and eventually off, the edge of the substrate leaving a thin film of the material on the surface. Final film thickness and other properties will depend on the nature of the liquid drop (viscosity, drying rate, percent solids, surface tension, etc.) and the parameters chosen for the spin process. This is particularly useful for polymer materials, which may be easily dissolved in organic solvents, and it is the common method used to apply photo resist to substrates (in photolithography). Factors such as final rotational speed, acceleration, and fume exhaust contribute to how the properties of coated

film are defined. One of the most important factors in spin coating [31] is repeatability. Subtle variations in the parameters that define the spin process can result in drastic variations in the coated film. In recent years, the casting technology has also been applied to form films of glass materials on substrates. The spin casting process is illustrated in the Figure 2.12.

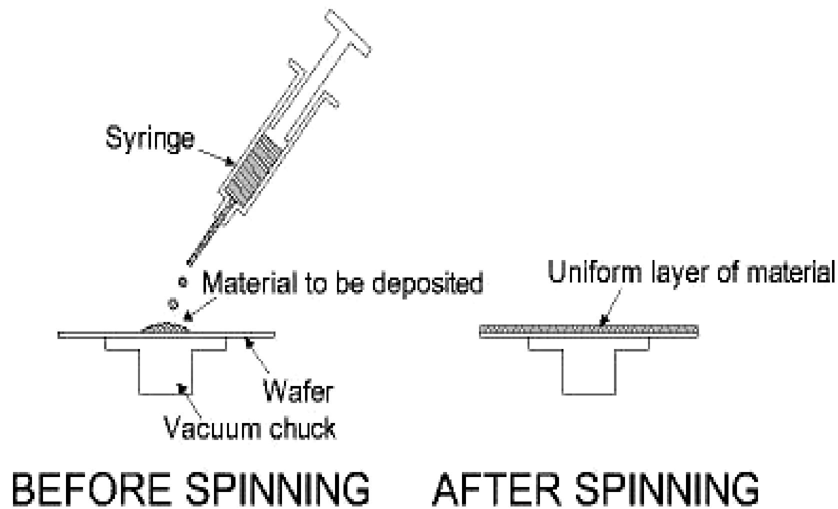

Figure 2.12: The spin coating process

Casting is a simple technology which can be used for a variety of materials (mostly polymers). The control on film thickness depends on exact conditions, but can be sustained within +/-10% in a wide range. If you are planning to use photolithography you will be using casting, which is an integral part of that technology. There are also other interesting materials such as polyimide and spin-on glass which can be applied by casting.

2.4.2.3 Sol-gel technique

Sol-gel method [32] is a wet chemical route for the synthesis of colloidal dispersions of oxides which can be altered to powders, fibers, thin films and monoliths. In general, sol-gel method consists of hydrolysis and condensation reactions. Sol-gel coating is a process of preparation of single or multi-component oxide coating which may be glass, glass ceramic or crystalline ceramic depending on the process. Also, the nanomaterials used in modern

ceramic and device technology require high purity and facilitate to control over composition and structure. Figure 2.13 shows the general scheme of Sol-gel synthesis.

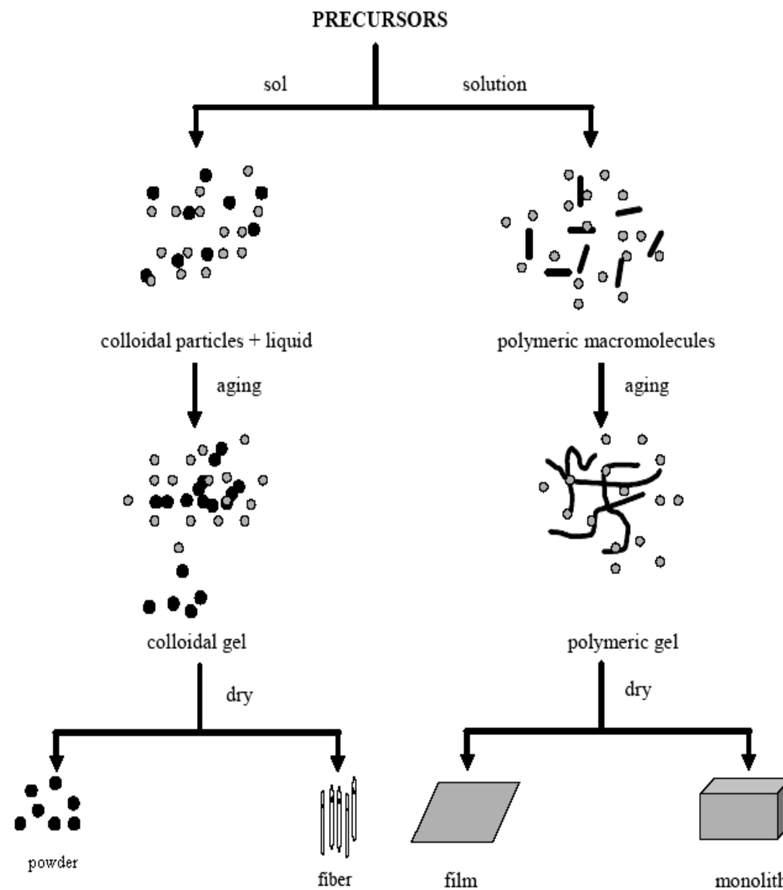

Fig 2.13: Generalized scheme of Sol-gel synthesis

The sol-gel coating is one of the interesting methods because it has many advantages. Examples are as the followings-

- The chemical reactants for sol-gel process can be conveniently purified by distillation and crystallization.
- All starting materials are mixed at the molecular level in the solution so that a high degree of homogeneity of films can be expected.
- Organic or inorganic salts can be added to adjust the microstructure or to improve the structural, optical and electrical properties of oxide films.

- The sol-gel coating is almost exclusively applied for fabrication of transparent layers with a high degree of planarity and surface quality.

2.4.2.4 Chemical bath deposition

The chemical bath deposition (CBD) technique [33] involves the controlled precipitation from solution of a compound on a suitable substrate. Figure 2.14 shows a schematic diagram of CBD process. This deposition takes place in a beaker with DI water where it is heated between temperatures of 85 to 90 ^{o}C. The technique offers many advantages over the more established deposition techniques, such as CVD, MBE and spray pyrolysis. The extent of the heterogeneous reaction on the substrate surface is limited by two major factors, the competing homogeneous reaction in solution and deposition of material on the CBD reactor walls. Chemicals, namely Cadmium Acetate, Ammonium Acetate, Ammonium Hydroxide, and Thiourea are poured individually and its chemical reaction results in the deposition of CdS onto all surfaces in the bath, including the surfaces of the ITO coated glass. Typically, for a 20-minute run, a thickness of 800-1000 Å can be achieved. The substrate is usually annealed before another deposition of other materials takes place.

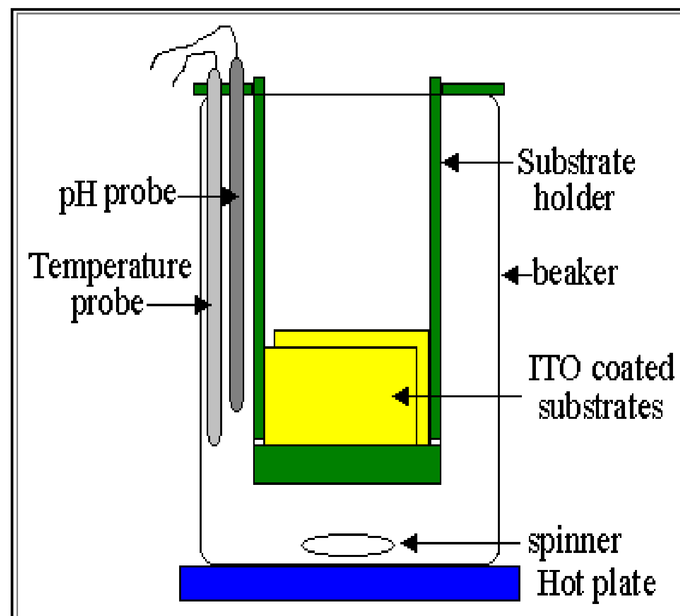

Figure 2.14: Chemical Bath Deposition Process

2.4.2.5 Electroplating

The chemical electroplating is one of the most widely used methods to deposit oxide and sulfides on metals. Black nickel and black chrome is the two well-known selective absorbers prepared on commercial scale by electroplating. In the plating process, parameters like pH of the solution, temperature of the bath, current density and plating time effect the micro structure topology and composition of the coatings. By varying the current while plating one can obtain a stack of numerous finely divided layers with a continuous gradient of composition resulting in a continuous gradient of refractive index.

2.4.2.6 Spray pyrolysis technique

SPT [34] is a process in which a thin film is deposited by spraying of an ionic solution, usually aqueous, containing soluble salts of the constituent atoms of the desired compound on a heated surface, where the constituents react to form a chemical compound. Hydrolysis and pyrolysis are the main chemical reactions involved in this process. The chemical reactions are selected such that the products other than the desired compound are volatile at the temperature of deposition. It is an excellent, low-cost, simple and rapid method for the deposition of thin films of semiconductor alloys and complex compounds and is suitable for industrial applications. It has been used for about 35 years for the manufacture of conductive glass. This process is particularly useful for the deposition of transparent conducting oxides on glass and is sensitive to variables particularly temperature, and the measurement at the surface is uncertain. Not only the physical and electronic properties of the film vary with temperature, but the deposition efficiency decreases with increased temperature, stoichiometry is also affected, particularly for alloys. In spite of these difficulties, spray pyrolysis is an excellent method for the deposition of large-area thin films.

Viguie and Spitz classified chemical SP process according to the type of reaction. In process

- The droplet resides on the surface as the solvent evaporates, leaving behind a solid that may further react in the dry state.
- The solvent evaporates before the droplet reaches the surface and the dry solid impinges on the surface, where decomposition occurs.
- The solvent vaporizes and the vapor diffuses to the substrate, there to undergo a heterogeneous reaction. (They identify this process as true chemical vapor deposition.).
- The enter reaction takes place in the vapor state.

The apparatus needed to carry out the chemical spray process consists of an optimizer the spray solution and a substrate heater. Figure 2.15 shows a schematic diagram of an SPD set up.

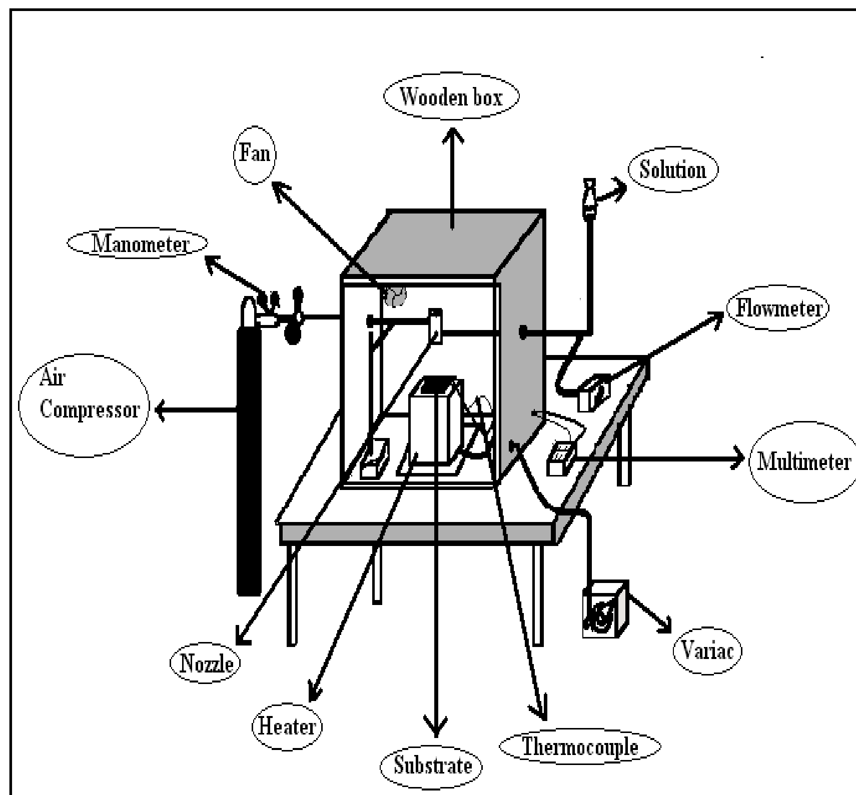

Figure 2.15: Schematic diagram of an SPD set up

2.4.2.6 Electrodeposition

The occurrence of chemical changes owing to the passage of electric current through an electrolyte is termed electrolysis and the deposition of any substance on an electrode as a consequence of electrolysis is called electrodeposition. The phenomenon of electrolysis is governed by the following two laws, first enunciated by Faraday in 1833: (i) the magnitude of chemical change occurring is proportional to the quantity of electricity passed and (ii) the masses of different species deposited at or dissolved from electrodes by the same quantity of electricity are in direct proportion to equivalent weights [35]. The two laws can be combined and expressed mathematically as

$$W = IEt/F$$

Where W is the mass (in g) of the substance deposited, I is the current (in A), E is the chemical equivalent weight (in g), and t is the reaction time (in s). F is a constant called the Faraday, equal to 96500 C and is the amount of charge required to deposit one equivalent of any ion from a solution.

In a laboratory, a low cost electrodeposition method can be easily developed and used for the preparation of cadmium sulfide thin film. This method is not only simple but also has optimum material utilization rate and low energy consumption. Since the materials are dissolved in a solution and the deposition process is carried out at a relatively low temperature, potential safety hazard during the deposition in minimized. In addition, the deposition system can be easily scaled up for large area film deposition.

References

[1] Bunn, C.W., “A Comparative Review of ZnO Materials and Devices”, Proc. Phys. Soc. London. 47, 835, (1935).

[2] Allenic, A. L., “Structural, Electrical and Optical Properties of P-type Zinc Oxide Epitaxial Films”, Ph.D. thesis, University of Michigan: ProQuest, (2008).

[3] Özgür, Ü. , Alivov, Y. I., Liu, C., Teke, A., Reshchikov, M. A., Doğan, S., Avrutin, V., Cho, S.J., Morkoç, H., "A comprehensive review of ZnO materials and devices", J. Appl. Phys., **98** (4), 041301-1-041301-101, (2005).

[4] Rossler , U., Bornstein, L, “New Series, Group III.17B, 22, 41B”, Springer: Heidelberg, (1999).

[5] Klingshirn, C. F., Waag, A., Hoffmann, A., Geurts, J., “Zinc Oxide: From Fundamental Properties Towards Novel Applications”, Springer Series in Materials Science. 120, Springer Science & Business Media, (2010).

[6] Abrahams, S. C., Beinstein, J.L., “Remeasurement of the Structure of Hexagonal ZnO”, Acta Cryst. B25, 1233-1236, (1969).

[7] Pauling, L., “The Nature of the Chemical Bond”, Cornell University Press, Ithaca, New York, (1960).

[8] Meyer, B. K., Alves, H., Hofmann, D. M., Kriegseis, W., Forster, D., Bertram, F., Christen, J., Hoffmann, A., Straßburg, M., Dworzak, M., Haboeck, U., Rodina, A. V., “Bound exciton and donor-acceptor pair recombinations in ZnO ”, Phys. Stat. Sol. (b) 241, 231-260, (2004).

[9] Yoshikawa, H., Adachi, S. “Optical Constants of ZnO”, Jpn. J. Appl. Phys. 36 (1997) 6237-6243.

[10] Ashkenov, N., Mbenkum, B. M., Bundesmann, C., Riede, V., Lorenz, M., Spemann, D., Kaidashev, E. M., Kasic, A., Schubert, M., Grundmann, M., Wanger, G., Neumann, H., Darakchieva, V., Arwin, H., Monemar, B., “Infrared dielectric functions and phonon modes of high-quality ZnO films”, J. Appl. Phys., 93, 126-133, (2003).

[11] Sun, X. W., Kwok, H. S., “Optical properties of epitaxially grown zinc oxide films on sapphire by pulsed laser deposition”, J. Appl. Phys., 86, 408-411, (1999).

[12] Look, D. C., Clafin, B., Alivov, Y. I., Park, S. J., “The future of ZnO light emitters”, Phys. Stat. Sol. a, 201, 2203-2212, (2004).

[13] Pearton, S. J., Norton, D. P., Ip, K., Heo, Y.W., Steiner, T., “Recent progress in processing and properties of ZnO”, Prog. Mater. Sci. 50(3), 293-340, (2005).

[14] Oganov, A. R., Chen, J., Gatti, C., Ma, Y. M., Yu, T., Liu, Z., Glass, C. W., Ma, Y. Z., Kurakevych, O. O., Solozhenko, V. L., "Ionic high-pressure form of elemental boron", Nature., 457, 863-867, (2009).

[15] Holleman, A. F., Wiberg, E., Wiberg, N. "Bor". Lehrbuch der Anorganischen Chemie (German) (91–100 ed.). Walter de Gruyter., 814-864, (1985).

[16] Liao, L., Li, J. C., Wang, D. F., Liu, C., Liu, C. S., Fu, Q., Fan, L. X., “Field emission property improvement of ZnO nanowires coated with amorphous carbon and carbon nitride films”, Nanotech., 16(9), 985-989, (2005).

[17] Xia, Y., Yang, P., Sun, Y., Wu, Y., Mayers, B., Gates, B., Yin, Y., Kim, F., Yan, H., “One-Dimensional Nanostructures: Synthesis, Characterization, and Applications”, Adv. Mater., 15(5), 353-389, (2003).

[18] Wang, Z. L., “Zinc oxide nanostructures: growth, properties and applications”, J. Phys. Cond. Matter., 16, R829-R858, (2004).

[19] Sirbuly, D. J., Law, M., Yan, H. Q., Yang, P. D., “Semiconductor Nanowires for Subwavelength Photonics Integration”, J. Phys. Chem. B, 109(32), 15190-15213, (2005).

[20] Look, D. C., “Recent advances in ZnO materials and devices”, Mater. Sci. Eng. B, 80, 383-387, (2001).

[21] Gardeniers, J. G. E., Rittersma, Z. M., Burger, G. J., “Preferred orientation and piezoelectricity in sputtered ZnO films”, J. Appl. Phys., 83, 7844-7954, (1998).

[22] Norton, D. P., Pearton, S. J., Hebard, A. F., Theodoropoulou, N., Boatner, L. A., Wilson, R. G., “Ferromagnetism in Mn-implanted ZnO:Sn single crystals”, Appl. Phys. Lett., 82(2), 239-241, (2003).

[23] Nause, J., “Fluorescent substrate offers route to phosphor-free LEDs”, Comp. Semicond. 11, 29, (2005).

[24] Hartnagel, H., Dawar, A. L., Jain, A. K., Jagadish, C., "Semiconducting transparent thin films", Institute of Physics Publishing, Bristol and Philadelphia, (1995).

[25] Look, D. C., Reynolds, D. C., Hemsky, J. W., Jones, R. L., Sizelove, J. R., "Production and annealing of electron irradiation damage in ZnO", Appl. Phys. Lett., 75(6), 811-813, (1999).

[26] Chopra, K. L., Das, S. R., "Thin film solar cells", Plenum Press, New York (1983).

[27] Behrisch, R, "Sputtering by Particle bombardment", Springer: Berlin, (ed.) (1981).

[28] Cho, A. Y., Arthur, J. R., "Molecular beam epitaxy", Prog. Sol. State. Chem., 10, 157-192, (1975).

[29] Mahan, J. E., "Physical Vapor Deposition of Thin Films", John Wiley & Sons: New York, (2000).

[30] Dobkin, D., Zuraw, M. K., "Principles of Chemical Vapor Deposition", Springer Science & Business Media, (2003).

[31] Scriven, L. E., "Physics and applications of dip coating and spin coating", Mater. Res. Soc. Symp. Proc., 121, 717-729, (1988).

[32] Hench, L. L., West, J.K., "The Sol-Gel Process", Chem. Rev., 90(1), 33-72, (1990).

[33] Lincot, D., Hodes, G., "Chemical Solution Deposition of Semiconducting and Non-metallic Films", Proc. Int. Symp. Electrochem. Soc., 2003-2032, (2006).

[34] Chamberlin, R. R., Skarman, J. S., "Chemical spray deposition process for inorganic films", J. Electrochem. Soc., 113(1), 86-89, (1966).

[35] Dini, J. W., "Electrodeposition: The Materials Science of Coatings and Substrates", Noyes Publications: New Jersey, (1993).

CHAPTER 3

THEORIES RELATED TO CHARACTERIZATION TECHNIQUES

CHAPTER 3
THEORIES RELATED TO CHARACTERIZATION TECHNIQUES

Generally, the structural, optical and electrical properties of thin films are elucidated using different techniques. In this section, the basic principles of some of the characterization methods are discussed briefly. These techniques include XRD for structural characterization, SEM for surface morphology, EDX spectroscopy for the film compositional study, and UV-vis spectroscopy for the optical characterization.

3.1 Structural Characterization

The term structure encloses a variety of concepts, which describe on various scales, the arrangement of the building blocks of materials. On an atomic scale, one deals with the crystal structure, which is defined by the crystallographic data of the unit cell. These data contain the shape and dimensions of the unit cell and the atomic position within its Bravais structure. They are obtained by diffraction experiments. On a coaster scale, one deals with the microscopic observations of the microstructure, which characterizes the size, shapes and mutual arrangements of individual crystal grains. It also includes the morphology of the surface of the materials. Microstructure and surface morphology observation of coatings, which are too 'thick for direct transmission also depends heavily on the high resolving power of electron microscopy. Suitable technique is surface replication and SEM [1-4]. Frequently one has to determine whether a given deposit is a single crystal or polycrystalline either with a random distribution of orientation with respect to the coating plane. For a single crystal coating, it is important to know its orientation relationship with respect to the substrate [5].

3.1.1 X-ray diffraction

XRD is one of the oldest and effective tools for understanding structure of crystalline materials. It provides extensive information about the crystal structure. X-rays are the electromagnetic waves with the wavelength between 1-100Å. The wavelength of an X-ray is thus of the same order of magnitude as the lattice constant of crystals. When X-rays are incident on a crystal surface, they are reflected from it.

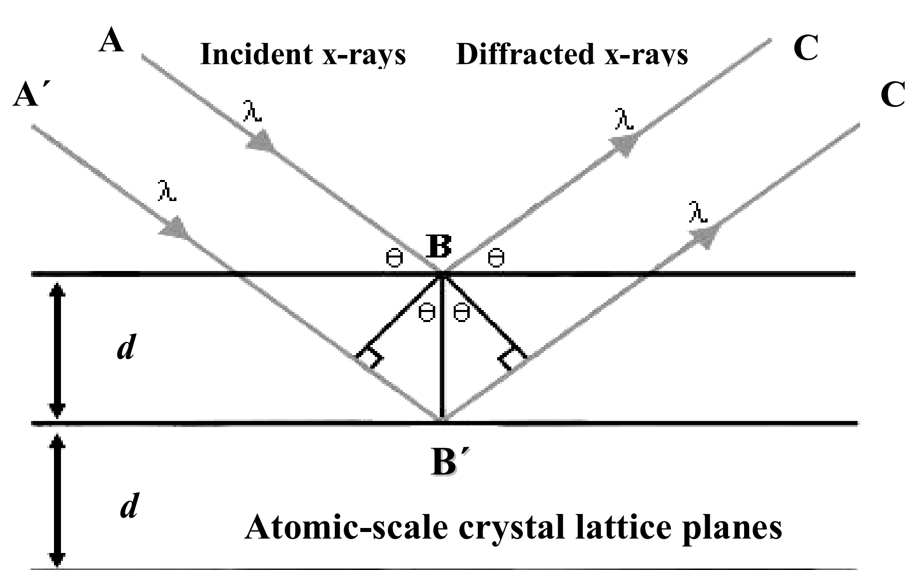

Figure 3.1: Bragg‟s law of X-ray diffraction

The reflection obeys the following Bragg‟s law,

$$2d\sin\theta = n\lambda \qquad (3.1)$$

where d is the distance between crystal planes; θ is the X-ray angle of incidence; λ is the wavelength of the X-rays and n is a positive integer. Bragg‟s law also suggests that the diffraction is only possible when a boundary condition is satisfied. The boundary condition is, $\lambda < 2d$.

XRD is the most specific technique for studying the crystal structure of solids. Generally, it does not require any elaborate sample preparation and is essentially nondestructive to samples [6, 7]. XRD is a suitable tool to determine the crystal structure of any unknown materials, whether the sample is a single crystal or polycrystals [6], either with a random

distribution of orientations or with a preferred orientation with respect to the film plane. Thicknesses of surface thin films are about 1000Å and those can be investigated using XRD [8, 9]. Thicker films can be characterized by reflection high-energy electron diffraction (RHEED). Analysis of the diffraction patterns obtained by these techniques and comparison with standard ASTM data can reveal the existence of different crystallographic phases in the film, their relative abundance, the lattice parameters, and any preferred orientations.

3.1.1.1 Lattice constants

The interplanar spacing for the hexagonal system is given as

$$\frac{1}{d_{hkl}} = \left[\frac{4}{3}\left(\frac{h^2++hk+k^2}{a^2}\right) + \frac{l^2}{c^2}\right]^{\frac{1}{2}} \qquad (3.2)$$

where, h, k and l are the indices of the crystal planes; d_{hkl} is the interplanar spacing and it is related to the diffraction angle θ as

$$\frac{1}{d_{hkl}} = \frac{2\sin\theta_{hkl}}{\lambda} \qquad (3.3)$$

The wavelength (λ) of X-ray is used 1.54178 Å for CuK_α line.

To determine the exact lattice parameter for each sample, Nelson-Riley [10] method was used. The Nelson-Riley function F (θ) is given by,

$$F(\theta) = \frac{1}{2}\left[\left(\frac{\cos^2\theta}{\sin\theta}\right) + \left(\frac{\cos^2\theta}{\theta}\right)\right] \qquad (3.4)$$

The values of lattice constant 'a' of all the peaks for a sample are plotted against F(θ). Then using a least square fit method exact lattice parameter ' a ' is determined. The point where the least square fit straight line cut the y-axis (i.e. at F(θ) = 0) is the actual lattice parameter of the sample.

3.1.1.2 Crystallite size

The crystallite size (D) of the deposited the thin films is estimated using Scherrer formula [11],

$$D = \frac{k\lambda}{\beta \cos \theta} \qquad (3.5)$$

Here k is taken as 0.94, λ the wavelength of X-ray used and β the full width at half maximum (FWHM) of the highest peak in XRD pattern.

3.1.1.3 Microstrain

The origin of the strain in the thin film is related to the lattice misfit, which in turn depends upon the deposition conditions. The strain developed in the film is known as microstrain (ε) and it is calculated from the relation as follows [12],

$$\varepsilon = \frac{(\beta \cos \theta)}{4} \qquad (3.6)$$

3.1.1.4 Dislocation density

Dislocation is an imperfection in a crystal associated with the misregistry of the lattice in one part of the crystal with that in another part. Unlike vacancies and interstitial atoms, dislocations are not equilibrium imperfections, i.e. thermodynamic considerations are insufficient to account for their existence in the observed densities. In fact, the growth mechanism involving dislocation is a matter of importance. In the present study, the dislocation density is estimated from Williamson and Smallman method using the relation [12, 13]

$$\delta = \frac{15\varepsilon}{aD} \qquad (3.7)$$

3.2 Surface Morphology

3.2.1 Working principle of an electron microscope

Electron Microscopes function exactly as their optical counterparts except that they use a focused beam of electrons instead of light to "image" the specimen and gain information as to its structure and composition. The basic steps involved in all electron microscopes are shown in Figure 3.2. A stream of electrons is formed (by the Electron Source) and accelerated toward the specimen using a positive electrical potential. This stream is confined and focused using metal apertures and magnetic lenses into a thin, focused, monochromatic beam. This beam is focused onto the sample using a magnetic lens. Interactions occur inside the irradiated sample, affecting the electron beam. These interactions and effects are detected and transformed into an image. The above steps are carried out in all electron microscopes regardless of type.

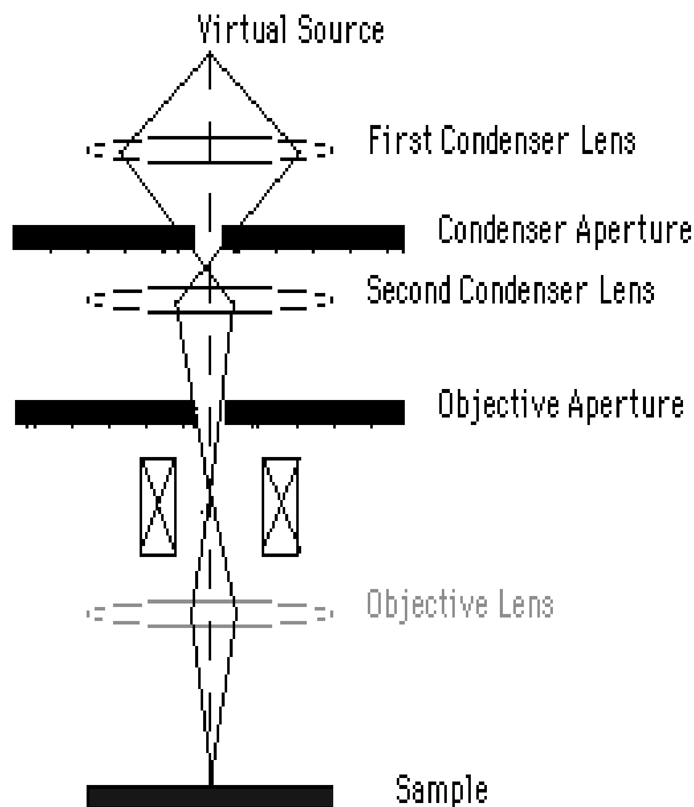

Figure 3.2: Schematic diagram of an electron microscope

3.2.2 Scanning electron microscopy

SEM is a type of microscope that form images the sample surface by scanning it with a high-energy beam of electrons in a raster scan pattern. It is a powerful microscope that uses electrons rather than light to form an image of objects such as fractured metal components, foreign particles and residues, polymers, thin films electronic components, biological samples, and countless others. The shorter wavelength of electrons permits image magnifications of up to 100,000X, as compared to about 2,000X for conventional light microscopy. An SEM also provides a greater depth of field than a light microscope, allowing complex, three-dimensional objects to remain sharp and in focus.

In a typical SEM, an electron beam is thermoionically emitted from an electron gun fitted with a tungsten filament cathode. Other types of electron emitters include lanthanum hexaboride cathodes, which can be used in a standard tungsten filament SEM. if the vacuum system is upgraded. Field emission guns (FEG) of the cold-cathode type using tungsten single crystal emitters or the thermally-assisted Schottky type, using emitters of zirconium oxide can also be used. The electron beam, which typically has an energy ranging from a few hundred eV to 40 keV, is focused by one or two condenser lenses to a spot about 0.4 nm to 5 nm in diameter. The beam passes through pairs of scanning coils or pairs of deflector plates in the electron column, typically in the final lens, which deflect the beam in the x and y axes so that it scans in a raster fashion over a rectangular area of the sample surface. The size of the interaction volume depends on the electron's landing energy, the atomic number of the specimen and the specimen's density. The energy exchange between the electron beam and the sample results in the reflection of high-energy electrons by elastic scattering, emission of secondary electrons by inelastic scattering and the emission of electromagnetic radiation, each of which can be detected by specialized detectors. The beam current absorbed by the specimen can also be detected and used to create images of the

distribution of specimen current. Electronic amplifiers of various types are used to amplify the signals which are displayed as variations in brightness on a cathode ray tube. The raster scanning of the CRT display is synchronized with that of the beam on the specimen in the microscope, and the resulting image is therefore a distribution map of the intensity of the signal being emitted from the scanned area of the specimen. The image may be captured by photography from a high resolution cathode ray tube, but in modern machines is digitally captured and displayed on a computer monitor and saved to a computer's hard disc.

Figure 3.3: A scanning electron microscope with EDS set up

In this work, a thermal field emission gun scanning electron microscope (FEG-SEM) of model JEOL JSM-7600F is used (Figure 3.3). It has an ultrahigh resolution for fine surface morphology of nanostructures (secondary electron image resolution 1.0 nm at 15 kV). It contains built-in r-filter enabling user selectable mixture of secondary electron (SE) and backscattered electron (BSE) images. It has Gentle Beam (GB) mode for accelerating voltage in kV, top-surface imaging, reduced beam damage and charge suppression allows examination of charging specimens without additional coating. New low-angle backscattered electrons detector allows imaging of specimens at extremely low accelerating voltage (kV) with high spatial resolution. Scanning transmission electron microscopy detector allows both

bright-field and dark-field imaging of thin, electron transparent samples with sub 0.8 nm resolution. For EDS this field emission SEM (FESEM) set up is connected to a Aztec Synergy system (Oxford AZtec energy/AZtec HKL) with X-MAX50 silicon drift detector which provides high counts rate and allows Nanoanalysis, Mapping, Crystal Orientation.

3.3 Elemental Analysis

Energy Dispersive X-ray spectroscopy (EDS) is the elemental analysis of the thin film by studying the energy dispersive table i.e. studying the net counts and net weight percentage we can analysis the elemental percentage. Studying the EDX table we also get the information about the elements in the thin film.

3.3.1 Energy dispersive x-ray spectroscopy

EDS is an analytical technique used for the chemical characterization of a sample. It is one of the variants of X-ray fluorescence (XRF) analysis. As a type of spectroscopy, it relies on the investigation of a sample through interactions between electromagnetic radiation and matter, analyzing X-rays emitted by the matter in response to being hit with charged particles. Its characterization capabilities are due in large part to the fundamental principle that each element has a unique atomic structure allowing x-rays that are characteristic of an element's atomic structure to be identified uniquely from each other.

To stimulate the emission of characteristic X-rays from a specimen, a high energy beam of charged particles such as electrons or protons (see PIXE), or a beam of X-rays, is focused into the sample being studied. At rest, an atom within the sample contains ground state (or unexcited) electrons in discrete energy levels or electron shells bound to the nucleus. The incident beam may excite an electron in an inner shell, ejecting it from the shell while creating an electron hole where the electron was. An electron from an outer, higher-energy

shell then fills the hole, and the difference in energy between the higher-energy shell and the lower energy shell may be released in the form of an X-ray. The number and energy of the X-rays emitted from a specimen can be measured by an EDS. As the energy of the X-rays are characteristic of the difference in energy between the two shells, and of the atomic structure of the element from which they were emitted, this allows the elemental composition of the specimen to be measured.

3.4 Optical Characterization

3.4.1 Beer-Lambert law

The Beer-Lambert law (or Beer's law) [14] is the linear relationship between absorbance and concentration of an absorbing species. The general Beer-Lambert law is usually written as:

$$A = abc \quad (3.8)$$

where A is the measured absorbance, "a" is a wavelength-dependent absorptivity coefficient, b is the path length, and c is the analyzed concentration. When working in concentration units of molarity, the Beer-Lambert law is written as:

$$A = \varepsilon bc \quad (3.9)$$

where „ε" is the wavelength-dependent molar absorptivity coefficient with units of M^{-1} cm^{-1}. Experimental measurements are usually made in terms of transmittance (T), which is defined as:

$$T = I / I_o \quad (3.10)$$

Where, I is the light intensity after it passes through the sample and I_o is the initial light intensity. The relation between A and T is:

$$A = -\log T = -\log (I / I_o) = \log (I_0/I) \quad (3.11)$$

Modern absorption instruments can usually display the data as either transmittance in % or absorbance.

The Beer-Lambert law can be derived from an approximation for the absorption coefficient for a molecule by approximating the molecule by an opaque disk whose cross-sectional area, σ, represents the effective area seen by a photon of frequency υ . If the frequency of the light is far from resonance, the area is approximately 0, and if υ is close to resonance the area is a maximum. Taking an infinitesimal slab, dz, of sample (Figure 3.4):

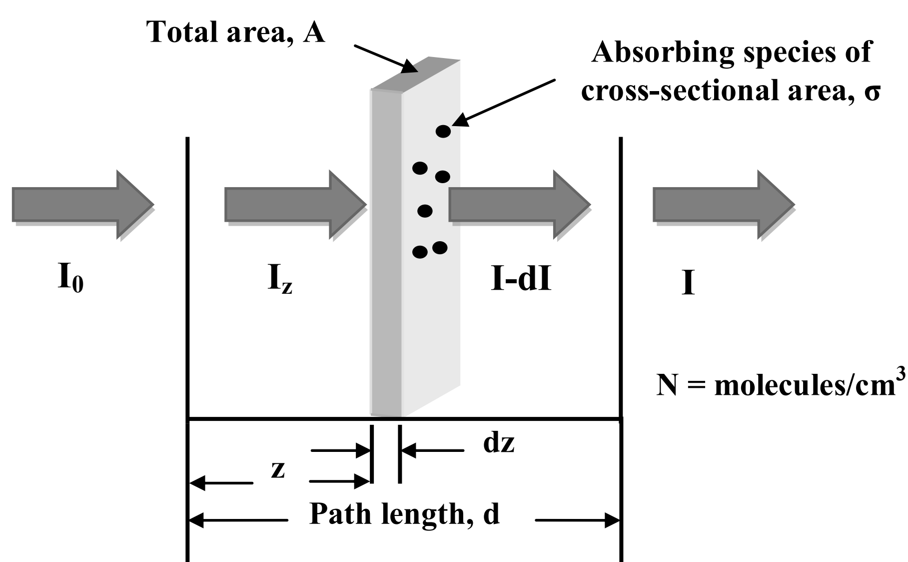

Figure 3.4: Absorption of light by a sample

I_o is the intensity entering the sample at z=0, I_z is the intensity entering the infinitesimal slab at z, dI is the intensity absorbed in the slab, and I is the intensity of light leaving the sample. Then, the total opaque area on the slab due to the absorbers is ζN A dz. Then, the fraction of photons absorbed will be ζN A dz / A. So,

$$\frac{dI}{I_Z} = -\sigma N dz \qquad (3.12)$$

Integrating this equation from z = 0 to z = b gives:

$\ln(I) - \ln(I_o) = - \zeta\ N\ b$

or, $- \ln(I / I_o) = -\zeta\ N\ b$

Since N (molecules/cm^3) (1 mole / 6.023x10^{23} molecules) 1000 cm^3 / liter = c (moles/liter) and 2.303*log(x) = ln(x)

Then, $- \log (I / I_o) = \zeta(6.023\times10^{20} / 2.303)\ cb$

Or, $A = \varepsilon\ bc = - \log (I / I_o)$ (3.13)

Where, $\varepsilon = \sigma\ (6.023\times10^{20} / 2.303) = \sigma(2.61\times10^{20})$, and ε is called the molar absorptivity. Thus the intensity of the transmitted light can be expressed as $I=I_0\ e^{-\alpha d}$ where d is the path length through the sample and α is the absorption coefficient. This equation can be written as,

$$\alpha = \frac{2.303\ A}{d} \quad (3.14)$$

3.4.2 Electronic transitions

The absorption of UV or visible radiation corresponds to the excitation of outer electrons. There are three types of electronic transition which can be considered;

1. Transitions involving π, ζ, and *n* electrons
2. Transitions involving charge-transfer electrons
3. Transitions involving *d* and *f* electrons (not covered in this Unit)

When an atom or molecule absorbs energy, electrons are promoted from their ground state to an excited state. In a molecule, the atoms can rotate and vibrate with respect to each other. These vibrations and rotations also have discrete energy levels, which can be considered as being packed on top of each electronic level (Figure 3.5).

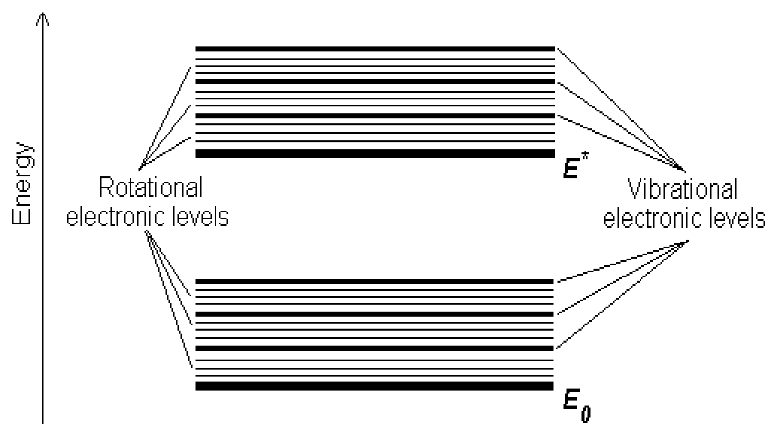

Figure 3.5: Vibrational and rotational energy levels

Absorbing species containing π, σ, and n electrons

Absorption of ultraviolet and visible radiation in organic molecules is restricted to certain functional groups (chromophores) that contain valence electrons of low excitation energy. The spectrum of a molecule containing these chromophores is complex. This is because the superposition of rotational and vibrational transitions on the electronic transitions gives a combination of overlapping lines. This appears as a continuous absorption band. Possible electronic transitions of π, ζ, and n electrons are discussed below (Figure 3.6).

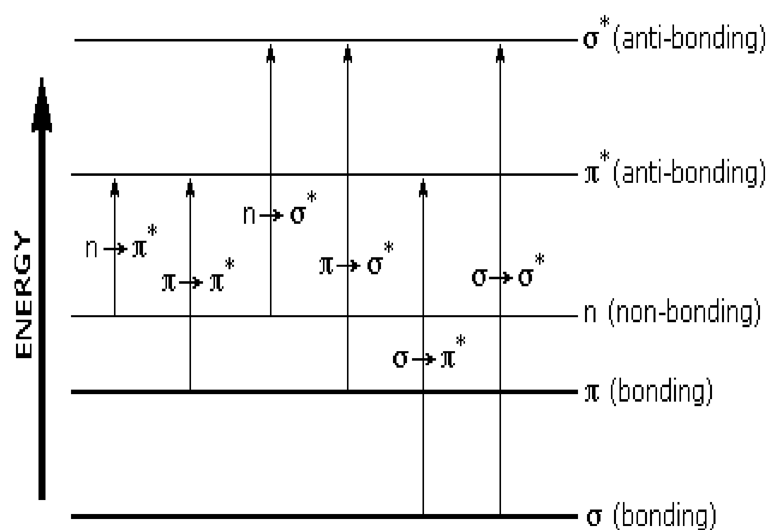

Figure 3.6: Possible electronic transitions

$\sigma \rightarrow \sigma^*$ Transitions

An electron in a bonding ζ orbital is excited to the corresponding antibonding orbital. The energy required is large. For example, methane (which has only C-H bonds, and can only undergo $\zeta \rightarrow \zeta^*$ transitions) shows an absorbance maximum at 125 nm. Absorption maxima due to $\zeta \rightarrow \zeta^*$ transitions are not seen in typical UV-Vis. spectra (200 - 700 nm).

$n \rightarrow \sigma^*$ Transitions

Saturated compounds containing atoms with lone pairs (non-bonding electrons) are capable of $n \rightarrow \zeta^*$ transitions. These transitions usually need less energy than $\zeta \rightarrow \zeta^*$ transitions. They can be initiated by light whose wavelength is in the range 150 - 250 nm. The number of organic functional groups with $n \rightarrow \zeta^*$ peaks in the UV region is small.

$n \rightarrow \sigma^*$ and $\pi \rightarrow \pi^*$ Transitions

Most absorption spectroscopy of organic compounds is based on transitions of *n* or π electrons to the π^* excited state. This is because the absorption peaks for these transitions fall in an experimentally convenient region of the spectrum (200 - 700 nm). These transitions need an unsaturated group in the molecule to provide the π electrons. Molar absorbtivities from $n \rightarrow \pi^*$ transitions are relatively low, and range from 10 to100 L mol^{-1} cm^{-1}. $\pi \rightarrow \pi^*$ transitions normally give molar absorbtivities between 1000 and 10,000 L mol^{-1} cm^{-1} . The solvent in which the absorbing species is dissolved also has an effect on the spectrum of the species. Peaks resulting from $n \rightarrow \pi^*$ transitions are shifted to shorter wavelengths (blue shift) with increasing solvent polarity. This arises from increase of the lone pair, which lowers the energy of the n orbital. Often (but not always), the reverse (i.e. red shift) is seen for $\pi \rightarrow \pi^*$ transitions. This is caused by attractive polarization forces between the solvent and the

absorber, which lower the energy levels of both the excited and unexcited states. This effect is greater for the excited state, and so the energy difference between the excited and unexcited states is slightly reduced - resulting in a small red shift. This effect also influences $n \rightarrow \pi^*$ transitions but is overshadowed by the blue shift resulting from the increase of lone pairs.

3.4.3 Direct and indirect optical transitions

In solid state physics and related applied fields, the band gap, also called an energy gap or stop band, is a region where a particle or quasiparticle is forbidden from propagating. For insulators and semiconductors, the band gap generally refers to the energy difference between the top of the valence band and the bottom of the conduction band (Figure 3.7). Fundamental absorption refers to the annihilation or absorption of photons by the excitation of an electron from the valence band up into the conduction band, leaving a hole in the valence band. Both energy and momentum must be conserved in such a transition.

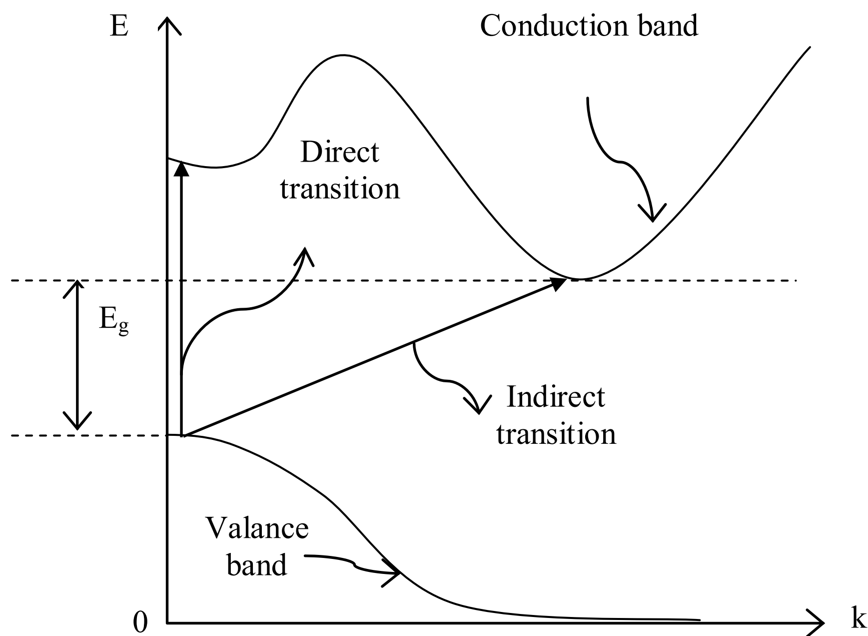

Figure 3.7: Direct and indirect transitions between valance and conduction bands with extrema at different values of momentum (k)

In the case of an indirect-band gap semiconductor, the minimum energy in the conduction band and the maximum energy in the valence band occur at different values of crystal momentum. Photon energies much larger than the forbidden gap are required to give direct transitions of electrons from the valence to the conduction band. However, transitions can occur at lower energies by a two-step process involving not only photons and electrons but also a third particle, a phonon.

To estimate the nature of absorption a random phase model is used where the k momentum selection rate is completely relaxed. The integrated density of states N (E) has been used and defined by

$$N(E) = \int_{-\infty}^{+\infty} g(E)dE \qquad (3.15)$$

The density of states per unit energy interval may be represented by

$$g(E) = \frac{1}{V}\sum \delta(E - E_n) \qquad (3.16)$$

Where, V is the volume, E is the energy at which g(E) is to be evaluated and E_n is the energy of the nth state.

If $g_v \propto E^p$ and $g_c \propto (E\text{-}E_{opt})$, where energies are measured from the valance band mobility edge in the conduction band (mobility gap), and substituting these values into an expression for the random phase approximation, the relationship obtained

$\nu^2 I_2(\nu) \propto (h\nu\text{-}E_0)^{p+q+1}$, where $I_2(\nu)$ is the imaginary part of the complex permittivity. If the density of states of both band edges is parabolic, then the photon energy dependence of the absorption becomes,

$\alpha h\nu \propto \nu^2 I_2(\nu) \propto (h\nu\text{-}E_{opt})^2$

So, for higher photon energies the simplified general equation which is known as Tauc relation is,

$$\alpha h\nu = B(h\nu - E_{opt})^n \qquad (3.17)$$

where $h\nu$ is the energy of absorbed light, n is the parameter connected with distribution of the density of states and B, a constant or Tauc parameter and here n = 1/2 for direct and n = 2 for indirect transitions [15].

The above equation can be written as

$$\frac{d\,[\ln(\alpha h\nu)]}{d[h\nu]} = \frac{n}{h\nu - E_{opt}} \qquad (3.18)$$

When finding the n, type of transition can be obtained from the absorption spectrum. A discontinuity in the d[ln(αhν)]/d(hν) versus hν plot at the band gap energy (E_{opt} or E_g), i.e. at hν = E_g can be observed. The discontinuity at a particular energy value gives the band gap E_g. Thus from the straight-line plots of $(\alpha h\nu)^2$ versus hν and $(\alpha h\nu)^{1/2}$ versus hν the direct and indirect energy gaps of thin films can be determined.

3.4.4 Refractive index and extinction coefficient

One of the most important optical constants of a material is its refractive index, which in general depends on the wavelength of the electromagnetic wave, through a relationship called dispersion. In materials where an electromagnetic wave can lose its energy during its propagation, the refractive index becomes complex. Refraction of light at the interface between two media of different refractive indices n_1 and n_2 is shown in Figure 3.8.

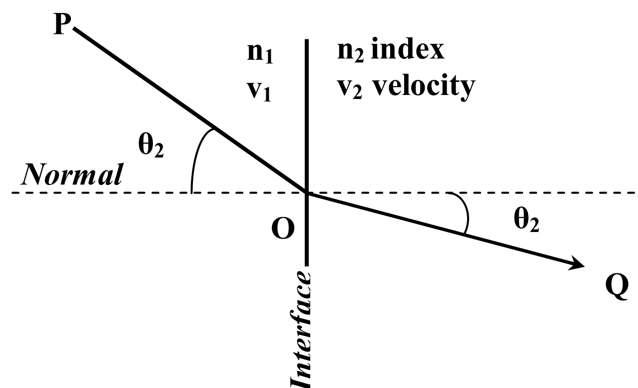

Figure 3.8: Refraction of light at the interface between two media of different refractive indices

The real part is usually the refractive index (n) and the imaginary part is called the extinction coefficient (k). In this section, n and k will be presented in detail along with some common dispersion relations. n of an optical or dielectric medium, is the ratio of the velocity of light (c) in vacuum to its velocity v in the medium; n=c/v [16]. Using this and Maxwell"s equations, one obtains the well known Maxwell"s formula for the refractive index of substance as $n = \sqrt{\varepsilon\mu_r}$ where ε is the static dielectric constant or relative permittivity and μ_r the relative permeability. As $\mu_r = 1$ for nonmagnetic substances, one gets, $n = \sqrt{\varepsilon}$, which is very useful in relating the dielectric properties to optical properties of materials at any particular frequency of interest. As ε depends on the wavelength of light, n also depends on the wavelength of light, and this dependence is called dispersion. In addition to dispersion, an

electromagnetic wave propagating through a medium experiences attenuation, which means it loses its energy, due to various loss mechanisms such as the generation of phonons (lattice waves), photo generation, free carrier absorption, scattering, etc. In such materials, the refractive index becomes a complex function of the frequency of the light wave. The complex refractive index, denoted by n*, with real part n, and imaginary part k, called the extinction coefficient, is related to the complex relative permittivity (ε) by:

$$n^* = n - jk = \sqrt{\varepsilon} = \sqrt{\varepsilon_r - j\varepsilon_i} \qquad (3.19)$$

Where ε_r and ε_i are, respectively, the real and imaginary parts of ε. Equation (3.19) gives

$$n^2 - k^2 = \varepsilon_r \text{ and } 2nk = \varepsilon_i \qquad (3.20)$$

In explicit terms, n and k can be obtained as:

$$n = (1/2^{½}) [(\varepsilon_r^2 + \varepsilon_i^2)^{1/2} + \varepsilon_r]^{1/2} \qquad (3.21)$$

$$k = (1/2^{1/2}) [(\varepsilon_r^2 + \varepsilon_i^2)^{1/2} - \varepsilon_r]^{1/2} \qquad (3.22)$$

The optical constants n and k can be determined by measuring the reflectance from the surface of a material as a function of polarization and the angle of incidence. For normal incidence, the reflection coefficient, r, is obtained as

$$r = \frac{1-n^*}{1+n^*} = \frac{1-n+jk}{1+n-jk} \qquad (3.23)$$

The reflectance R is then defined by:

$$R = |r|^2 = \left|\frac{1-n+jk}{1+n-jk}\right|^2 = \frac{(1-n)^2+k^2}{(1+n)^2+k^2} \qquad (3.24)$$

And refractive index can be calculated by using following equation

$$n = \left(\frac{1+R}{1-R}\right) + \sqrt{\frac{4R}{(1-R)^2} - k^2} \qquad (3.25)$$

Notice that whenever k is large, for example over a range of wavelengths, the absorption is strong, and the reflectance is almost unity. The light is then reflected, and any light in the medium is highly attenuated.

Extinction coefficient can be determined from the relation as follows

$$k = \frac{\alpha\lambda}{4\pi} \qquad (3.26)$$

Optical conductivity [17] of the thin films is calculated by using the following equation

$$\sigma_{opt} = \frac{\alpha n c}{4\pi} \qquad (3.27)$$

3.4.5 Instrumentation

A diagram of the components of a typical spectrometer is shown in the following Figure 3.9. The functioning of this instrument is relatively straightforward. A beam of light from a visible and/or UV light source (colored red) is separated into its component wavelengths by a prism or diffraction grating. Each monochromatic (single wavelength) beam in turn is split into two equal intensity beams by a half-mirrored device. One beam, the sample beam (colored magenta), passes through a small transparent container (cuvette) containing a solution of the compound being studied in a transparent solvent. The other beam, the reference (colored blue), passes through an identical cuvette containing only the solvent.
The intensities of these light beams are then measured by electronic detectors and compared. The intensity of the reference beam, which should have suffered little or no light absorption, is defined as I_0. The intensity of the sample beam is defined as I. Over a short period of time, the spectrometer automatically scans all the component wavelengths in the manner described. The ultraviolet (UV) region scanned is normally from 200 to 400 nm, and the visible portion is from 400 to 800 nm.

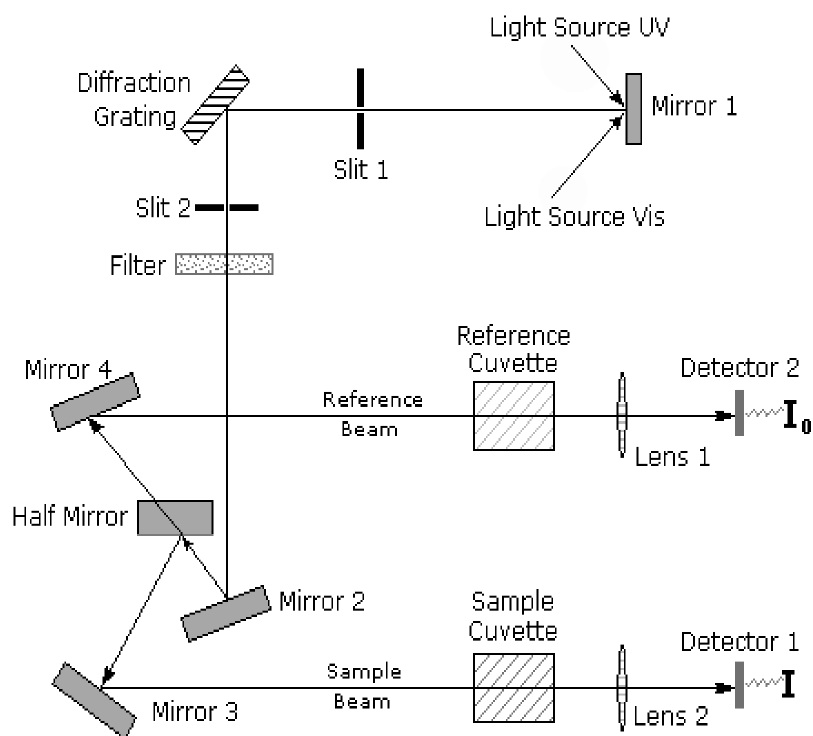

Figure 3.9: Schematic diagram of the components of a spectrometer

If the sample compound does not absorb light of a given wavelength, $I = I_0$. However, if the sample compound absorbs light then I is less than I_0, and this difference may be plotted on a graph versus wavelength, as shown on the right. Absorption may be presented as transmittance or absorbance. If no absorption has occurred, T = 1.0 and *A*= 0. Most of the sample compound does not absorb light of a given wavelength, $I = I_0$. However, if the sample compound absorbs light then I is less than I_0, and this difference may be plotted on a graph versus wavelength, as shown on the right. Absorption may be presented as transmittance or absorbance. If no absorption has occurred, T = 1.0 and *A*= 0. Most spectrometers display absorbance on the vertical axis, and the commonly observed range is from 0 (100% transmittance) to 2 (1% transmittance). The wavelength of maximum absorbance is a characteristic value, designated as λ_{max}. Different compounds may have very different absorption maxima and absorbances. Intensely absorbing compounds must be examined in

dilute solution, so that significant light energy is received by the detector, and this requires the use of completely transparent (non-absorbing) solvents. The most commonly used solvents are water, ethanol, hexane and cyclohexane.

Figure 3.10: A UV-vis spectrophotometer

3.4.6 Experimental procedure

In this work, the optical properties of the thin films are studied by UV-visible spectroscopic measurements. UV-visible absorption spectra were recorded using a dual beam UV-visible spectrophotometer (SHIMADZU UV-1601) shown in Figure 3.10 in the wavelength range of 190-1100 nm at room temperature. The transmission and absorption spectra were recorded both for the ZnO and ZnO: B thin films of concentration 0.50 - 1.50 at%. A blank glass slide was used as the reference during the optical absorption measurement of thin films.

3.5 Electrical Characterization

Electrical characterization of a semiconductor involves the measurement of the resitivity (ρ). The techniques for measuring ρ are very well known and have been documented in several literatures [18, 19]. Some methods of resistivity measurement are as follows:

i. Direct method,
ii. Two-point method,
iii. Linear four-probe method,
iv. Van der Pauw technique, etc.

Some of these methods are discussed in the following section.

3.5.1 Direct method

The resistivity of a thin film can be measured easily by using direct method. If the current I is flowing along L and voltage drop across L is V, then R=V/I and then by using the following equation, one can easily determine the resistivity (ρ) if the thickness of the film t is known

$$\rho = \frac{RWt}{L} \quad (3.19)$$

If W = L, i.e. film having square shape, then ρ and corresponding conductivity (ζ) are defined by the following equations,

$$\rho = Rt \quad (3.20)$$

$$\zeta = 1/\rho \quad (3.21)$$

Thus one can easily determine the resistivity as well ζ by measuring the sheet resistance R and film thickness t.

3.5.2 Two point probe method

Two point probe method is usually used for a relatively uniform specimen, to nullify the effect of contact resistance. The simple circuit diagram is shown in Figure 3.11. To avoid heating of the sample, current in the circuit must be kept low; the voltmeter must have high-input impedance. Measurement should be made far away from the contact so that minority carriers may be recombined before they reach probes.

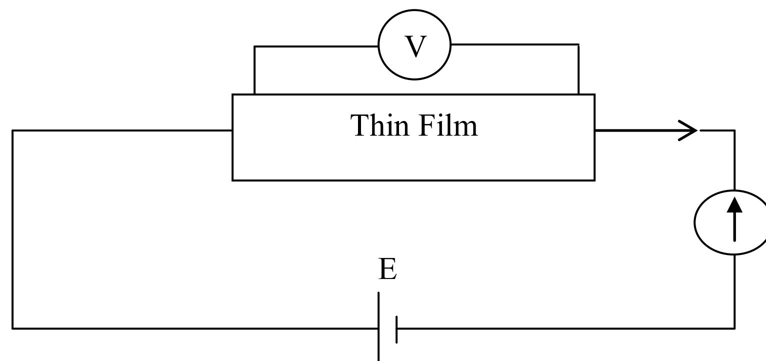

Figure 3.11: Circuit arrangement of resistivity measurement by two point probe method

Contact noise due to sample current through the probe contacts avoided and since the cutting can be done with a dye in an ultrasonic cutter, the probe spacing will be constant from sample to sample. The current I through the sample and the voltage drop V between the probes can be measured. And resistivity can be evaluated from,

$$\rho = \frac{A}{d}\left(\frac{V}{I}\right) \qquad (3.22)$$

where d is the probe spacing and A is the cross-sectional area of the sample.

3.5.3 Linear four point probe method

One of the most general techniques for resistivity measurement is the linear four point probe method. The four probes should be collinear with equal spacing. Current is supplied through the outer probes and the voltage drop between the inner two probes is measured (Figure 3.12

and 3.13). The resistivity of a sample, relatively large compared to the probe spacing may be estimated from the following equation,

$$\rho = \frac{2\pi\left(\frac{V}{I}\right)}{\frac{1}{S_1}+\frac{1}{S2}-\frac{1}{(S_1+S_2)}-\frac{1}{(S_2+S_3)}} \tag{3.23}$$

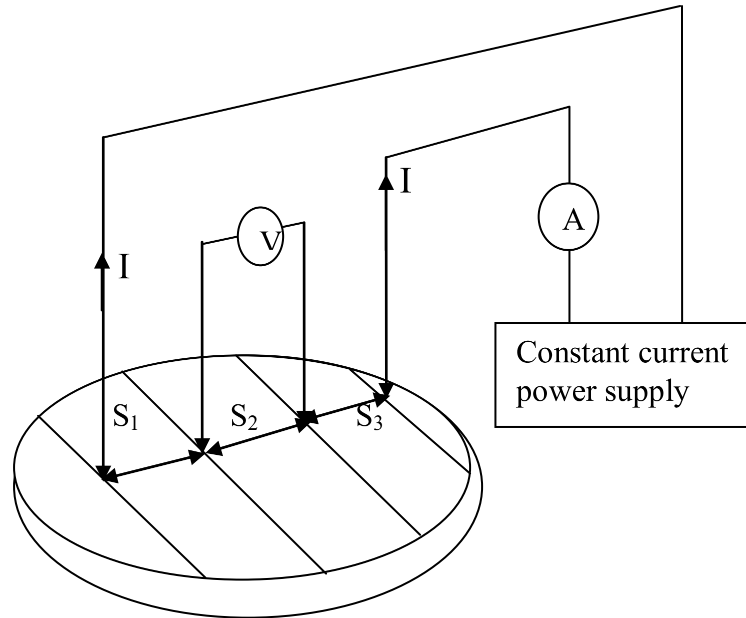

Figure 3.12: Circuit of linear four point probe for measuring resistivity

where, S_1, S_2 and S_3 are the probe spacing. When the probes are equally spaced, i.e., $S_1= S_2=S_3=S$. Then Eq (3.23) becomes,

$$\rho = 2\pi S\left(\frac{V}{I}\right) \tag{3.24}$$

The right hand side of the equation should be multiplied by correction factors of sheet resistance (C.F.1), film thickness (C.F.2) and temperature (C.F.3) [20]. Since, the thin films were square in shape and the ratio of the side of the square (D) and the probe distance (S) is <3, C.F.1 is not required here. The film thickness t is much less than S and t/S<0.4, thus C.F.2 is 1. Temperature correction for room temperature condition is ~1.0. So, equation (3.24) can directly be used for calculation of resistivity.

Figure 3.13: Experimental set up for electrical measurement

3.5.4 Van der Pauw technique

Electrical resistivity of metal and semiconductor film of any shape may be measured by using Van der Pauw method [21]. The resistivity of film having any arbitrary shape can be uniquely determined by using this method. To explain this method, let us consider the Figure 3.14, if A, B, C, and D are any four sufficiently small, ohmic contacts arranged successively on the circumference of a film of any arbitrary shape.

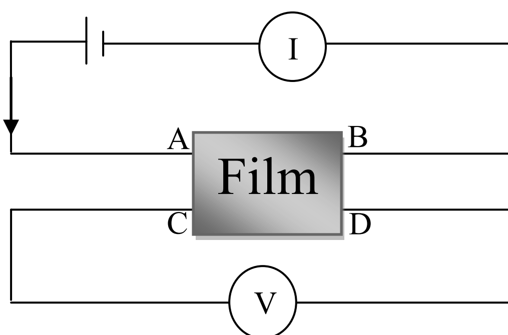

Figure 3.14: Experimental arrangements for measuring resistivity by using Van der Pauw‟s method

If a current I_{AB} entering into the film through the contact A and leaving it from the contact B and produces a potential difference V_{DC} between points D and C then

$$R_{AB,CD} = \frac{V_{DC}}{I_{AB}} \quad (3.24)$$

Similarly, we can write

$$R_{CD,AB} = \frac{V_{BA}}{I_{CD}} \quad (3.25)$$

$$R_{BC,DA} = \frac{V_{AD}}{I_{BC}} \quad (3.26)$$

$$R_{DA,BC} = \frac{V_{CB}}{I_{DA}} \quad (3.27)$$

Using reciprocal theorem Van der Pauw (1958) showed that

$$\rho = 4.543t \left(\frac{R_{AB,CD} + R_{BC,DA}}{2}\right) f \quad (3.28)$$

The correction factor f has been calculated by Van der pauw and is equal to unity when

$R_{AB,CD} \cong R_{BC,DA}$ and then equation (3.28) becomes,

$$\rho = 2.266t \,(R_{AB,CD} + R_{BC,DA})\ (\Omega\text{-m}) \quad (3.29)$$

Where, t is the film thickness in cm. and corresponding conductivity is defined as,

$$\rho = \frac{1}{\sigma}\ (\Omega\text{-m})^{-1} \quad (3.30)$$

3.5.5 Factors affecting resistivity measurement

The effects of the following factors are remarkable in the measurement of resistivity:

a. Length to breadth ratio, L/b of the film

b. Current electrodes

c. Current density

d. Microscopic inhomogenity of the film

e. Sensitivity of the measuring devices

f. Electrical contact resistivity

3.6.7 Activation energy

The energy required to transfer charge from one initially neutral island to another is known as activation energy and denoted by ΔE. This is equivalent to the electrostatic binding energy of the charge to the island. When these charge carriers are excited to at least this energy from the Fermi-level there will be tunneling from one island to another. These islands or small particles are called crystallites. The activation energy is related with film conductivity [22] and given by the relation

$$\sigma = \sigma_0 \exp(-\Delta E/2K_B T) \quad (3.33)$$

Where, ζ_0 is the conductivity at 0^0C and K_B is the Boltzmann constant and T is the absolute temperature. Equation (3.33) can be written as

$$\ln\sigma = -\frac{\Delta E}{2K_B T} + \ln\sigma_0 \quad (3.34)$$

Equation (3.34) is equivalent to a straight line equation, y = mx+c. So that ΔE can be determined from the slope of the straight line. From the graph of $\ln\zeta$ vs.1/T, ΔE can be calculated by using the relation

$$\Delta E = -\left(\frac{\ln\sigma}{\frac{1}{T}}\right) \times 2K_B \text{ (eV)} \quad (3.35)$$

3.6 Thickness Measurements

Thickness is one of the most significant film parameters. It may be measured either by in-situ monitoring of the rate of deposition, or after the film is taken out of deposition chamber. The methods are chosen on the basis of their convenience, simplicity and reliability. In-situ monitoring generally allows both monitoring and controlling of the deposition rate and film thickness. Other technique is thickness measurement with the help of optical interference. Since the film thicknesses are generally of the order of a wavelength of light, various types of optical interference phenomena have been found to be most useful for measurement of film thicknesses. Multiple-Beam interferometry technique (Tolansky method) [23] was employed for the measurement of thickness of the thin films. A brief description of the method is given below. This method utilizes the resulting interference effects when two silvered surfaces are brought close together and are subjected to optical radiation. This interference technique, which is of great value in studying surface topology in general, may be applied simply and directly to film-thickness determination. When a wedge of small angle is formed between unsilvered glass plates, which are illuminated by monochromatic light, broad fringes are seen arising from interference between the light beams reflected from the glass on the two sides of the air wedge. At points along the wedge where the path difference between these two beams are an integral and odd number of wavelengths, bright and dark fringes occur respectively. If the glass surfaces of the plates are coated with highly reflecting layers, one of which is partially transparent, then the reflected fringe system consists of very fine dark lines against a bright background. A schematic diagram of the multiple-beam interferometer along with a typical pattern of Fizeau fringes from a film step is shown in Figure 3.15. As shown in this figure, the film whose thickness is to be measured is over coated with a silver layer to give a

good reflecting surface and a half-silvered microscope slide is laid on top of the film whose thickness is to be determined. A wedge is formed by the two microscope slides and light multiply reflected between the two silvered surfaces forms an interference pattern with a discontinuity at the film edge as shown in Figure 3.15. The thickness of the film "d" can then be determined by the relation,

$$d = \frac{\lambda}{2} \times \frac{b}{a} \tag{3.36}$$

where, λ is the wavelength and *b/a* is the fractional discontinuity identified in the Figure 3.15. In general, the sodium light is used, for which λ = 5893 Å. Figure 3.16 shows an image of the fringes formed during interference.

Image Plane

Microscope

Monochromatic Source

Glass plate

Collimating lens

Reference plate (Half silvered)

Film to be measured

Substrate

b

a

Step height

Fringe spacing

Figure 3.15: Interferometer arrangement for producing reflection Fizeau fringes of equal thickness

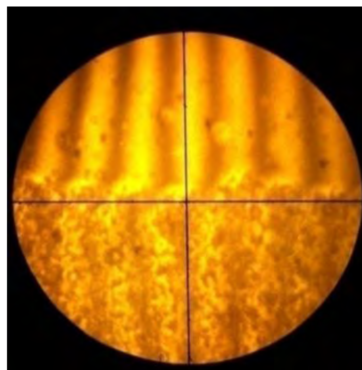

Figure 3.16: Interference pattern observed during measurement of film thickness

References

[1] Vankar, V. D., Das, S. R., Nath, P., Chopra, K. L., "Structure of vacuum, evaporated $Cd_xZn_{1-x}S$ thin films", Phys. Stat. Sol.(a), 45(2), 665-669, (1978).

[2] Stturkey, L., "Symposium on Advances I Techniques in Electron Metallography", American Society for Testing and Materials Philadelphia, PA, (1963).

[3] Barrett, C. S., Massalski, T. B., "Structure of Metals", McGraw-Hill Book Company: New York, (1966).

[4] Maissel, L. I., Glang, R., "Handbook of Thin Film Technology" McGraw-Hill Book Company: New York, (1970).

[5] Hirsch, P. B., Howie, A., Nilcholson, R.B., Pashly, D.W., Whelan, M.J., Electron "Microscopy of Thin Crystals", Butterworths: Washington D. C.,(1965).

[6] Howland, R., Benatar, L., "A Practical guide to Scanning Probe Microscopy", Park Scientific Instruments, (1996).

[7] Cullity, B. D., "Elements of X-ray Diffraction", Addison-Wesley Publishing Company. Inc. USA, (1959).

[8] Gupta, B. K., Agnihotri, O. P., "Structural investigations of spray-deposited CdS films doped with Cu, In and Ga", Phil. Mag.(b), 37, 631-633, (1978).

[9] Kumar, P., Misra, A., Kumar, D., Dhama, N., Sharma, T.P., Dixit, P.N., "Structural and optical properties of vacuum evaporated $Cd_xZn_{1-x}S$ thin films" Opt. Mater., 27(2), 261–264, (2004).

[10] Nelson, J. B., Riley, D.P., "An experimental investigation of extrapolation methods in the derivation of accurate unit cell dimension of crystals", Proc. Phys. Soc., 57, 160-177, (1945).

[11] Warren, B.E., "X-ray Diffraction", Addision Wesly Publishing Co.: London, (1969).

[12] De, C. K., N. K. Mishra , Ind. J. Phys. A 71(1997) 530.

[13] Bedir, M., Oztas, M., Bakkaloglu, O.F., Ormanci, R., "Investigations on Structural, Optical and Electrical Parameters of Spray Deposited ZnSe Thin Films with Different Substrate Temperature", Eur. Phys. J. B 45, 465-471, (2005).

[14] Bouguer, P., "Essai d'optique sur la gradation de la lumière", Claude Jombert: Paris, (1729).

[15] Davies, E. A., Mott N.F., "Conduction in non-crystalline system V. conductivity, optical absorption and photoconductivity in amorphous semiconductors", Phil. Mag. 22(179), 0903-0922, (1970).

[16] Wiener, O. W., J. Electron. Mater., 31, p53, 1887.

[17] Sharma, P., Sharma, V., Katyal, S.C., "Variation of optical constant in $Ge_{10}Se_{60}Te_{30}$ thin film", Chalcogen. Lett., 3(10), 73-79, (2006).

[18] McCarter, W. J., Starrs, G., Kandasami, S., Jones, R., Chrisp, M., "Electrode configurations for resistivity measurements on concrete", ACI Mater. J., 106(3), 258-264, (2009).

[19] Lataste, J. F., "Electrical resistivity measurement", in Non-Destructive Assessment of Concrete Structures, Springer, (2012).

[20] Paulnack, C. L., Chaplin, N.J., "Minimal Maintenance Probe for Precise Resistivity Measurement of Semiconductors", Rev. Sci. Instrum. 33, 873-875, (1962).

[21] Van der Pauw, L. J., "A Method of Measuring Specific Resistivity and Hall Effect of Discs of Arbitrary Shape", Philips. Res. rept.13(1), 1-9, (1958).

[22] Kittel, C., "Introduction to Solid State Physics", John Wiley & (ASIA) Pte. Ltd., (1996).

CHAPTER 4

SAMPLE PREPARATION

CHAPTER 4

SAMPLE PREPARATION

4.1 Preparation of Thin Films

Thin film preparation consists of four sequential steps (Figure 4.1). A source of film material is supplied. The material is transported to the substrate and deposition takes place. The films are characterized by various experimental techniques and finally the results are analyzed to evaluate the process.

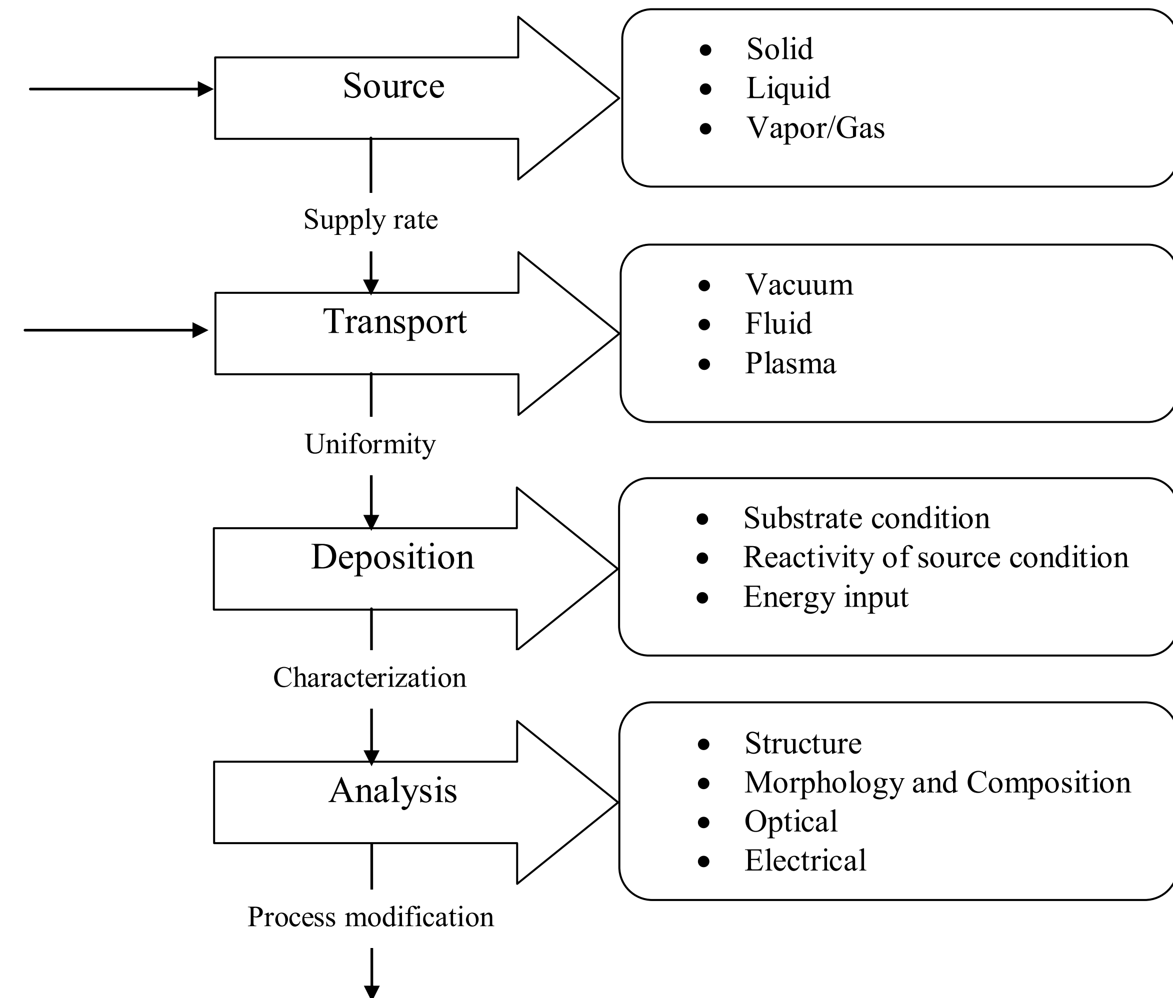

Figure 4.1: Steps of thin film processes

Spray pyrolysis (SP) is one the most common techniques used for deposition of thin films. In this work, ZnO and ZnO: B thin films are prepared by using a locally fabricated SP

deposition (SPD) unit. This chapter includes a brief discussion on the SPD unit and various steps of preparation of ZnO and ZnO: B thin films on glass substrate by SPD technique.

4.1.1 Experimental details

4.1.1.1 Preparation of masks

The direct deposition of thin film pattern requires a suitably shaped aperture, commonly referred to as a mask. For the purpose of various experimental studies, film of specific size and shape are required. Mask is made from stainless steel plate with the desired pattern cut into it. The aperture is made in a bath machine.

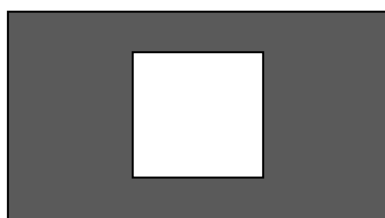

Figure 4.2: Mask for the sample

The mask is placed in proximity to the substrate, thereby allowing condensation of the evaporated only in the exposed substrate areas. The mask is prepared in such a way that the edge of the mask is smooth so that it is helpful for determining the film thickness accurately (Figure 4.2).

4.1.1.2 Heater

The heater „H‟ is an ordinary hot plate 2 kW nichrome wire heater. The top of the plate is covered with a piece of asbestos sheet having a small open area at the center where a mica sheet is attached. A thick stainless steel plate „G‟ (Figure 4.3) is placed on this mica sheet. Substrate is placed on this susceptor plate „G‟ to have a uniform temperature throughout the substrate surface. An electrical voltage variac controls the heater power.

4.1.1.3 The design of the reactor

The design of the reactor is shown is Figure 4.3. It is a vertical batch type reactor composed of a galvanized iron enclosure „E‟, heater „H‟ and heat susceptor „G‟. For the rapid expulsion of the by-product gases there are opening at the side and at the top of the reactor. It helps focusing the incoming sprayed solution towards the substrate „S‟ and also provides a chimney action to the exhaust gas upwards.

4.1.1.4 The fume chamber

It is a large type chamber with a slanting top and is provided with a chimney. There is an exhaust fan fitted at the mouth of the chimney to remove the unused gases from the chamber. The slanting top and the sidewalls are made of glass and wood. There are airtight doors in the front side. The chamber has purging facilities. The whole spray system and the reactor are kept inside this fume chamber at the time of film deposition because of the safety grounds and to check air current disturbances at the deposition site. These two points just stated are very important for the spray process when deposition is carried out in open- air atmosphere.

4.1.1.5 Air compressor

It is reservoir type electrical air compressor. A rotary pump in this section mode draws atmospheric air and keeps it reserved in a large capacity air tank. At the outlet of the tank a pressure gauge is attached which records the pressure of the air at the time of supplying it from the tank. There is a bypass control valve which can keep the output pressure constant.

4.1.1.6 Spray head/ nozzle

The single spray nozzle consists of capillary tubes (stainless steels) fitted perpendicular to the other tube as shown in Figure 4.3. When compressed air is passed rapidly through the upper tube „P" in direction tangential to the mouth of the lower tube „A", a partial vacuum is created at the front part of the tube „A" whose other end is kept immersed in the spray liquid. Due to this partial vacuum the liquid rises up through the tube „A" and the compressed air drives it away in the form of fine spray particles. The thinner spray nozzle would give the finer spray particles. A very fine needle shaped capillary tube was used for the spray nozzle and it may vary from nozzle to nozzle.

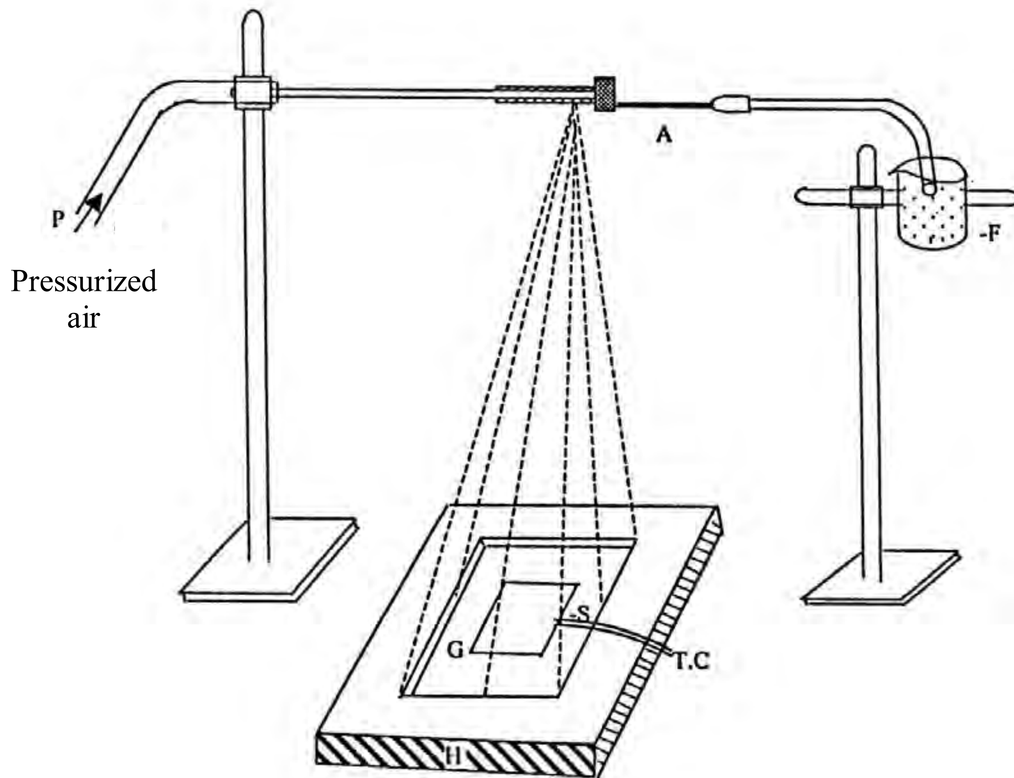

T.C. = Thermocouple	F = Beaker filled with solution	P = Upper tube
H = Heater	G = Graphite Block	A = Lower tube
	S = Substrate	

Figure 4.3: Schematic diagram of the experimental setup of spray pyrolysis technique

4.2 Substrate and Substrate Cleaning

For thin film deposition, several types of substrates are used. Substrate may influence various the properties of thin films [1]. Generally, glass, quartz, plastic and ceramic substrates are used for polycrystalline films. However, in the present work, thin films are deposited on glass substrates. The most commonly microscope glass slides having 5 cm long, 2 cm wide and 0.1 cm thickness are used. These are fine smooth high quality microscope glass slides. The cleaning of substrate has a major influence on the properties of the thin film deposited onto them. Surface contaminations manifest it in pinholes, which can cause open resistor or localized high resistance. The following procedures are used for substrate cleaning. The gross contamination of each of the substrates are first removed by warm aqueous solution of sodium carbonate and then washed with distilled water. After washing in distilled water, the substrates are dipped at first into nitric acid for some time and again washed in distilled water. These are then dipped into chromic acid for some time. Taking them out of

chromic acid bath one by one and then these are washed and thoroughly rinsed with deionized water for several times. Finally, these are dried in hot air and preserved for use. During the whole process the substrates are always held by slide holding forceps.

4.3 Working Solution

The working solution is prepared by taking zinc acetate dihydrate [Zn $(CH_3COO)_2$. $2H_2O$] as a source material. The most commonly used solvents are distilled water and methanol. As Zn $(CH_3COO)_2$. $2H_2O$ dissolves in water at room temperature, water is taken as solvent. Since, the spray system used in the present experiment operates via a partial vacuum path as the mouth of the spray nozzle, the concentration of the solution prepared by the solvent is made in such a way that it could be at least be drawn by the nozzle. If the solution concentration is high the spray rate will be low. A typical value of solution concentration 0.1 M is used in this work. In order to prepare the ZnO: B thin films, the aqueous solution of zinc acetate and boric acid (H_3BO_3) are used as the precursor solution.

4.4 Deposition Parameters

In the SPD technique the structure, composition and other characteristics of the deposited thin films depend on a number of process variables (deposition parameters). The deposition parameters such as the substrate temperature (T_s), type and concentration of solution (C), flow rate of the solution (S_r), deposition time (t_d), quality of the substrate material, size of atomized particles, carrier air pressure (P_a) and substrate to spray outlet distance (d_s), etc. affect the properties of thin films. It is obvious that T_s is the most important deposition parameter and it must be controlled with great care.

For the deposition of ZnO and ZnO: B thin films onto glass substrates, the deposition parameters t_d, S_r, d_s, P_a, and C are kept constant. ZnO and ZnO: B thin films are deposited at various substrate temperatures (T_s) from 300 to 450 °C. ZnO: B thin films are prepared by changing the B doping concentration between 0.50 and 1.50 at% at constant values of T_s. The effect of these two film parameters on the structural, optical and electrical properties of ZnO and ZnO: B thin films are studied in this work.

4.5 Rate of Deposition

The rate of flow of the working solution can be controlled by a suitable designing of nozzle „A‟ and adjusting the air flow rate. In preparing ZnO and ZnO:B thin films, the solution flow rate is maintained about 0.50 ml/min.

4.6 Thickness Control

Thickness plays an important role in the properties of thin films unlike a bulk material [2-4]. In the present SPD process, the deposition time plays the main role in controlling the thickness of the thin films, provided the other parameters, remain constant. Since the deposition is carried out in normal atmosphere a direct and insitu control of thickness is not so easy. To control the film thickness therefore calibration chart may be used. These charts are generally plots of deposition time vs. thickness, and can be prepared at different constant substrate temperatures prior to the preparation of particular experimental samples using the same solution and deposition variables.

4.7 Sample Deposition

It has been stated earlier that SPD is a low cost technique for preparing ZnO thin films [5-7], which consist basically of spraying solution on a heated substrate. The apparatus needed to carry out the chemical spray process consists of a device to atomize the spray solution and a substrate heater. Figure 4.3 shows a schematic diagram of SPD unit and Figure 4.4 shows the experimental setup for SPD used in this work. A considerable amount of (about 100 ml) solution is taken in the container „F" fitted with the spray nozzle „A". The clean glass substrate with a suitable mask was put on the susceptor of the heater „H". The distance between the tip of the nozzle and the surface of the glass substrate was kept 25 cm. Before supplying the compressed air the substrate temperature „T_s" was to be kept at a level slightly higher than the required substrate temperature because at the onset of spraying a slight fall of temperature is likely. The temperature of a substrate was controlled by controlling the heater power using a variac. The substrate temperature was measured by placing a copper constantan thermocouple on the substrate. When compressed air is passed through „P" at constant pressure of 0.50 bar, vacuum is created at the tip of the nozzle and the solution is automatically carried to the reactor zone in the form of spray and film is deposited on the heated substrate [8-10]. The solution is adjusted such that about 5 minutes of spray produces ZnO and ZnO: B thin films of thickness about 200 nm. The possible chemical reaction that takes place on the heated substrate to produce ZnO may be as follows:

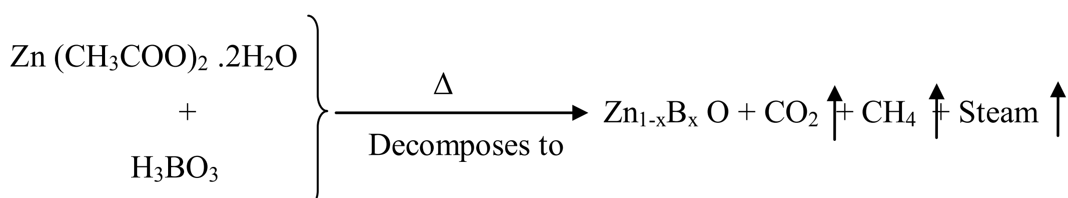

Figure 4.4: Experimental set up of Spray Pyrolysis unit at the Department of Physics, BUET

References

[1] Choudhury, C., Sehgal H. K., "Properties of spray deposited cobalt oxide selective coating on aluminum and galvanized iron substrate", Appl. Energy, 10, 313-324, (1982).

[2] Kadam, L. D. , Patil P. S., "Thickness- dependent properties of sprayed cobalt oxide thin films" Mater. Chem. Phys., 68, 225-232, (2001).

[3] Islam, M. R., Podder J., "Optical properties of ZnO nanofiber thin films grown by spray pyrolysis of zinc acetate precursor", Cryst. Res. Technol., 44(3), 286- 292, (2009).

[4] Affreen, S., Balamurugan D., Jeyaprakash B.G., "Thickness dependent physical property of spray deposited $ZnFe_2O_4$ thin film" J. Appl. Sci., 12: 1636-1640, (2012).

[5] Chamberlin, R. R., Skarman J. S., "Chemical spray deposition process for inorganic films", J. Electrochem. Soc., 113(1), 86-89, (1966).

[6] Altiokka, B., Aksay S., "Optical properties of CuInS2 films produced by spray pyrolysis method", J. Arts and Sci. Sayi., 3/May, 27-34, (2005).

[7] Riveros R., Romero E., Gordillo G., "Synthesis and characterization of highly transparent and conductive SnO2:F and In2O3:Sn thin films deposited by spray pyrolysis", Braz. J. Phys., 36(3B), 1042-1045, (2006).

[8] Elangovan, E., Ramamurthi K., "Studies on optical properties of polycrystalline SnO_2:Sb thin films prepared using $SnCl_2$ precursor", Cryst. Res. Technol. 38(9), 779-784, (2003).

[9] Anuar, K., Ho S. M., Tan W. T., Atan M. S., Kuang D., Jelas H. M., Saravanan N., "Effects of solution concentration on the properties of Cu4SnS4 thin films", Mater. Sci., 14(2), 101-105, (2008).

[10] Yadav, S. C., Uplane M. D., "Synthesis and properties of boron doped ZnO thin films by spray CVD technique at low substrate temperature", Int. J. Engr. Sci. Technol., 4(12), 4893-4898, (2012).

CHAPTER 5

RESULTS AND DISCUSSION

CHAPTER 5

RESULTS AND DISCUSSION

5.8 Introduction

The results obtained from various experimental measurements on ZnO and ZnO: B thin films are represented and discussed in this chapter.

5.9 Surface Morphology

SEM images of ZnO and ZnO: B thin films are presented in Figures 5.1 to 5.9. The SEM images of the thin films are taken at 1, 2.5, 5, and 30 k magnifications. In lower magnification, it is seen in Figure 5.1 that the scanned area is nicely covered with fibrous and non-fibrous ZnO thin films. SEM images discovered that sprayed particles are adsorbed on the glass substrate into clusters as the primary stage of nucleation. In higher magnification images, clusters appear as nanofibers around the nucleation center. Analogous type of feature was reported by Ilican *et al.* [1] for indium doped ZnO thin films deposited onto glass substrate at substrate temperature (T_s) of 350 °C by SPT and Caglar *et al.* [2] for ZnO: B thin films deposited onto ITO substrate by Sol-gel method, respectively. Figure 5.2 shows the SEM images of ZnO thin films which are deposited at the T_s of 350, 400 and 450 °C. SEM images 0.50 and 0.75 at% ZnO: B thin films (Figure 5.3 and 5.4) exhibit that the nanofibers are thicker and more closely spaced compared to those in ZnO thin films (Figure 5.2). The thickness of the nanofibers decreases in 1.00 and 1.50 at% ZnO: B thin films (Figure 5.5 and 5.6). The distance between nanofibers increases due to the increase of substrate temperature from 350 to 450 °C. At x 30 k, it is observed that the shapes of the particles forming the nanofibers are almost circular for the ZnO and ZnO: B thin films except for 1.50 at% B doping. Figure 5.7 shows that the nanofibers are not so compact and smooth for 1.50 at% ZnO: B thin films with respect to others. Thicknesses of the nanofibers are measured at x 30 k (Figure 5.8). Thickness of the nanofibers increases slightly with the increase of T_s. The

average thickness of the nanofibers increases with the increase of B doping up to 0.75 at% and then it decreases for 1.00 and 1.50 at% of B doping. The average thickness of the nanofibers in ZnO and ZnO: B thin films vary from 200 to 550 nm. The droplet size is found between 10 – 28 μm (Figure 5.9).

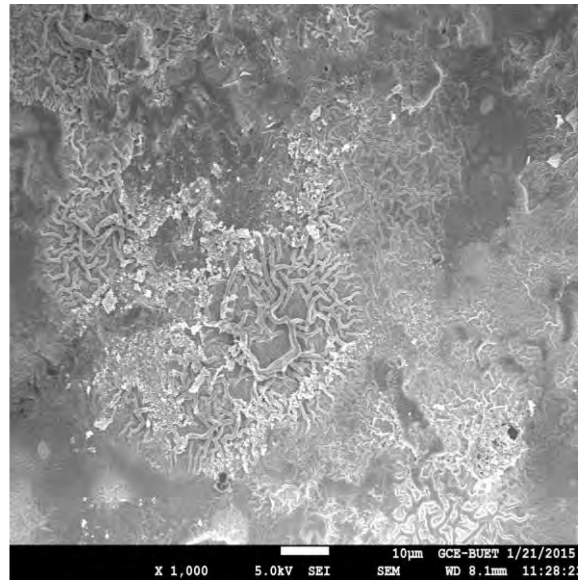

Figure 5.1: SEM image (x 1 k) of ZnO thin film deposited at 300 °C

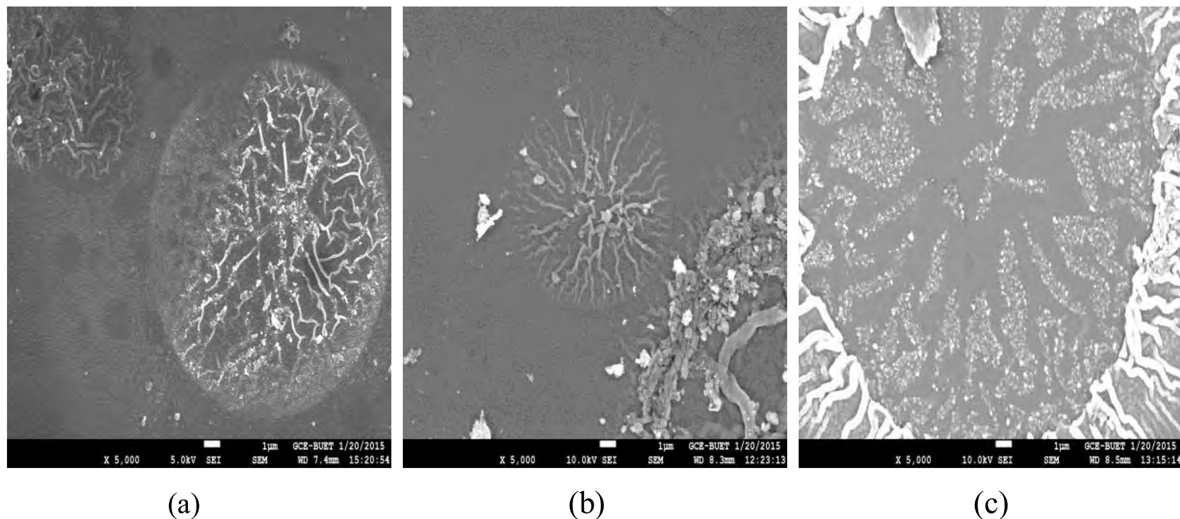

Figure 5.2: SEM images (x 5 k) of ZnO thin films deposited at the T_s of (a) 350, (b) 400 and (c) 450 °C

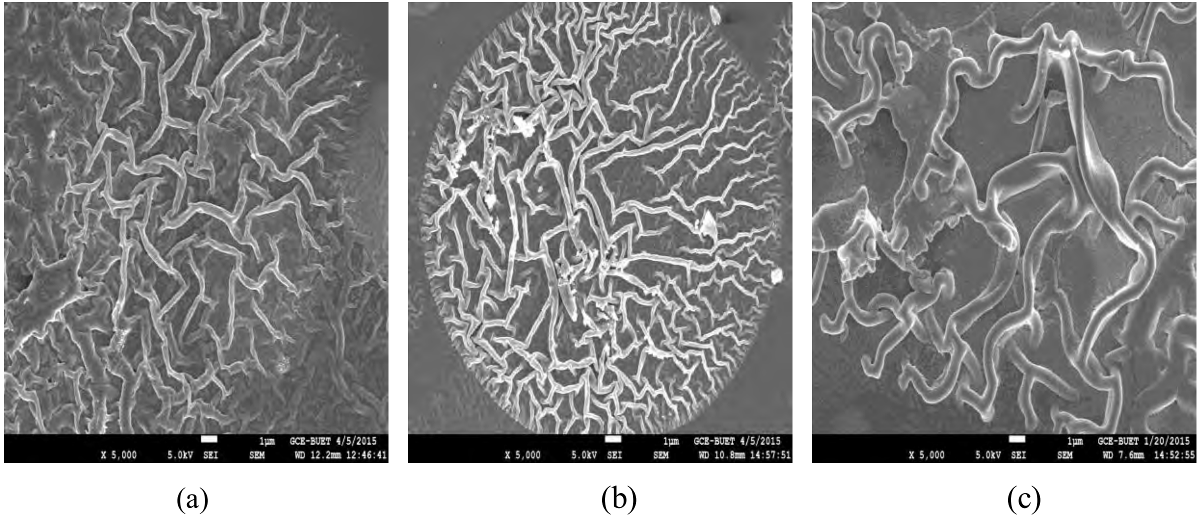

Figure 5.3: SEM images (x 5 k) of 0.50 at% ZnO: B thin films deposited at the T_s of (a) 350, (b) 400 and (c) 450 °C

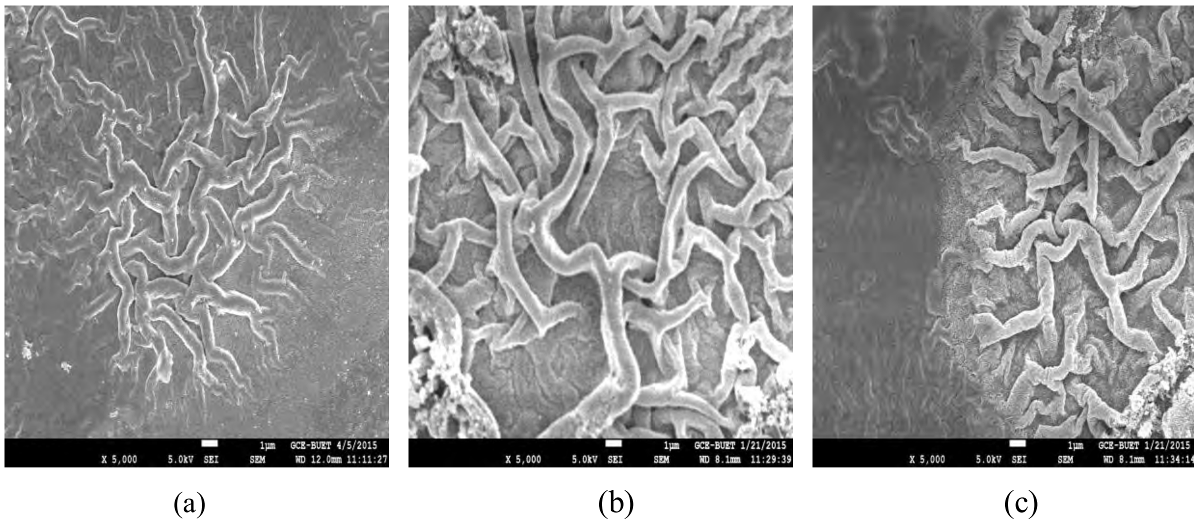

Figure 5.4: SEM images (x 5 k) of 0.75 at% ZnO: B thin films deposited at the T_s of (a) 350, (b) 400 and (c) 450 °C

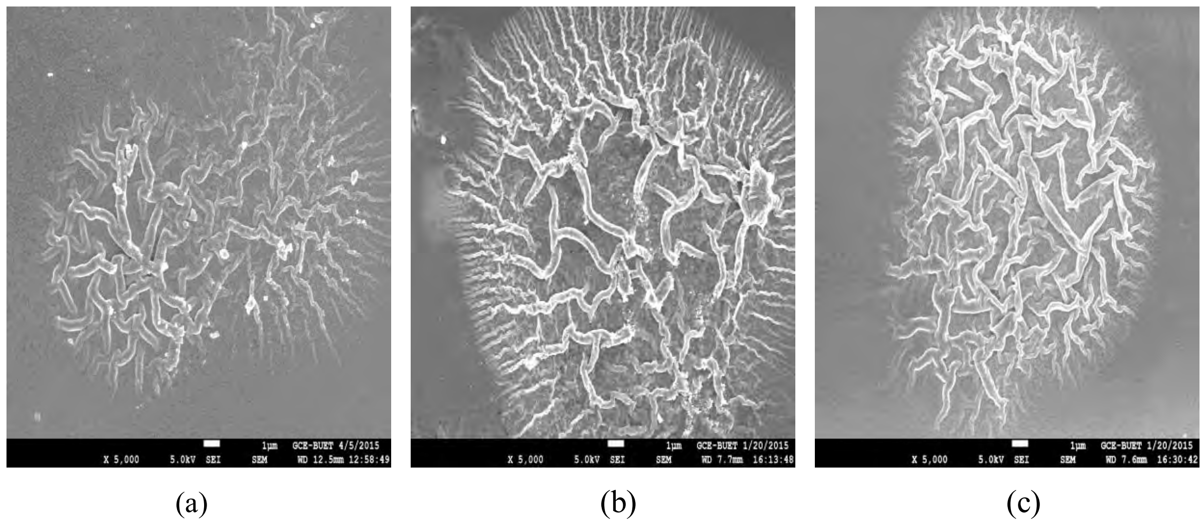

Figure 5.5: SEM images (x 5 k) of 1.00 at% ZnO: B thin films deposited at the T_s of (a) 350, (b) 400 and (c) 450 °C

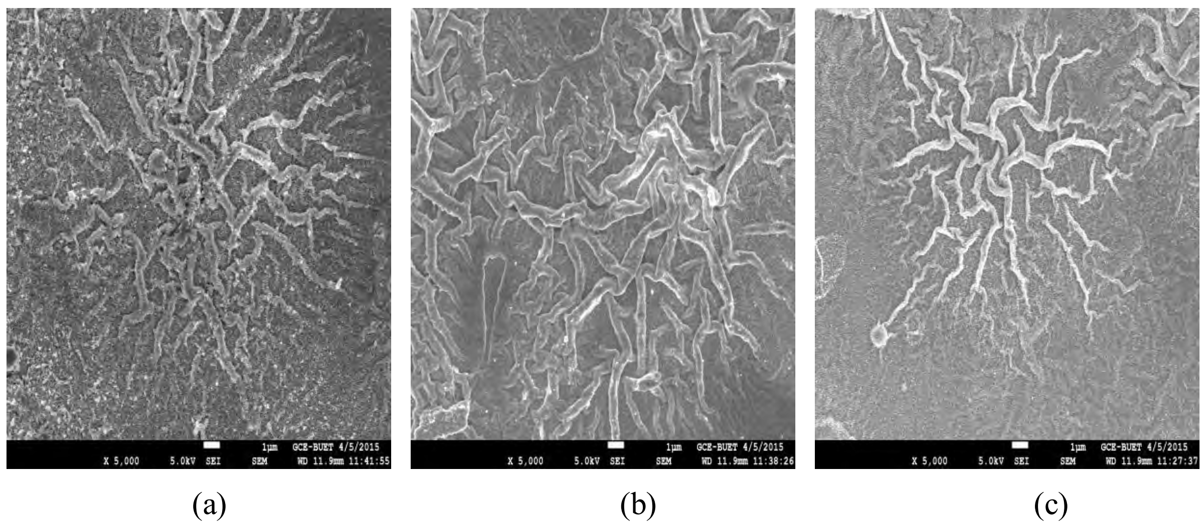

Figure 5.6: SEM images (x 5 k) of 1.50 at% ZnO: B thin films deposited at the T_s of (a) 350, (b) 400 and (c) 450 °C

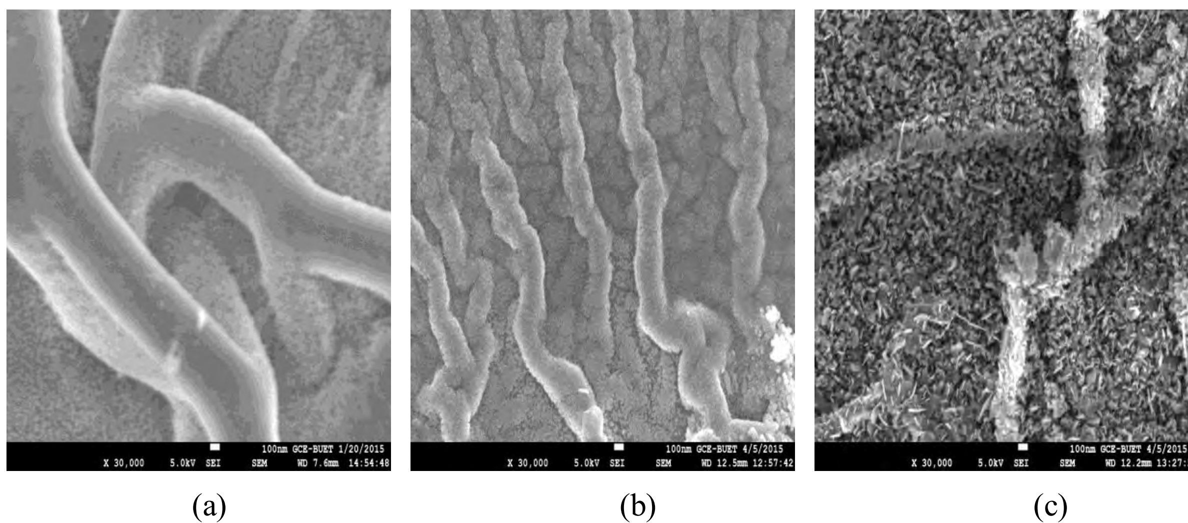

(a) (b) (c)

Figure 5.7: SEM images (x 30 k) of (a) 0.50, (b) 1.00 and (c) 1.50 at% ZnO: B thin films deposited at the T_s of 450 °C

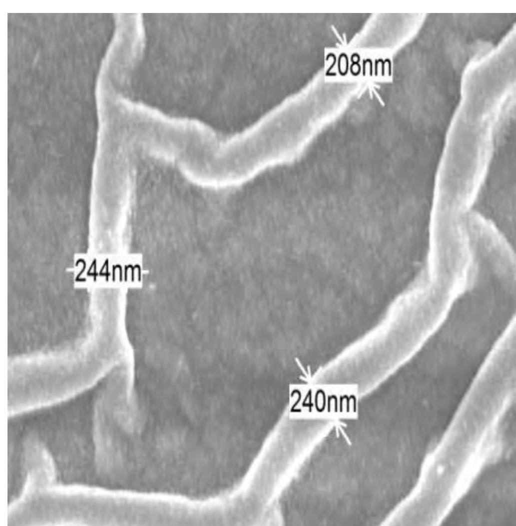

Figure 5.8: SEM image (x 30 k) shows nanofiber thickness

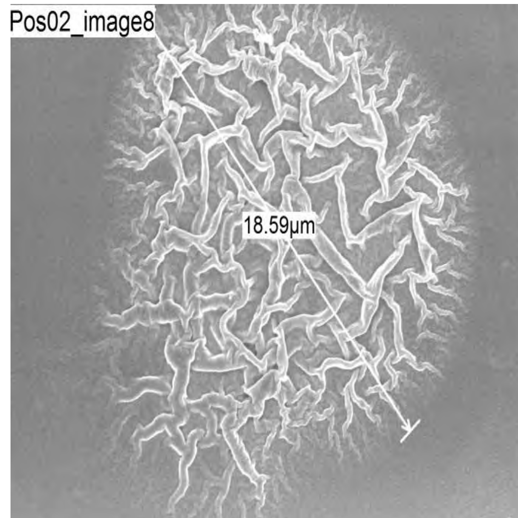

Figure 5.9: Droplet size is shown in an SEM image (x 2.5 k)

5.10 Elemental Analysis

Elemental analysis of ZnO and ZnO: B thin films are carried out by EDX spectroscopy. EDX spectra of ZnO and ZnO: B thin films are showed in Figures 5.10 (a) - (e) and the quantitative analysis of the elements are presented in the Tables 4. Two strong peaks corresponding to Zn and O are observed in the spectrum of ZnO thin film (Figure 5.10). It confirms the high purity of the ZnO thin film. There are small peaks for B impurity in the EDX spectra and quantitative analysis shows the increase in at % of B with the increase of concentration of B. It can be noticed in EDX analysis for ZnO: B thin film that at % of Zn is decreased with the increase of concentration of B. The quantity of O is not much affected due to increase of B doping. Thus, successful incorporation of B is confirmed by EDX analysis.

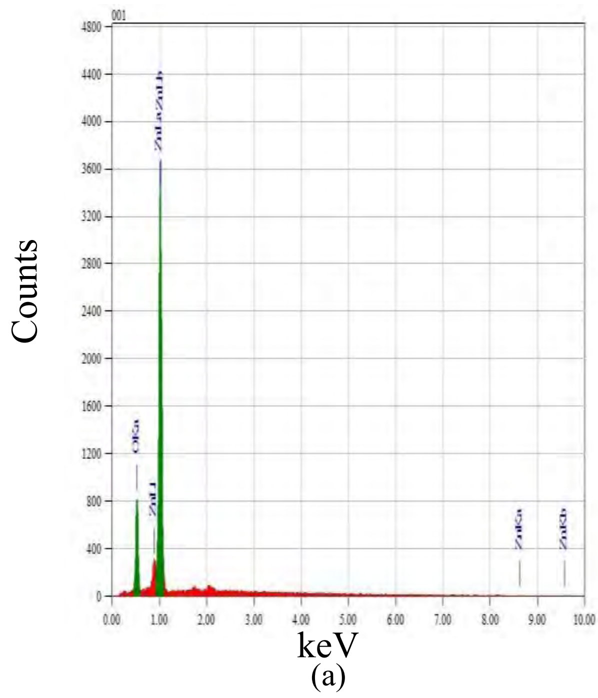

(a)

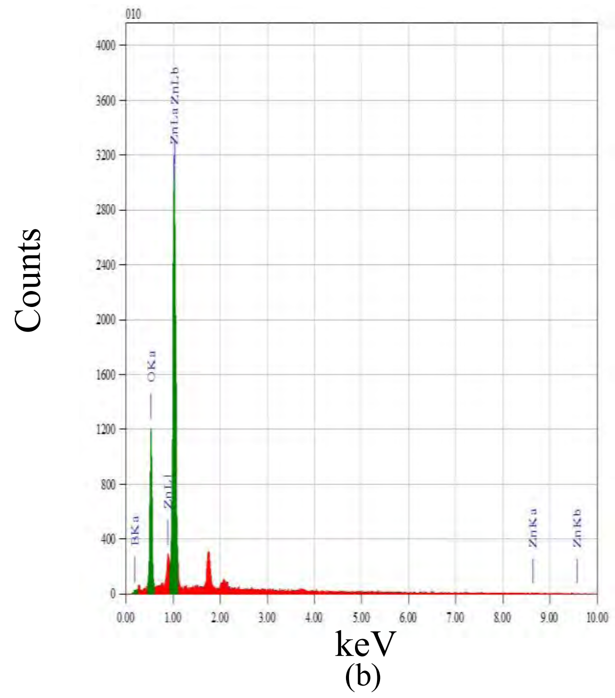

(b)

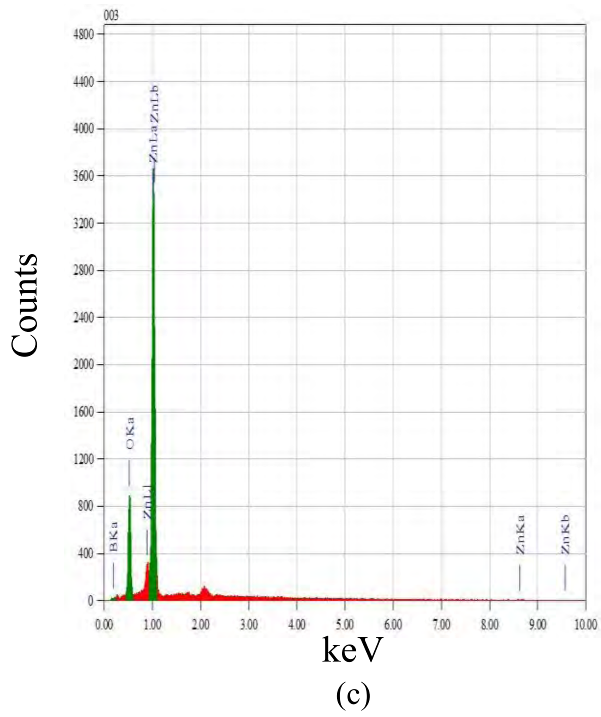

(c)

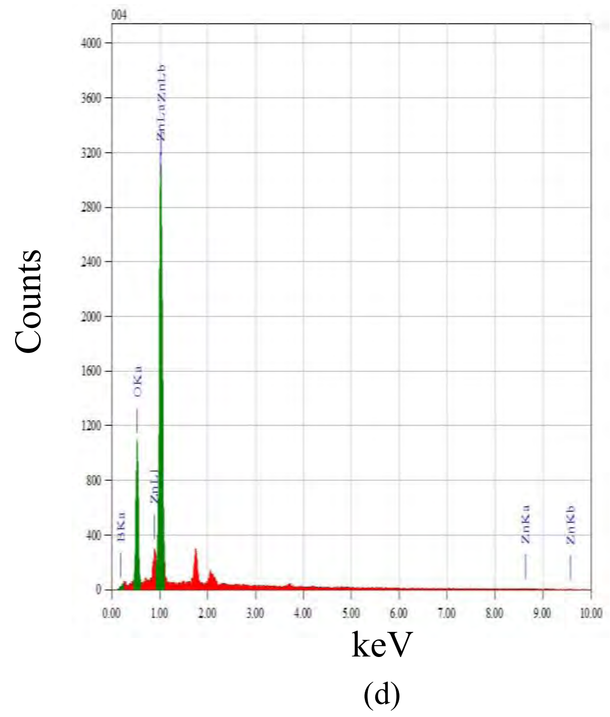

(d)

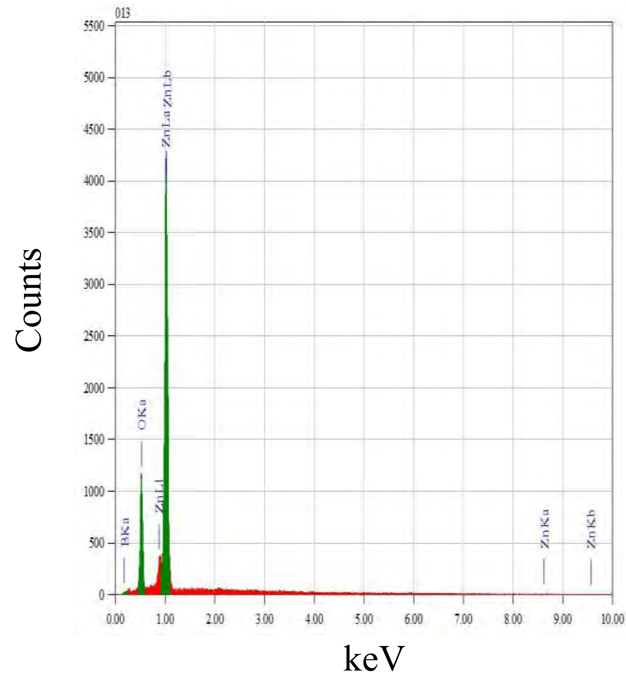

(e)

Figure 5.10: EDX spectra of (a) ZnO, (b) 0.50, (c) 0.75, (d) 1.00 and (e) 1.50 at% ZnO: B thin films deposited at $T_s = 300$ °C

Table: 4. The EDX analysis of ZnO and ZnO: B thin films

Sample	Elements								
	B			Zn			O		
	T_s (°C)								
	350	400	450	350	400	450	350	400	450
	at%								
ZnO	-	-	-	48.45	49.79	47.95	51.55	50.21	52.05
0.50 at% ZnO: B	2.61	3.08	2.58	38.68	43.47	43.83	58.71	53.45	53.60
0.75 at% ZnO: B	3.25	2.50	10.18	45.38	50.60	46.89	51.37	46.89	46.67
1.00 at% ZnO: B	6.99	16.61	8.82	37.74	38.96	40.86	55.27	45.08	52.22
1.50 at% ZnO: B	8.81	10.82	13.08	40.86	37.46	44.93	50.33	51.71	41.99

5.11 X-ray Diffraction

The XRD patterns of ZnO and ZnO: B thin films, synthesized at the T_s of 300, 350, 400 and 450 °C are illustrated in the Figure 5.11. All the films show polycrystalline nature. The reflections are observed for (100), (002), (101), and (110) planes indicating hexagonal wurtzite type of crystal structure of the thin films. Among these peaks first three are well defined, but (110) peak is less intense one. No peak corresponding to B impurity is observed, that means B has substituted Zn from their lattice sites without changing the hexagonal type of structure. For the ZnO and ZnO: B thin films deposited at higher T_s the peaks are sharp and intensities of the peaks increase up to 1.0 at% B doping. ZnO: B thin films show preferred orientation along [002] direction [2]. It can be said that doping causes texturing along c-axis. The (110) peak is not found in the XRD patterns of 1.00 at% ZnO: B thin films (Figure 5.14), but there is increase in the intensities of the other peaks. The XRD patterns of 1.50 at% ZnO: B thin films show peaks with less intensities compared to other ZnO: B thin films. Decrease in intensity can be attributed as the deterioration of crystalline quality [3]. Lattice constants a and c of ZnO and ZnO: B thin films are calculated by the equations (3.2) and (3.4). The values of a and c are found from the Nelson-Riley plot. The values of a and c and the c/ a ratio of ZnO and ZnO: B thin films are presented in Tables 5 and 6. The lattice constants are comparable to the standard values for ZnO [4]. For all the films the lattice constants increase and decrease such that c/a ratio is comparable to that for an ideal hexagonal structure [5]. Crystallite size is calculated for the predominant peak (002) by using equation (3.5) and it is plotted against the B doping concentrations in Figure 5.12. Average crystallite size is determined between 27 and 88 nm. Maximum crystallite size is found for 0.50 at% ZnO: B thin films and then it decreases with the further increase of B concentration [6]. Larger crystallite size indicates less dislocation per unit area and minimum strain inside the crystallite. Microstrain (ε) and dislocation density (δ) are calculated by the equations (3.6) and (3.7) and these are plotted as a function of B concentration in Figure 5.12. Decrease of ε and δ with the increase of B concentration signifies less deformation of the crystallites at higher B concentration [7].

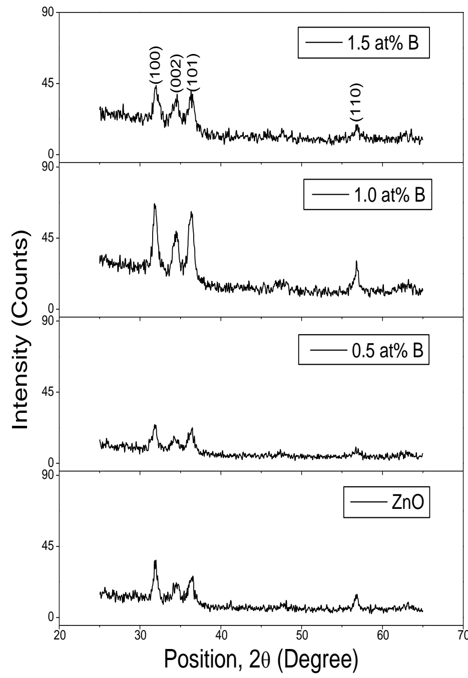

(a)

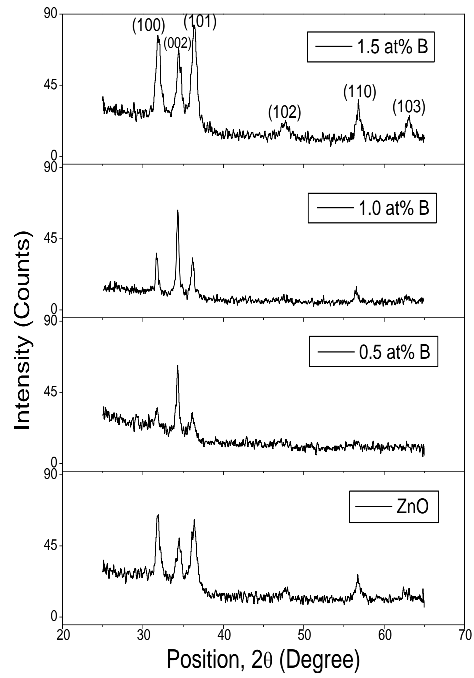

(b)

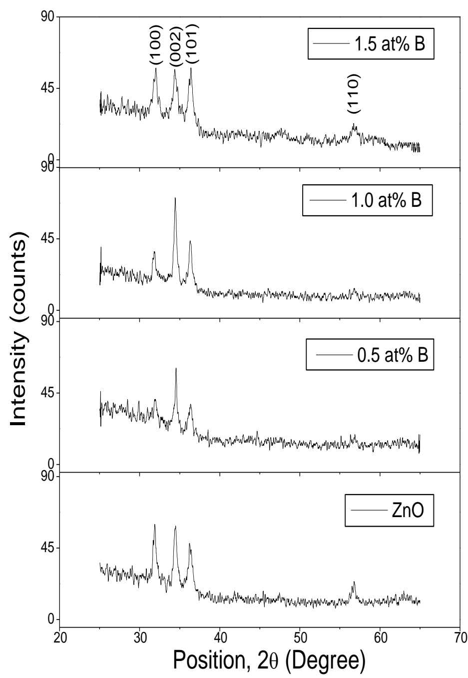

(c)

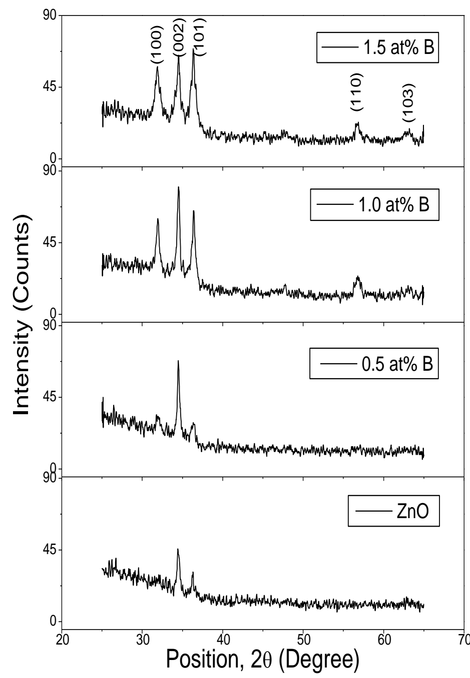

(d)

Figure 5.11: XRD patterns of ZnO and ZnO: B thin films deposited at the T_s of (a) 300, (b) 350, (c) 400 and (d) 450 °C

Table: 5. Lattice constants of ZnO and ZnO: B thin films deposited at various T_s

B concentration (at%)	a (Å)				c (Å)			
	T_s (°C)				T_s (°C)			
	300	**350**	**400**	**450**	**300**	**350**	**400**	**450**
0	3.2365	3.2482	3.2571	3.1823	5.2752	5.2947	5.2828	5.1877
0.50	3.2474	3.2484	3.2624	3.2371	5.2967	5.2947	5.3089	5.2689
1.00	3.2438	3.2392	3.2536	3.2388	5.2824	5.2796	5.2938	5.2760
1.50	3.2409	3.2497	3.2421	3.2464	5.2767	5.2874	5.2797	5.2854

Table: 6. c/a ratio for ZnO and ZnO: B thin films deposited at various T_s

B concentration (at%)	c/a			
	T_s (°C)			
	300	**350**	**400**	**450**
0	1.6299	1.6300	1.6293	1.6301
0.50	1.6310	1.6299	1.6272	1.6276
1.00	1.6284	1.6299	1.6270	1.6289
1.50	1.6281	1.6270	1.6284	1.6280

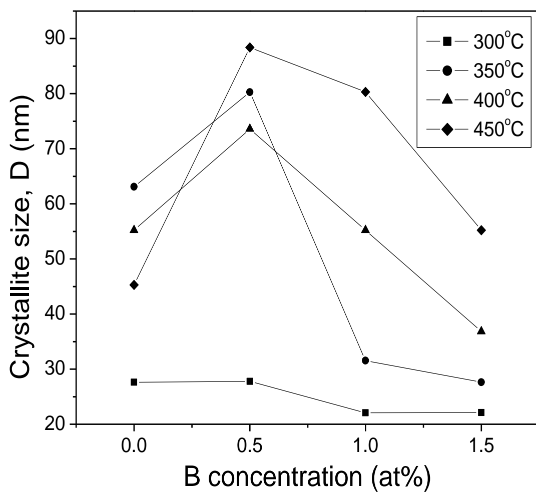

(a)

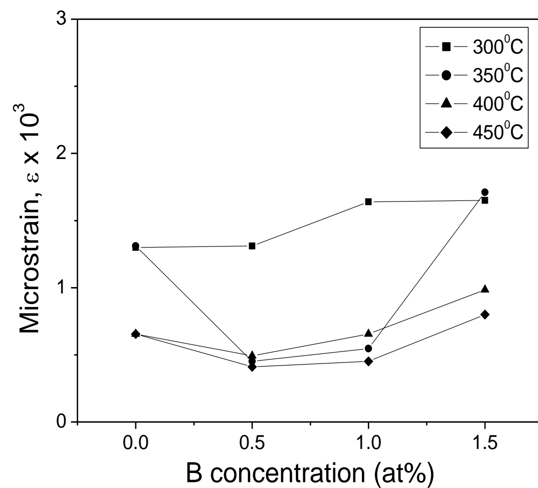

(b)

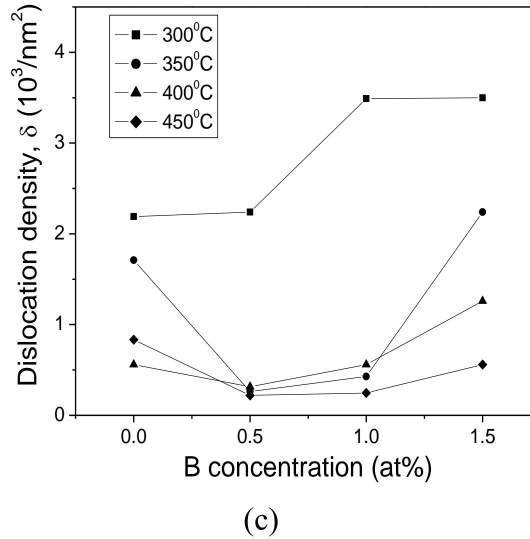

(c)

Figure 5.12: Variation of (a) crystallite size, (b) microstrain and (c) dislocation density with B concentration for ZnO: B thin films deposited at different T_s

5.12 Optical Properties

5.12.1 Transmittance

Optical transmittance (T %) of ZnO and ZnO: B thin films are showed in the Figures 5.13 and 5.14. The maximum T of 89 % is found for the ZnO thin films (Figure 5.17 a). T decreases for 0.50 at% of B concentration (Figure 5.13 b) and it increases with the increase of B concentration up to 1.00 at% (Figure 5.13 c, 5.13 d), then it decreases for 1.50 at% of B doping (Figure 5.13 e). It is noticed in Figure 5.14 that for all the thin films deposited at the T_s of 450 °C, have higher T values. The higher T for films grown at 450 °C may be attributed to the enhancement of crystalline quality of the ZnO thin films [8]. The higher value of T of 86 % is found for the 1.00 at% ZnO: B thin film deposited at T_s of 450 °C as seen in Figure 5.14. Pawar *et al.* have found high T of about 90 % for 1.00 at% ZnO: B thin film deposited by SPT under different deposition conditions [9]. This higher value of T can be attributed to the decrease in free carrier absorption due to the elevated carrier mobility of the film [10]. The overall transmittance behavior of the ZnO and ZnO: B thin films indicate uniformity of the film thickness and less absorbing nature of the surface [11].

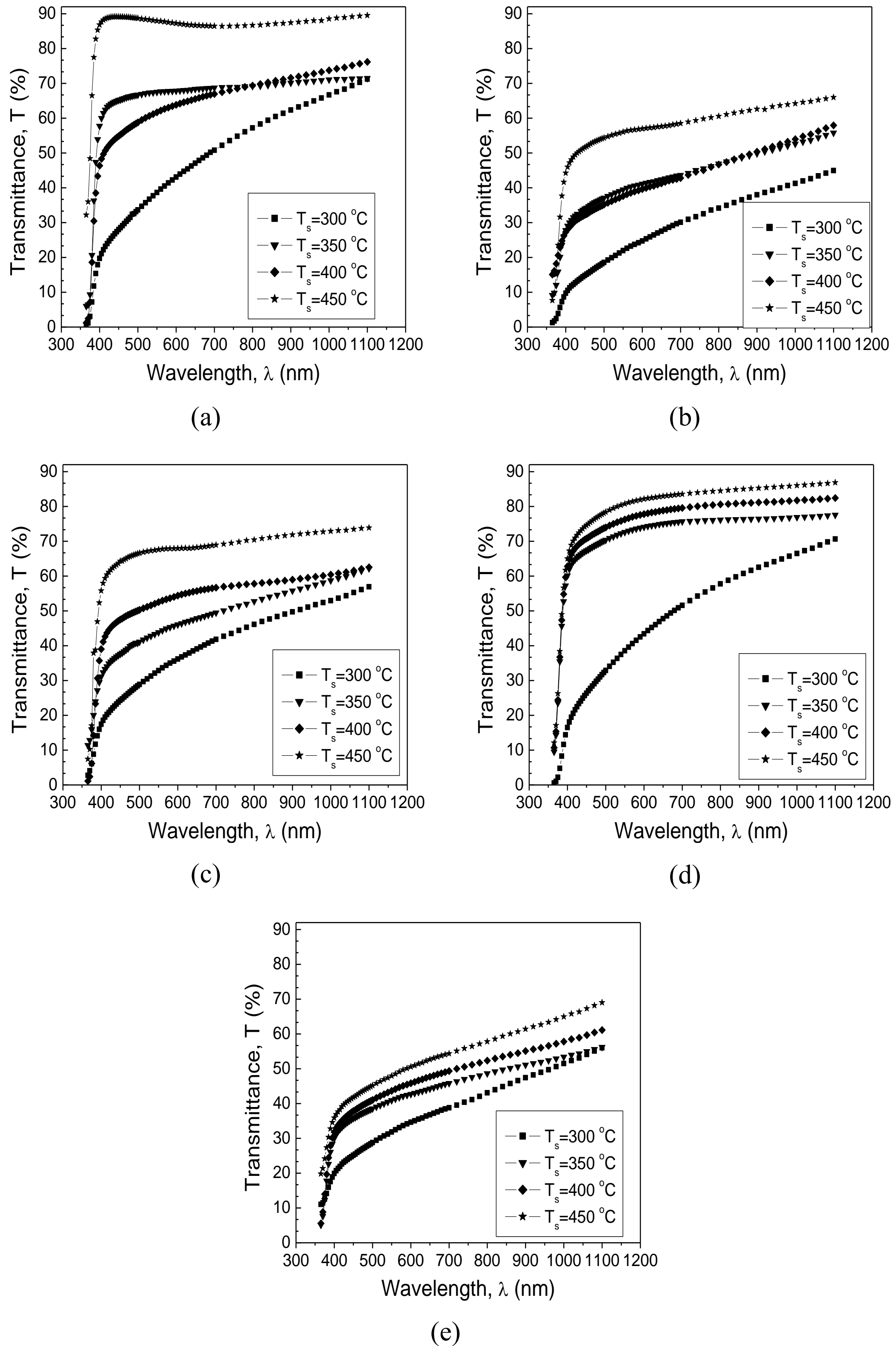

Figure 5.13: Variation of transmittance (%) with wavelength for (a) ZnO, (b) 0.50, (c) 0.75, (d) 1.00 and (e) 1.50 at% ZnO: B thin films deposited at various T_s

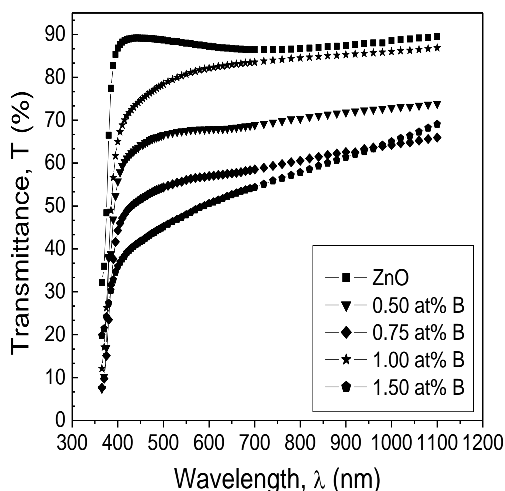

Figure 5.14: Variation of transmittance with wavelength for ZnO and ZnO: B thin films deposited at T_s=450°C

5.12.2 Absorption co-efficient

Absorption co-efficient (α) of ZnO and ZnO: B thin films are calculated from the absorbance data using equation (3.14). α is plotted against photon energy in the Figure 5.15. It can be seen from those graphs that α of the ZnO and ZnO: B thin films are lower in the visible region of solar spectrum because of higher transmittance of thin films in this region. The value of α for are lower for ZnO thin films deposited at various T_s except for that deposited at T_s of 300 °C. ZnO thin films deposited at T_s of 300 °C has the lowest crystallite size as observed in Figure 5.12, may be due to this reason it shows higher value of α than other ZnO thin films. The higher α is found for 0.50 at% ZnO: B thin films. α decreases up to 1.00 at% B doping and again it increases for 1.50 at% B doping in ZnO. All the ZnO thin films deposited at T_s of 450 °C show the lower α values. It has already been found that the crystallite size of ZnO and ZnO: B thin films deposited at T_s of 450 °C are higher as shown in Figure 5.12. Bigger size of crystallites may be the reason less absorption of light at the crystallite boundaries.

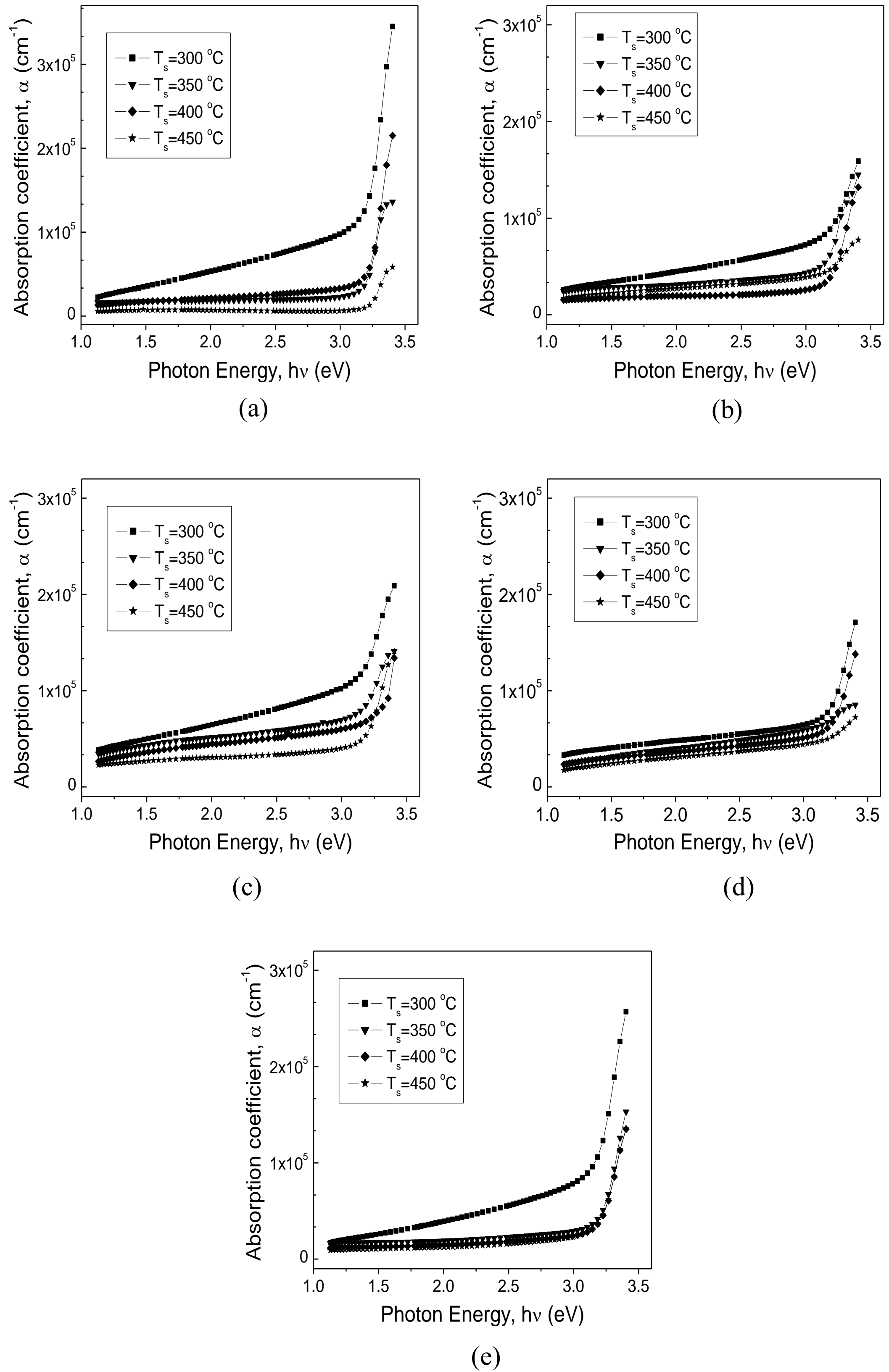

Figure 5.15: Variation of absorption co-efficient with photon energy for (a) ZnO, (b) 0.50, (c) 0.75, (d) 1.00 and (e) 1.50 at% ZnO: B thin films deposited at various T_s

5.12.3 Optical band gap

Optical band gap (E_g) of the ZnO and ZnO: B thin films are determined from the Tauc relation represented by the equation (3.17). Tauc plots are showed in the Figures 5.21 and 5.22 a. The extrapolations of the linear portion to the intercept of energy axis at $(\alpha h\nu)^2 = 0$ are used to find out the E_g of ZnO and ZnO: B thin films. Band gap values of ZnO have been reported between 3.1 and 3.3 eV for ZnO single crystal [12]. The E_g value is found between 3.11 and 3.33 eV, the results obtained are in good agreement with those obtained for single crystal ZnO. E_g is found in this range for ZnO: B thin films deposited onto glass substrate at T_s of 450 ^{o}C by SPT [9] and also by Sol-gel method [13]. The E_g has increased slightly with B concentration and the maximum E_g of 3.33 eV is obtained for 1.00 at% ZnO: B thin film deposited at the T_s of 450°C. Increase of E_g may be attributed to the Burstein- Moss (B-M) effect [14]. B-M effect states that in a heavily doped semiconductor the donor electrons occupy energy levels at the bottom of the conduction band. Pauli principle prevents energy states from being doubly occupied and optical transitions are vertical. Thus, the valence electrons require an additional energy to be excited to the higher energy states in the conduction band to conserve linear momentum, as a result E_g is shifted. Ziabari *et al.* has explained the shift of E_g in ZnO due to p-type doping by Fermi level calculations [15] and corroborated the results with experiments.

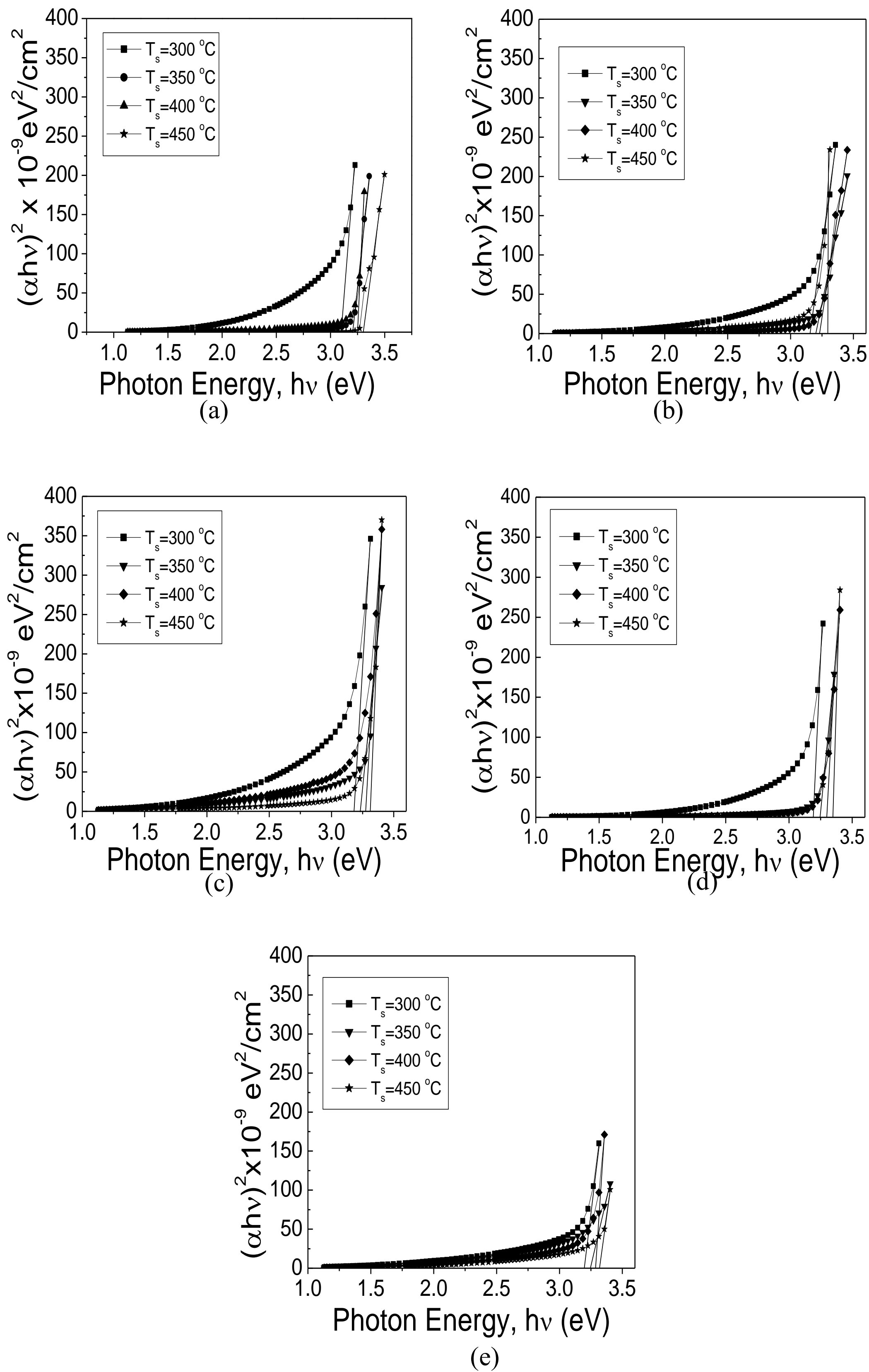

Figure 5.16: Tauc plots of (a) ZnO, (b) 0.50, (c) 0.75, (d) 1.00 and (e) 1.50 at% ZnO: B thin films deposited at various T_s

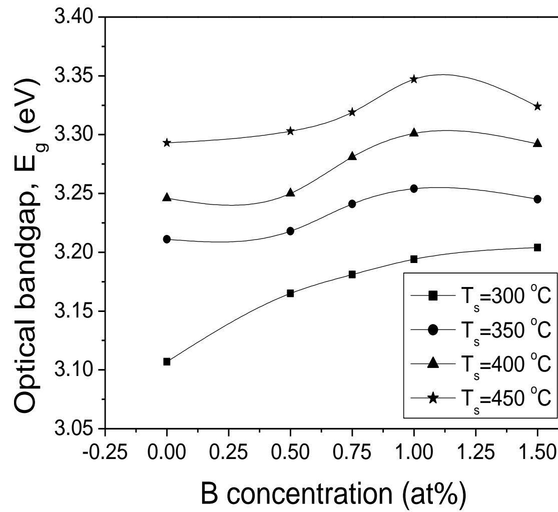

Figure 5.17: Variation of optical band gaps with B concentrations in ZnO thin films deposited at various T_s

5.12.4 Refractive index

Refractive index (n) of the ZnO and ZnO: B thin films is calculated by the equation (3.25) and plotted against photon wavelength in Figures 5.18. The values of n become constant in the visible region of spectrum. Table 7 shows the n for ZnO and ZnO: B thin films at the wavelength of 750 nm which is approximately the middle of the plateau region of the graphs. The n value decreases with the T_s and B concentration up to 1.00 at% of B doping. For 1.50 at% ZnO: B thin films higher n of 2.66 is found. Since speed of light is inversely proportional to n, high value of n of a material indicates that light speed decreases when it passes through the material. It is found that 1.50 at% ZnO: B shows higher α value in the visible region. 1.00 at% ZnO: B thin films show lower n than others and it can be said that light moves faster through the films in the visible region and those exhibits higher transmittance. The values of n run between 1.2 – 2.72, these values are consistent with those obtained for ZnO [16] and ZnO: B thin films synthesized by SPT under some different deposition condition by other workers [6].

Table: 7. Refractive index for ZnO and ZnO: B thin films deposited at various T_s

Sample		Refractive index (n) at the wavelength of 750 nm			
	B concentration (at%)	**T_s (°C)**			
		300	**350**	**400**	**450**
ZnO	0	2.54	2.27	2.26	1.74
	0.50	2.63	2.59	2.49	2.23
	0.75	2.62	2.47	2.61	2.45
	1.00	2.53	2.06	1.94	1.82
	1.50	2.66	2.59	2.57	2.56

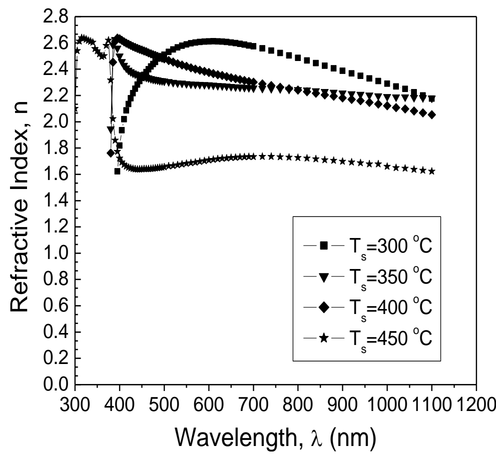

(a)

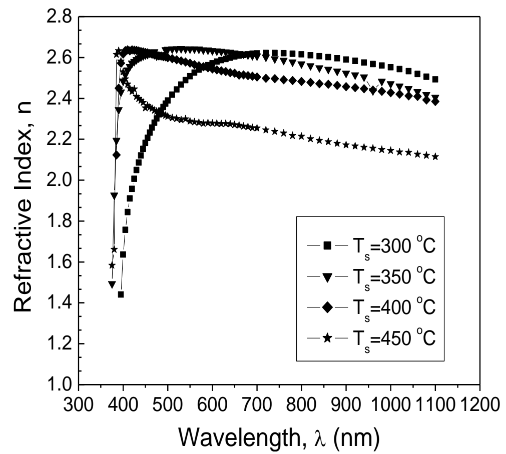

(b)

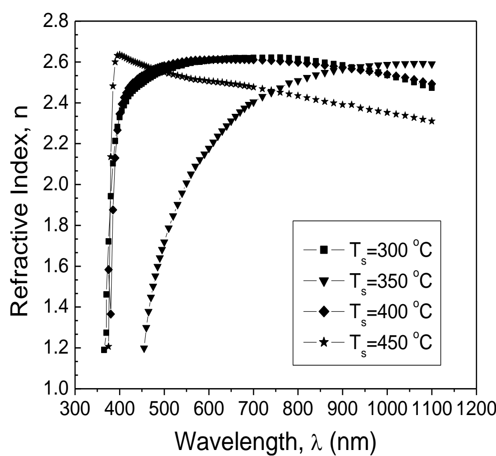

(c)

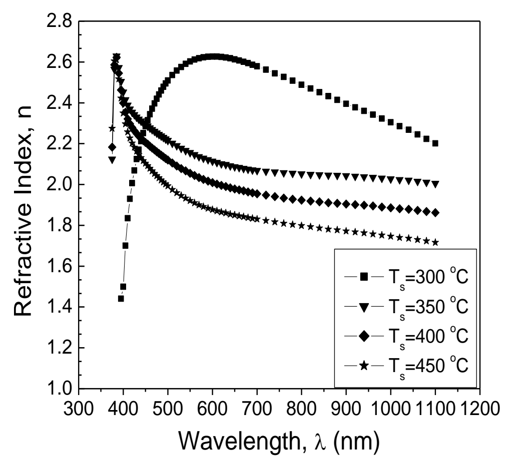

(d)

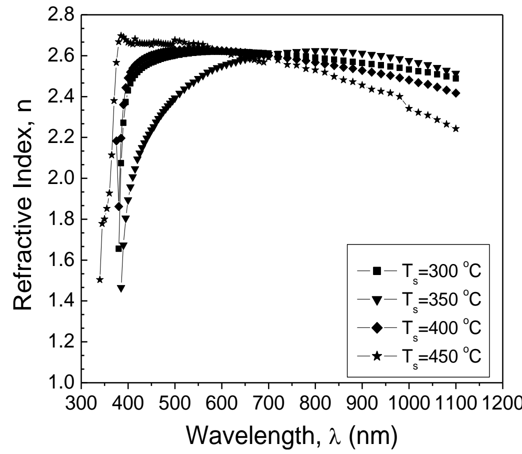

(e)

Figure 5.18: Variation of refractive index with wavelength for (a) ZnO, (b) 0.50, (c) 0.75, (d) 1.00 and (e) 1.5 at% ZnO: B thin films deposited at various T_s

5.12.5 Extinction co-efficient

Variation of extinction coefficient (k) with wavelength for ZnO and ZnO: B thin films are shown in Figure 5.19. Equation (3.26) is used to calculate k of ZnO and ZnO: B thin films. All the thin films show lower absorption in the visible region of solar spectrum and absorption peaks are found in the UV region near the wavelength 380 nm. Similar type of nature k has been observed for ZnO: B thin films deposited by Sol-gel dip coating method [18]. The k values of are lower for ZnO thin films deposited at various T_s, since those are highly transparent. The k decreases due to B doping, lower values of k is found for 1.0 at% ZnO: B thin films and k increases for 1.5 at% B doping in ZnO. All the ZnO and ZnO: B thin films deposited at T_s = 450 °C show the lower values of k, because those have higher T values as discussed before.

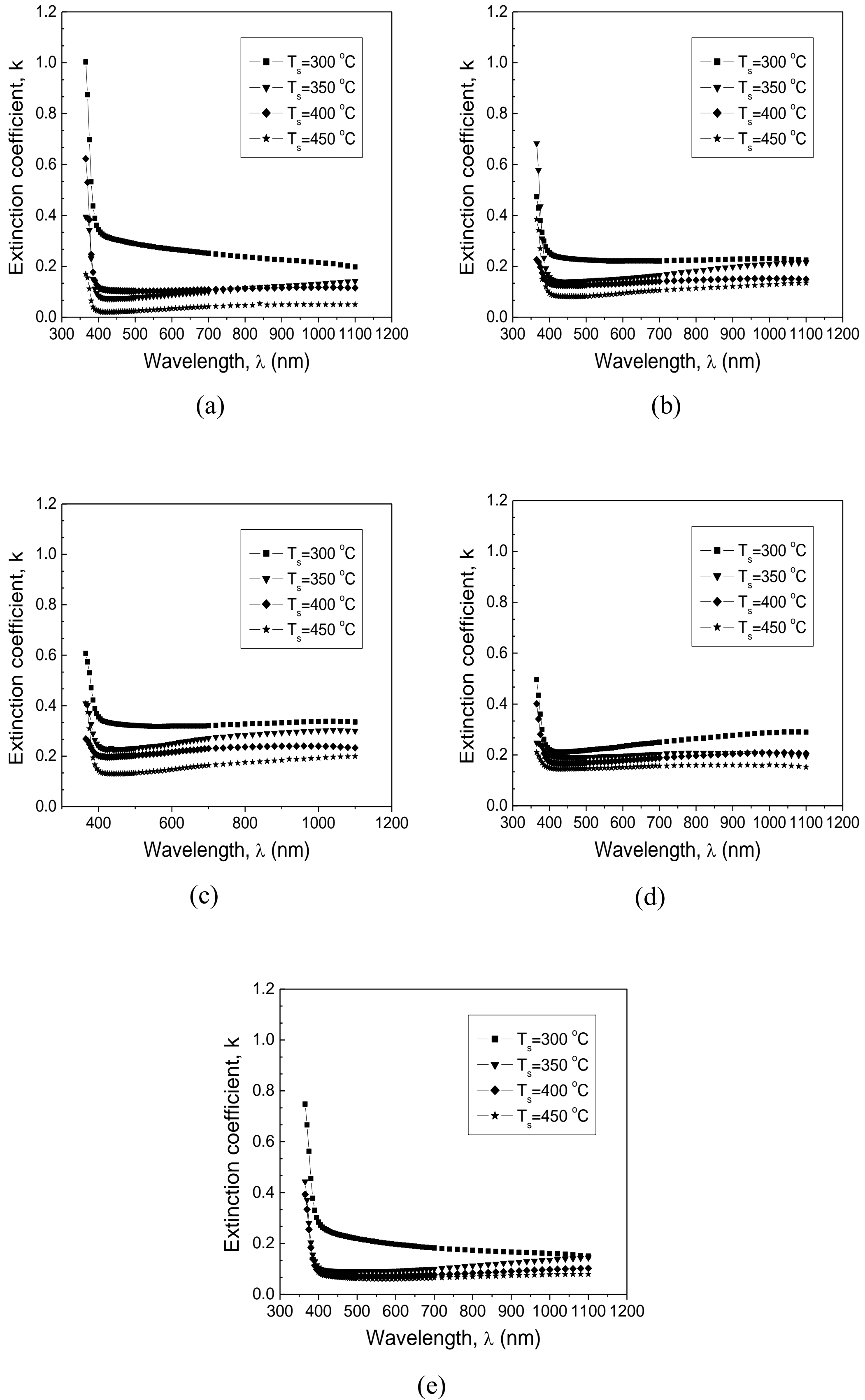

Figure 5.19: Variation of extinction coefficient (k) with wavelength for (a) ZnO, (b) 0.50, (c) 0.75, (d) 1.00 and (e) 1.50 at% ZnO: B thin films deposited at various T_s

5.12.6 Optical conductivity

Optical conductivity (ζ_{opt}) of ZnO and ZnO: B films is calculated by the formula in equation (3.27). For all the thin films, ζ_{opt} increases with photon energy as exhibited in Figure 5.20. ζ_{opt} of ZnO and ZnO: B thin films may have changed due to the formation of coordination complexes when photon is absorbed by the thin films [18].The ζ_{opt} is the increase of electrical conductivity with photon energy. It is a frequency dependent quantity which inversely related to the E_g values. For the larger E_g material ζ_{opt} is expected to be lower. Lower values of ζ_{opt} are found for the ZnO and ZnO: B thin films deposited at T_s= 450 ºC, since those have higher value of E_g as shown in Figure 5.17. For the films deposited at T_s= 300 ºC, ζ_{opt} is higher because of their relatively lower value of E_g. The ζ_{opt} decreases with B concentration between 0.50 – 1.00 at%. For 1.50 at% ZnO: B thin films, there is a slight increase in ζ_{opt}, it is consistent with the variation of band gap with B concentration.

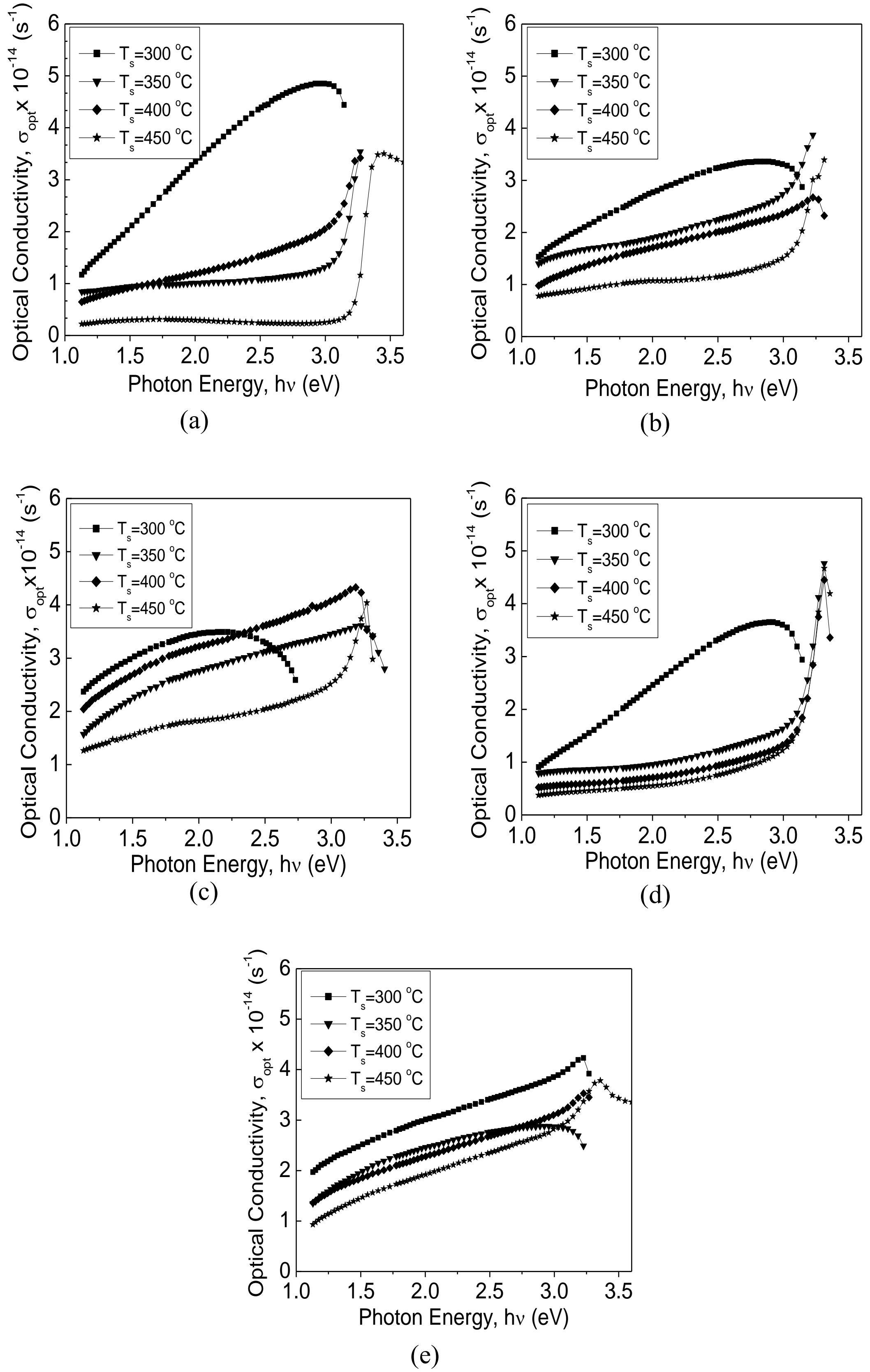

Figure 5.20: Variation of optical conductivity with photon energy for (a) ZnO, (b) 0.50, (c) 0.75, (d) 1.00 and (e) 1.50 at% ZnO: B thin films deposited at various T_s

5.12.7 Dielectric constants and dielectric loss

Real and imaginary parts of dielectric constants (ε_r and ε_i) are calculated using the equation (3.20). ε_r and ε_i represent the absorption associated with the free carrier absorption [17]. ε_r is associated with the refractive index and it shows how much a material slow down the light while passing through it. ε_i gives the idea to what extent dielectric material absorbs energy from electromagnetic field of light due to dipole motion. Figures 5.21 and 5.22 exhibit that ZnO and ZnO: B thin films deposited at T_s of 450 ºC have lower values of ε_r and ε_i and those decrease with B doping up to 1.0 at% and increase slightly for 1.5 at% B doping in ZnO thin films. Similar type of dielectric properties are observed for ZnO: B thin films deposited by Sol-gel dip coating method [18].

Dielectric loss tangent (tanδ) has been calculated by the equation (5.1),

$$\tan\delta = \frac{\varepsilon_i}{\varepsilon_r} \qquad (5.1)$$

tanδ of ZnO and ZnO: B thin films are plotted against wavelength in Figure 5.23. The tanδ values are found less for the ZnO thin films deposited at T_s= 450 ºC. tanδ decreases with the increase of B concentration up to 1.0 at% B doping and then it increases in the case of 1.50 at% ZnO: B. Decrease of tanδ indicates more loss of photon energy in the medium and vice versa. The variation of tanδ with photon wavelength is consistent with the nature of absorption in the ZnO and ZnO: B thin films.

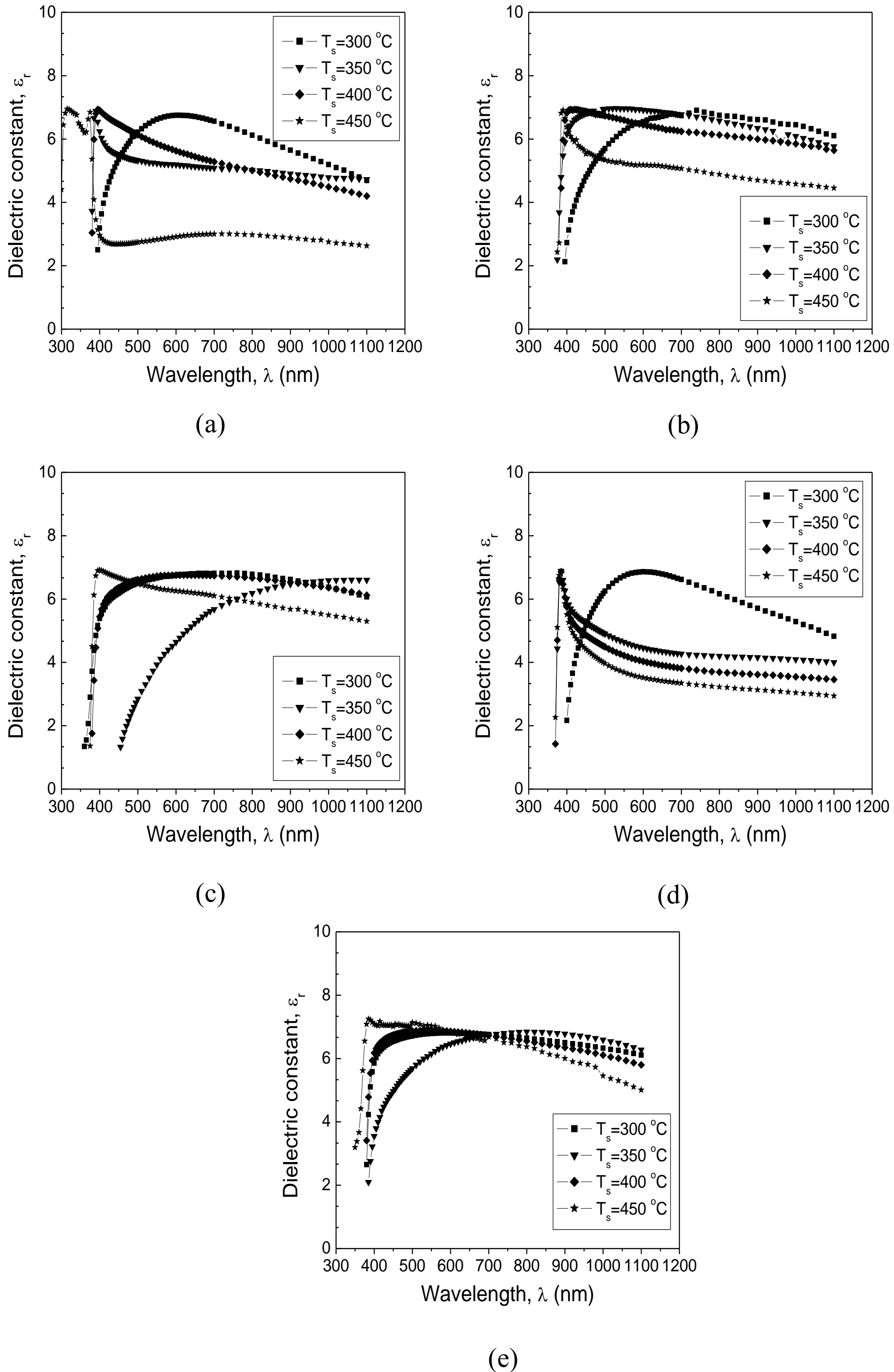

Figure 5.21: Variation of real part of dielectric constant with wavelength for (a) ZnO, (b) 0.50, (c) 0.75, (d) 1.00 and (e) 1.50 at% ZnO: B thin films deposited at various T_s

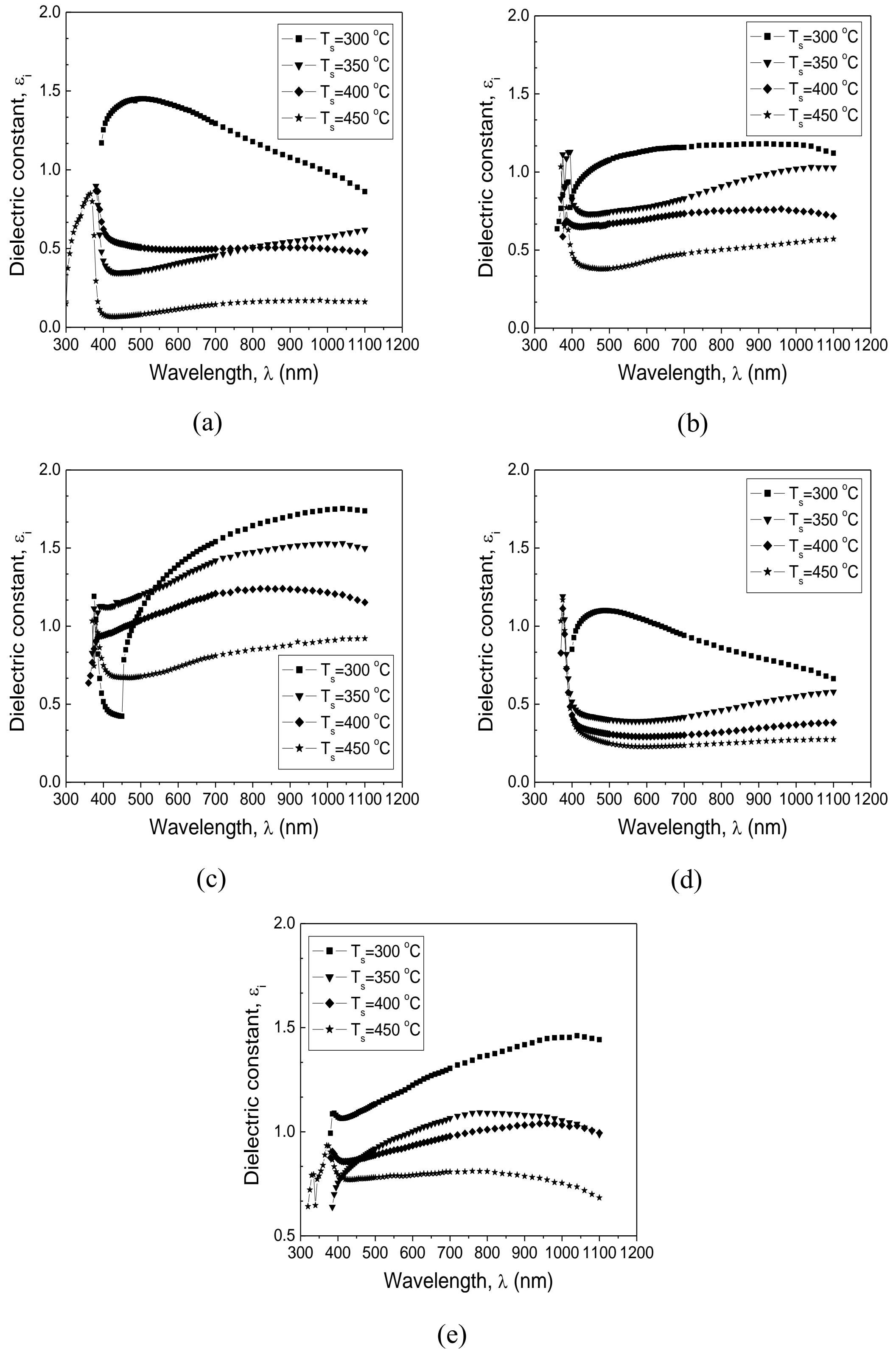

Figure 5.22: Variation of imaginary part of dielectric constant with wavelength for (a) ZnO, (b) 0.50, (c) 0.75, (d) 1.00 and (e) 1.50 at% ZnO: B thin films deposited at various T_s

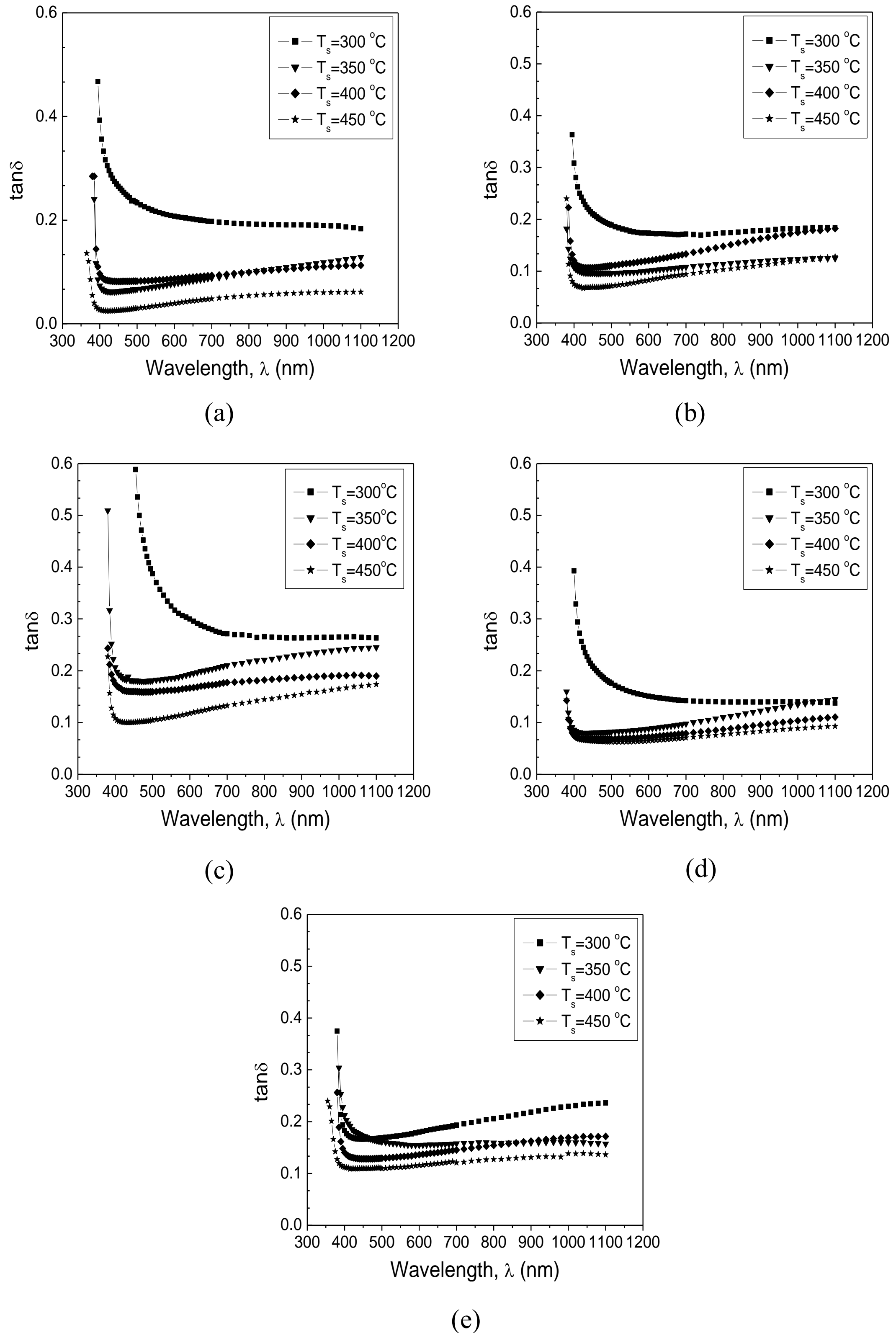

Figure 5.23: Variation of dielectric loss tangent with wavelength for (a) ZnO, (b) 0.50, (c) 0.75, (d) 1.00 and (e) 1.50 at% ZnO: B thin films deposited at various T_s

5.13 Electrical Properties

5.13.1 I-V characteristics

Electrical resistivity of ZnO and ZnO: B thin films are measured by inline four point probe method. I-V characteristics curves of the ZnO thin films are shown in the Figure 5.24. The data for I-V characteristics are taken for the supply voltages in the range 0 – 20 V and the corresponding current and voltage drops are measured. I-V graphs are almost linear in nature and the conduction process is ohmic [2]. The resistivities of the thin films are calculated using the I-V graphs. Resistivity decreases with B concentration up to 1.0 at% of B doping and then it increases for 1.5 at% B doping (Figure 5.25), similar nature is observed for ZnO: B in some published works [6, 13] Resistivity is found between 1.97×10^3 and 1.71×10^4 Ω-m. The ZnO and ZnO: B thin films deposited at 450 ºC show lower resistivity than others. The minimum resistivity is found for 1.00 at% ZnO: B thin films, similar result is found for ZnO: B thin films prepared by Sol-gel method [19].

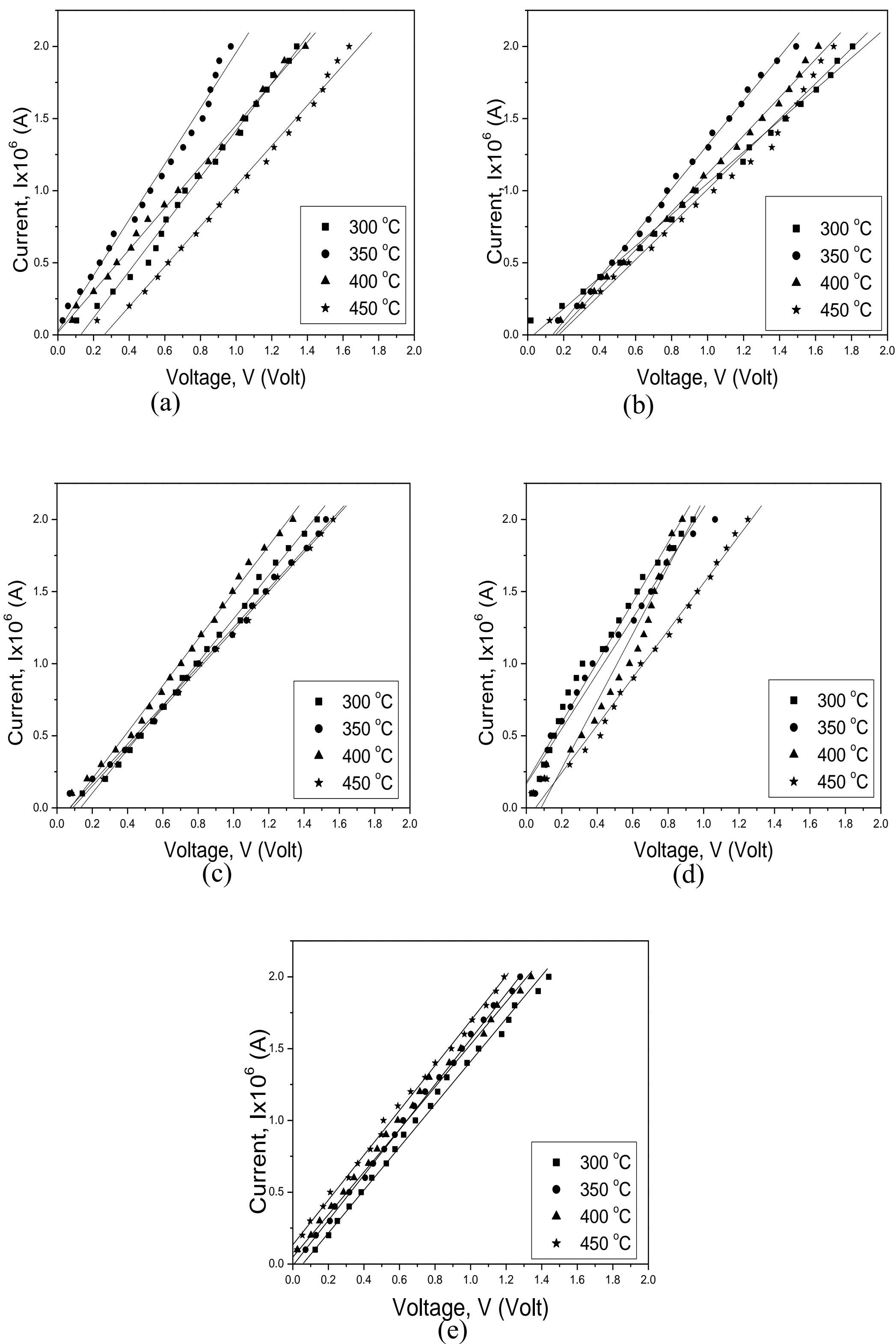

Figure 5.24: I-V characteristic graphs of (a) ZnO, (b) 0.50, (c) 0.75, (d) 1.00 and (e) 1.50 at% ZnO: B thin films deposited at various T_s

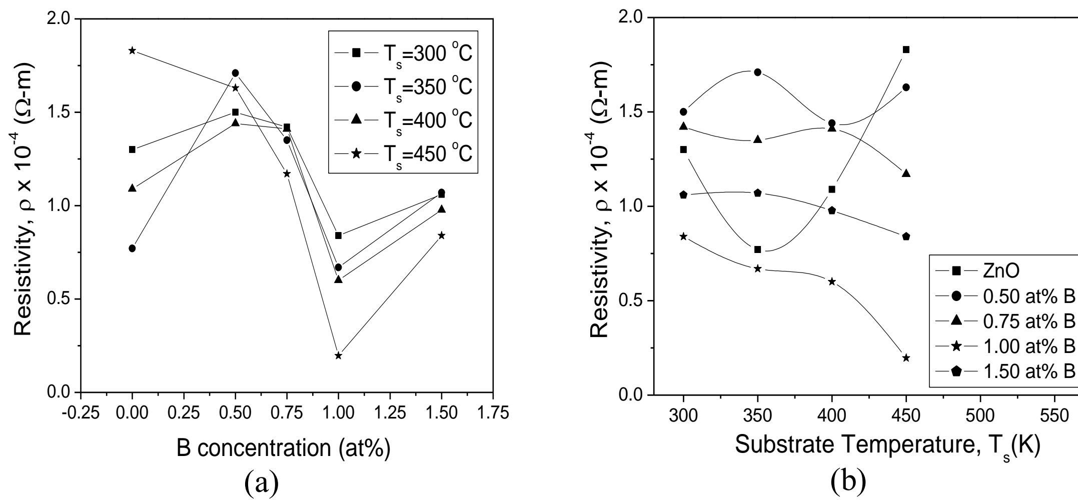

Figure 5.25: Variation of resistivity of ZnO thin films with (a) B concentration and (b) substrate temperature

5.13.2 Temperature dependence of electrical conductivity and activation energy

Activation energy (ΔE) of ZnO and ZnO: B thin films are calculated by plotting the electrical conductivity against inverse of absolute temperature as shown in Figure 5.26. The slopes of the graphs are used in equation (3.34) to find out the activation energies of ZnO and ZnO: B thin films. ΔE of ZnO and ZnO: B thin films are plotted as a function of B concentration in Figure 5.27. Rise and fall in ΔE values are seen in the range of concentration 0 – 1.50 at%. ΔE decreases with B doping concentration from 0 to 0.75 at% of B doping and it increases for 1.00 at% of B doping and then it decreases for 1.50 at% of B doping. Higher value of ΔE indicates that reaction is very sensitive to temperature [20]. ZnO and ZnO: B thin films deposited at lower T_s have higher average ΔE values than those deposited at higher T_s. It indicates that electrical conduction mechanism is faster in ZnO and ZnO: B thin films deposited at lower T_s. Again it is seen that for 1.00 at% ZnO: B thin films have higher ΔE. It may be attributed to less resistivity and more crystalline structure of the films. The values of ΔE are found between 0.27 and 0.52 eV, the result is consistent with those obtained for ZnO: B thin films synthesized onto ITO substrate by Sol-gel method [2] and for the same material deposited by spray CVD [11].

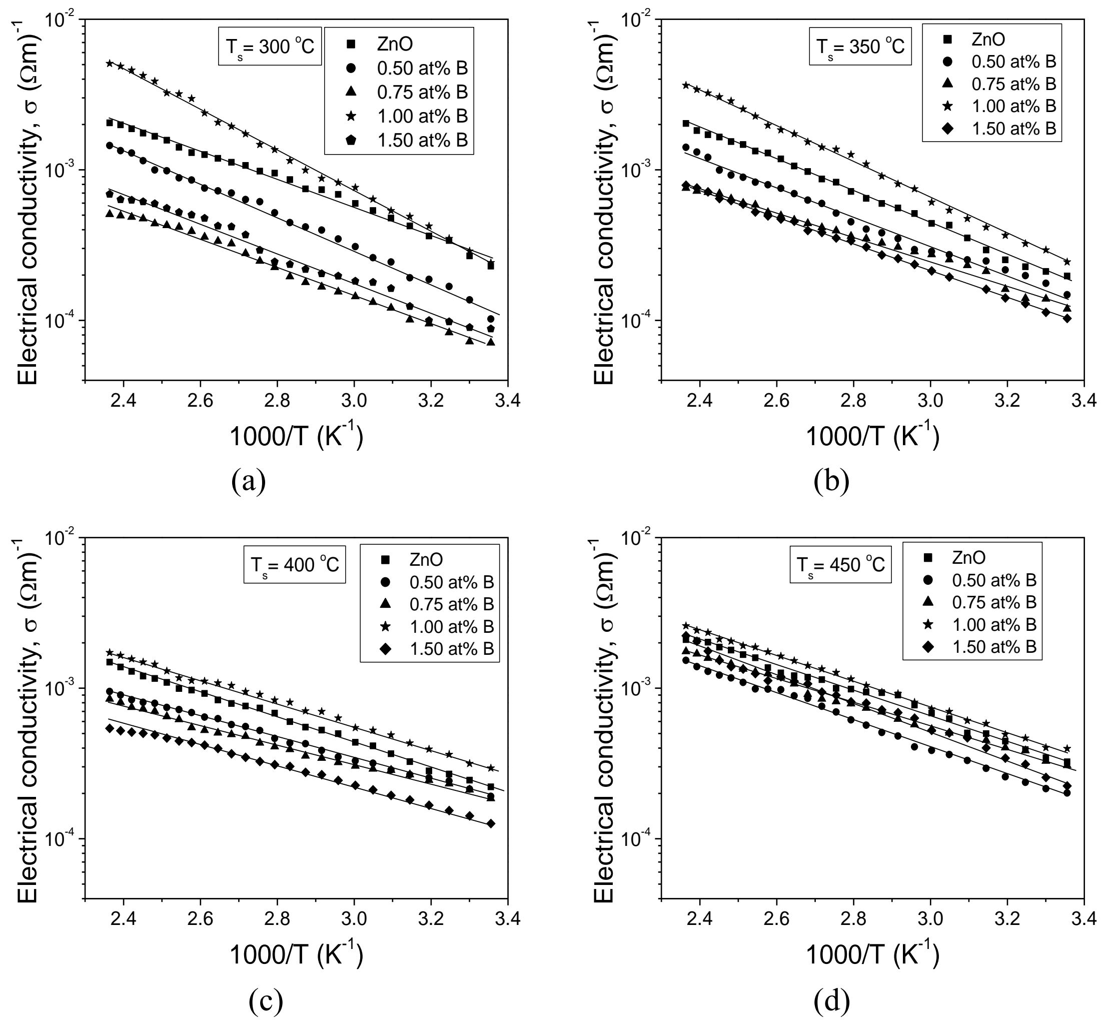

Figure 5.26: Electrical conductivity versus 1000/T graphs of ZnO and ZnO: B thin films deposited at (a) 300, (b) 350, (c) 400 and (d) 450 ^{o}C

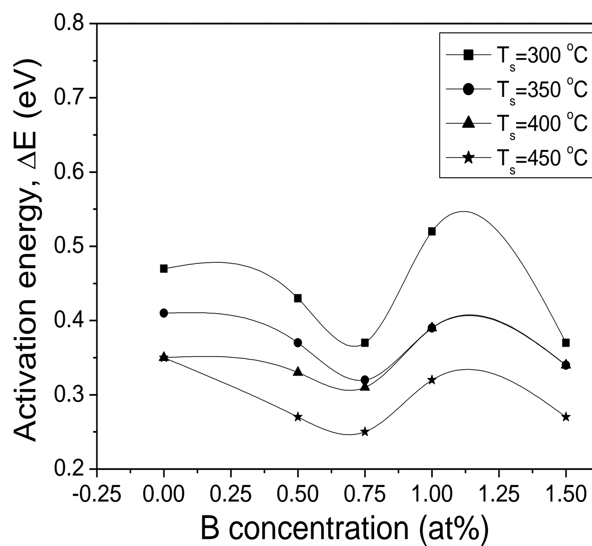

Figure 5.27: Variation of activation energy with B concentration for ZnO: B thin films

References

[1] Ilican, S., Caglar, Y., Caglar, M., Yakuphanoglu, F., "Electrical conductivity, optical and structural properties of indium-doped ZnO nanofiber thin film deposited by spray pyrolysis method", Physica E, 35, 131–138, (2006).

[2] Caglar, M., Ilican, S., Caglar, Y., Yakuphanoglu, F., "Boron doped nanostructure ZnO films onto ITO substrate", J. Alloys. Compd., 509, 3177–3182, (2011).

[3] Kim, G., Bang, J., Kim, Y., Rout, S.K., Ihl Woo, S., "Structural, electrical and optical properties of boron doped ZnO thin films using LSMCD method at room temperature", Appl. Phys. A, 97, 821–828, (2009).

[4] Shakti, N., Gupta, P. S., "Structural and Optical Properties of Sol-gel Prepared ZnO Thin Film", Appl. Phys. Res., 2(1), 19-28, (2010).

[5] Özgür, Ü., Alivov, Y.I., Liu, C., Teke, A., Reshchikov, M. A., Dogan, S., Avrutin, V., Cho, S.J., Morko, H., "A comprehensive review of ZnO materials and devices", J. Appl. Phys., 98, 041301, (2005).

[6] Lokhande, B. J., Patil, P.S., Uplane, M.D., "Studies on structural, optical and electrical properties boron doped zinc oxide films prepared by spray pyrolysis technique", Physica B., 302–303, 59–63, (2001).

[7] Jabbar, R. H., Elttayef, A. K., Jabor, A. A., Hashim, A. H., "Structural properties of boron doped zinc oxide nanostructure films deposited on glass substrate", Int. J. Appl. Innov. Eng. Manag., 2(10), 222-227, (2013).

[8] Ayouchi, R., Martin, F., Leinen, D., Ramos-Barrado, J.R., "Growth of pure ZnO thin films prepared by chemical spray pyrolysis on silicon", J. Cryst. Growth., 247, 497–504, (2003).

[9] Pawar, B. N., Jadkar, S.R., Takwale, M.G., "Deposition and characterization of transparent and conductive sprayed ZnO: B thin films", J. Phys. Chem. Sol. 66 1779–1782, (2005).

[10] Hagiwara, Y., Nakada, T., Kunioka, A., "Improved J(sc) in CIGS thin film solar cells using a transparent conducting ZnO : B window layer", Sol. En. Mat. Sol. Cells., 67(1-4), 267-271, (2001).

[11] Yadav, S. C., Uplane, M.D. "Synthesis and properties of Boron doped ZnO thin films by spray CVD technique at low substrate temperature", Int. J. Eng. Sci. Technol., 4(12), 4893-4898, (2012).

[12] Srikant, V., Clarke, D. R., “On the optical band gap of zinc oxide”, J. Appl. Phys., 83, 5447-5451, (1998).

[13] Kumar, V., Singh, R.G., Purohit, L.P., Mehra, R.M., “Structural, transport and optical properties of boron-doped zinc oxide nanocrystalline”, J. Mater. Sci. Technol., 27(6), 481-488, (2011).

[14] Burstein, E., “Anoma1ous Optical Absorption Limit in InSb”, Phys.Rev., 93, 632-633, (1954).

[15] Ziabari, A. A., Rozati, S.M., “Carrier transport and band gap shift in n-type degenerate ZnO thin films: The effect of band edge Nonparabolicity”, Physica B., 407, 4512–4517, (2012).

[16] Kumar, R. A., Manivannan, V., Krishnaraj, S., “Growth and Characterization of ZnO Nano thin films using Spray pyrolysis”, Int. J. Res. Pure and Appl. Phys., 3(4), 39-42, (2013).

[17] Chopra K. L., “Thin Film Phenomena”, McGraw Hill Book Company: USA, (1969).

[18] Kim, S. Yoon, H., Kim, D. Y., Kim, S. O., Leem, J. Y.“Optical properties and electrical resistivity of boron-doped ZnO thin films grown by sol–gel dip-coating method”, Opt. Mater., 35(12), 2418-2424, (2013).

[19] Tsay, C. Y., Hsu, W. T., “Sol–gel derived undoped and boron-doped ZnO semiconductor thin films: Preparation and characterization”, Ceram. Int., 39 (7), 7425-7432, (2013).

[20] Wade, L.G., “Organic Chemistry”. (6th ed), Pearson Prentice Hall: New Jersey, (2006).

CHAPTER 6

CONCLUSIONS AND SUGGESTIONS FOR FURTHER WORK

CHAPTER 6

CONCLUSIONS AND SUGGESTIONS FOR FURTHER WORK

6.1 Conclusions

In the present work, ZnO and ZnO: B thin films with B concentrations of 0.50, 0.75, 1.00 and 1.50 at% are synthesized onto glass substrates at T_s of 300, 350, 400 and 450 °C. The thin films have thicknesses between 150 and 278 nm. The influence of variation of T_s and B concentration on structure and various physical properties of ZnO and ZnO: B thin films are studied elaborately.

SEM images of the ZnO and ZnO: B thin films exhibit that the substrate is nicely covered with fibrous and non-fibrous films within the field of view. Nanofibers are formed around the nucleation centers and those are more densely placed in the ZnO: B thin films than those in the ZnO thin films. Nanofiber thickness increases with the increase of T_s and B concentration from 0 to 0.75 at% and that decreases for 1.00 and 1.50 at% of B doping. The shape of particles forming the nanofibers is changed from circular to elliptical for 1.50 at% ZnO: B thin films. EDX analysis reveals that the ZnO and ZnO: B thin films are stoichiometric and B is successfully incorporated into ZnO thin films.

ZnO and ZnO: B thin films are polycrystalline hexagonal wurtzite type of crystal structure with preferential orientation along (002) plane. No peak corresponding to B impurity is found, that means B has substituted Zn from their lattice sites without changing the hexagonal type of structure. For the ZnO and ZnO: B thin films deposited at higher T_s the peaks are sharp and intensities of the peaks increase up to 1.0 at% B doping. a and c values of ZnO and ZnO: B thin films increase and decrease such that c/a ratio is comparable to that for an ideal hexagonal structure. Average crystallite size is found between 27 and 88 nm for ZnO: B thin films. It decreases with the increase of B doping concentration. ε and δ decrease with the increase of B concentration.

ZnO and ZnO: B thin films disclose that the T is higher for the ZnO thin films. T increases with B concentration between 0.50 -1.00 at% and then it falls for 1.5 at% of B doping. It is observed that the thin films deposited at the T_s of 450 °C have higher T. Higher T may be attributed to the enhancement of crystalline quality of the ZnO thin films. The higher value of T is found to be 86% for the 1.0 at% ZnO: B thin film deposited at T_s of 450 °C. The overall T behavior of the ZnO and ZnO: B thin films indicate the uniformity of the film thickness and less absorbing nature of the surface. Optical band gap of ZnO and ZnO: B thin films are found between 3.11 and 3.33 eV. Optical band gap increases with the increase of T_s and B concentration between 0 and 1.00 at%. Refractive index of ZnO and ZnO: B thin films is found between 1.2 and 2.72. Refractive index of the thin films decreases with the increase of T_s and B concentration up to 1.00 at%. k decreases with the increase of B doping up to 1.00 at% and then it increases for 1.5 at% of B doping. ZnO and ZnO: B thin films deposited at higher T_s have lower k. ε_r, ε_i, tanδ and ζ_{opt} of the ZnO and ZnO: B thin films follow the same trend as k.

Electrical resistivity of the ZnO and ZnO: B thin films run between 1.97×10^3 and 1.71×10^4 Ω-m at room temperature. Resistivity decreases with the rise of temperature for all the thin films. ΔE of the thin films is higher for the films deposited at lower T_s. It is observed that ΔE decreases with the increase of B doping from 0 to 0.75 at% and then it increases for 1.50 at% of B doping.

In conclusion it can be inferred that ZnO and ZnO: B thin films synthesized by SPT have good surface morphology, well crystalline quality, high transparency and low resistivity. B doping causes change in almost all the physical properties of ZnO. The results obtained in this work are in good agreement with those obtained by other workers for the same material. ZnO: B thin films can be suitable for optoelectronic applications.

6.2 Suggestions for Further Work

This is the first time that ZnO: B thin films have been synthesized in our laboratory. In order to improve the quality of the thin film of this material and their characterization more works are required, for example:

i. Characterization of ZnO: B thin films synthesized by changing other deposition parameters.
ii. Study of the surface by Atomic force microscopy.
iii. Investigation of electrical properties at low temperature.
iv. Measurement of temperature dependent Hall effect.
v. Study the annealing effect.